Effects of Impurities on CO_2 Geological Storage

Zhiyu Wang

Thesis submitted to the

Faculty of Graduate and Postdoctoral Studies

in partial fulfillment of the requirements for the degree of

Master of Applied Science

Department of Chemical and Biological Engineering

Faculty of Engineering

University of Ottawa

© Zhiyu Wang, Ottawa, Canada, 2015

Abstract

This project studied the physical and chemical effects of typical impurities on CO_2 storage using both experimental approaches and theoretical simulation. Results show that the presence of typical non-condensable impurities from oxyfuel combustion such as N_2, O_2, and Ar resulted in lower density than pure CO_2, leading to decreased CO_2 storage capacity and increased buoyancy in saline aquifers. In contrast, inclusion of condensable SO_2 in CO_2 resulted in higher density than pure CO_2 and therefore increased storage capacity. These impurities also had a significant impact on the phase behaviours of CO_2, which is important to CO_2 transportation. Different effects on rock chemistry were detected with experimental systems containing pure CO_2, CO_2 with SO_2, or CO_2 with SO_2 and O_2 under conditions simulating that in a potential storage site. An equation was proposed to predict the effects of the rock chemistry on the porosity of rocks.

Keywords: CO_2 storage, impurities, basal aquifer, capacity, buoyancy, porosity.

Résumé

Ce projet a étudié les effets physiques et chimiques des types d'impuretés sur le stockage du CO_2 en utilisant les approches expérimentales et la simulation théorique. Les résultats démontrent que la présence des types d'impuretés non condensables de l'oxycombustion tels que N_2, O_2 et Ar ont une plus basse masse volumique que le CO_2 pur. Donc, cela conduit à une diminution de la capacité de stockage du CO_2 et à une augmentation de la flottabilité dans les aquifères salins. Cependant, l'inclusion de SO_2 condensable dans le CO_2 a démontré une masse volumique plus élevée que le CO_2 pur donc une augmentation de la capacité de stockage. Ces impuretés ont également démontré l'importance de leurs effets sur les changements de phase du CO_2 et ces derniers sont cruciaux pour le transport de CO_2. Différents effets chimiques des roches ont été détectés en effectuant des systèmes expérimentaux contenant du CO_2 pur, CO_2 avec SO_2, CO_2 ou SO_2 et O_2 sous des conditions simulant un potentiel d'un site de stockage. Une équation empirique a été proposée pour interpréter les effets chimiques des roches sur leur porosité.

Mots clés: stockage du CO_2, impuretés, aquifère poreux, capacité, flottabilité, porosité.

Acknowledgements

Firstly, I would like to express my sincere gratitude to my supervisors, Dr. Christopher Lan and Dr. Jinsheng Wang, for their great support and guidance in my project, for their patience, motivation, enthusiasm and immense knowledge. Without their dedicated involvement in every step throughout the process, this project would have never been accomplished. I am also very grateful to David Ryan, the leader of the CO_2 Storage Group in CanmetENERGY-Ottawa, who allowed me to complete my experimental work for my thesis in their laboratory and gave me much needed help.

Secondly, I wish to thank the members of the CO_2 Storage Group of CANMETEnergy-Ottawa, including, Ms. Vivien Ko, Dr. Ian He and Mr. Andrew Wigston. They provided me all the facilities for my project and have been encouraging me throughout my work. No matter on work or life, they tried their best to understand my situation and was always willing to give the best suggestions. I thank them for offering this invaluable opportunity to join them in their research work. The work in CANMET will be the most memorable experience in my life. In addition to the work in CANMET, I got an unforgettable life on campus. During the study and work in Faculty of Engineering, I would like to thank the fellows who are working with Professor Lan, including Yifan, MohammodAli, Licheng, Xiaozhou and Johnson. They always helped me when I was in trouble.

Thirdly, I would like to acknowledge the administrative and technical support from Department of Chemical Engineering at University of Ottawa, and Natural Resources Canada. Even though the procedures of registration in these two departments were tedious, I have finished my work with their patience and great support. Here, I thank Dr. Xudong Cao and Ms. Yunjuan Hu for their permission and arrangement in my Master program.

Finally, I really appreciate the understanding and support from my dear friends and my family. They are always there cheering me up and stood by me through the good and bad times.

Content

Abstract ... **ii**
Résumé ... **iii**
Acknowledgements ... **iv**
List of Figures ... **viii**
List of Tables ... **x**
Nomenclature ... **xi**
Abbreviations ... **xii**
Chapter 1 ... **1**
Introduction ... **1**
1.1 Mechanisms of CO_2 trapping in CCS ... 3
1.2 CCS in Canada ... 4
1.3 Research objectives ... 5
1.4 Structure of thesis ... 7
1.5 References ... 8
Chapter 2 ... **10**
Literature Review ... **10**
2.1 Introduction ... 10
2.2 Simulation model ... 11
2.2.1 Equations of state ... 11
2.2.2 Evaluation of EOSs ... 13
2.2.3 Other specific models ... 15
2.3 Survey of experimental data ... 15
2.3.1 PVTxy ... 15
2.3.2 Binary interaction parameter, k_{ij} ... 18
2.4 Physical effects ... 18
2.4.1 Phase behaviour ... 18
2.4.2 Density and normalized CO_2 storage capacity ... 19

2.4.3 Permeation 22
2.5 Chemical effects 24
2.5.1 Possible mineral in reservoirs 24
2.5.2 Formation of acid and dissolution of solid minerals 26
2.5.3 Pure CO_2 26
2.5.4 Impure CO_2 27
2.5.5 Redox reaction by possible oxides in gas mixture 27
2.5.6 Effects of SO_2 on the porosity of reservoir 28
2.6 Knowledge gaps 30
2.7 References 31
Chapter 3 38
Effects of Impurities on the Physical Properties of CO_2 in Geological Storage Sites 38
Abstract 38
3.1 Introduction 39
3.2 Methodologies 40
3.2.1 Simulation by REFPROP 40
3.2.2 Experimental method 40
3.3 Results and discussions 42
3.4 Conclusion 54
3.5 References 55
Chapter 4 57
The Geochemical Reactions of CO_2 Mixtures in Saline-aquifer Storage Sites 57
Abstract 57
4.1 Introduction 58
4.2 Methodologies 60
4.2.1 Sample description 60
4.2.2 Experimental method 62
4.2.3 Modelling method (PHREEQC) 66
4.3 Analytical methods and results 67
4.3.1 Solid characterization 67
4.3.1.1 XRD 67

4.3.1.2 XRF and LECO-S 71
4.3.1.3 SEM-EDS 73
4.3.2 Liquids analyses 76
4.3.3 Simulation results 77
4.4 Discussion 81
4.4.1 Effects of CO_2 gas mixture on pH and conductivity 81
4.4.2 Chemical reactions of rock minerals 84
4.4.3 Ion analyses 86
4.4.4 Saturation equilibrium of minerals 88
4.4.5 The quantification of porosity change 89
4.4.6 The corrosion on the pipeline material 91
4.5 Conclusion 95
4.6 References 96
Chapter 5 101
Conclusion 101
Appendix A 102
Appendix B 103

List of Figures

Figure 1.1	Three steps of CCS chain…….	1
Figure 1.2	Simplified sketch of three CO_2 capture system for power plants……	2
Figure 1.3	Areal extent of the Basal Aquifer in the Northern Great Plains region of the United States and the Prairie Region of Canada……..	5
Figure 2.1	Predicted and experimental density of the multicomponent CO_2-rich stream.	20
Figure 2.2	Predicted and experimental density difference……	21
Figure 2.3	Calculated densities for CO_2 and CO_2 mixtures as a function of pressure at 330 K……	21
Figure 2.4	Normalized CO_2 storage capacities at 330 K……...	22
Figure 2.5	Normalized permeation flux……	24
Figure 3.1	Sketch of experimental setup……...	41
Figure 3.2	The comparisons of calculated density with measured density of Gas Mixture 1. …….....	43
Figure 3.3	The comparisons of calculated normalized density with measured normalized density of Gas Mixture 1……..	44
Figure 3.4	The comparisons of calculated density with measured density of Gas Mixture 2……..	45
Figure 3.5	The comparisons of calculated normalized density with measured normalized density of Gas Mixture 2……..	45
Figure 3.6	The comparison of the density of Gas Mixture 1 and Gas Mixture 2…….	47
Figure 3.7	The deviation of representing 15% multi-light impurities by Ar…….	47
Figure 3.8	Calculated deviation between the density of Gas Mixture 1 and the gas with a same concentration of impurities represented by Ar……	48
Figure 3.9	Normalized CO_2 capacity for Gas Mixture 1……..	49
Figure 3.10	Normalized buoyancy towards 12W4…….	52
Figure 3.11	Normalized buoyancy towards 7W4……...	52
Figure 3.12	Phase Behaviours of Gas Mixture 1, Gas Mixture 2 and pure CO_2…….	53
Figure 3.13	Calculated normalized capacity showing the effect of SO_2 on CO_2 storage capacity…….....	54
Figure 4.1	Location of wells from which samples were collected and analyzed for mineralogy of the Basal Aquifer in the Prairie region of Canada. ……..	61
Figure 4.2	Schematic diagram of experimental setup……...	65
Figure 4.3	Reactor for static test……	65

Figure 4.4	XRD results of 10-11-067-12W4…….	69
Figure 4.5	XRD results of 06-29-007-07W4…….	70
Figure 4.6	Results of XRF and LECO-S. …….	72
Figure 4.7	SEM results of solid samples……...	75
Figure 4.8	The corrosions of Reactors 4 and 7 after reaction……	84
Figure 4.9	Predicted corrosion rates and experimental results with the variation of SO_2 concentration…….....	94
Figure 4.10	Predicted variation of corrosion rate with O_2 mole fraction……	94
Figure 4.11	Measured corrosion rates and predicted results with the variation of temperature……...	95
Figure B.1	Geologic Time Scale……**....**	103

List of Tables

Table 1.1	Estimated operating condition of CCS……..	3
Table 2.1	Possible Impurities……....	10
Table 2.2	Impurity concentration……	10
Table 2.3	EOSs for CCS system ……	12
Table 2.4	AAD of EOSs on the calculated VLE properties of binary CO_2-mixtures.	14
Table 2.5	AAD of EOSs on both gas and liquid volume of various binary CO_2-mixtures……...	14
Table 2.6	Summary of the experimental conditions for CO_2-mixtures……	17
Table 2.7	Calibrated k_{ij} for different binary CO_2-mixture……..	18
Table 2.8	Possible minerals for simulation of geochemical reaction…….	25
Table 4.1	List of wells and core samples for laboratory testing…….	62
Table 4.2	Original well water analyses……...	62
Table 4.3	Original solid sample analyses by XRD…….	63
Table 4.4	Overview of the batch reaction……...	64
Table 4.5	Chemical compositions of brine solutions……..	64
Table 4.6	Chemical formulas of mineral phases in XRD……...	67
Table 4.7	EDS results……..	75
Table 4.8	Results of liquid analyses……..	77
Table 4.9	Modelling results by PHREEQC……	79
Table 4.10	Calculated equilibrium mineral saturation index……	81
Table 4.11	The possible reactions of rock minerals……..	86
Table 4.12	The porosity change after the reactions……..	91
Table A.1	Properties of Pure Species……..	102

Nomenclature

a, b, c, α ----- constants in equations of state;

k_{ij} ----- binary interaction parameter;

K_{sp} ----- solubility product;

N ----- number of experimental data;

P ----- pressure;

P_b ----- bubble point pressure;

P_c ----- critical pressure;

P_d ----- dew point pressure;

R ----- the universal gas constant;

T ----- temperature;

T_c ----- critical temperature;

W_m ----- molecule weight;

x ----- mole fraction in liquid phase;

y ----- mole fraction in vapour phase.

Abbreviations

AAD ----- Absolute average deviation;

abs----- ABSOLUTE；

CCS ----- Carbon capture and storage;

EDS ----- Energy Dispersive X-ray Spectroscopy;

EOR ----- Enhanced Oil Recovery;

EOS ----- Equations of state;

IC ----- Ion-Chromatography;

ICP-MS ----- Inductively Coupled Plasma Mass Spectrometry;

IPCC ----- Intergovernmental panel on climate change;

$SCCO_2$ ----- Supercritical CO_2;

SEM ----- Scanning Electron Microscopy;

TDS ----- Total dissolved solutes;

XRF ----- X-ray Fluorescence;

XRD ----- X-ray Diffraction.

Chapter 1

Introduction

It is generally accepted that the main cause of global warming is the increase in atmospheric concentration of greenhouse gases, such as carbon dioxide (CO_2), methane (CH_4) and nitrous oxide (N_2O). From the IPCC (Intergovernmental Panel on Climate Change) report, the atmospheric concentration of CO_2 has risen from pre-industrial levels of 280 ppm to 380 ppm, in 2005. Undoubtedly, CO_2 has been becoming the primary greenhouse gas, which is responsible for about 2/3 on greenhouse effect enhancement.

Many studies were explored to seek a balance between the economic development and environmental protection. Carbon capture and geological storage (CCS) is a flexible technology aiming at reducing the atmospheric carbon dioxide. Normally, as shown in Figure 1.1, a typical CCS procedure consists of three steps: CO_2 capture, CO_2 transport and CO_2 storage.

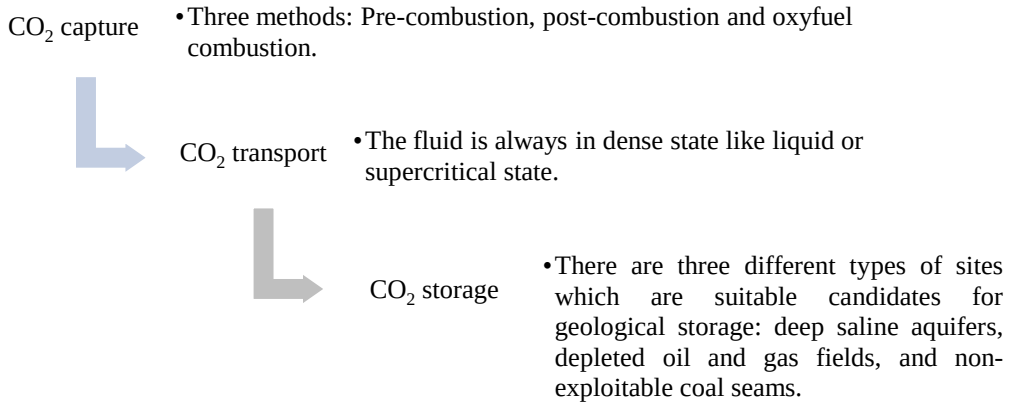

Figure 1.1 Three steps of the CCS chain.

Three different methods are applied to CO_2 capture: pre-combustion, post-combustion and oxyfuel combustion. Figure 1.2 depicts a simplified procedure of the capture system and the difference between these three methods. Pre-combustion is the technology refers to the extraction of the carbon included in the fuel before the combustion, to produce a hydrogen-

based fuel (Pehnt and Henkel, 2009). With post combustion, the CO_2 is separated after the combustion of fossil fuel. Finally, the oxyfuel combustion is performed with oxygen instead of air in order to improve the purity of CO_2.

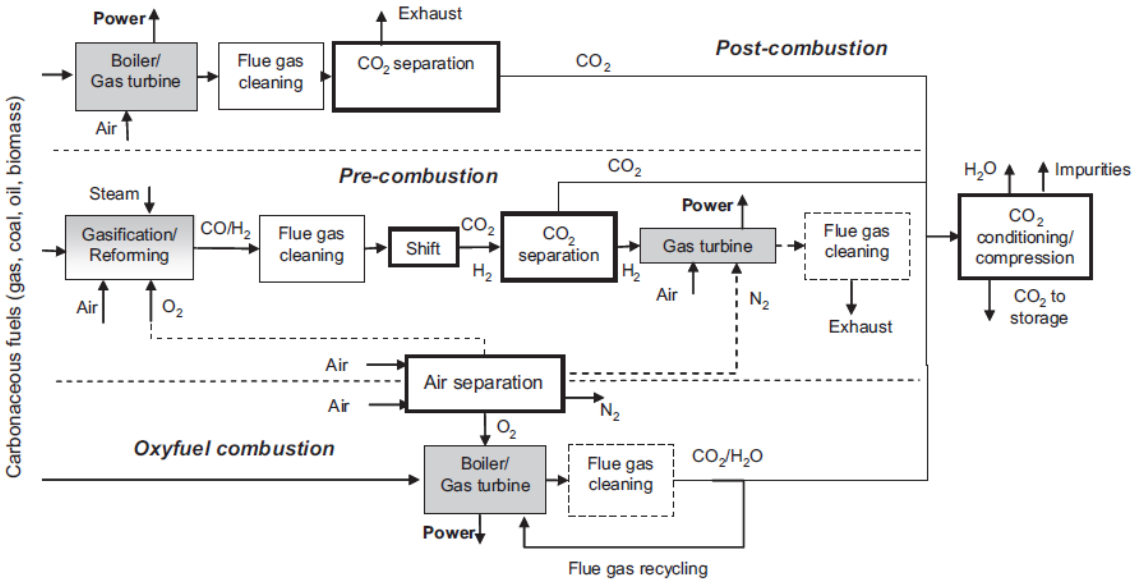

Figure 1.2 Simplified sketch of three CO_2 capture systems for power plants: post-, pre- and oxyfuel combustion. Grey components indicate power generation processes (Koornneef et al., 2012). Components with highlighted borders indicate processes causing a drop in power generation efficiency. Components with dashed borders indicate optional processes. Note that natural gas reforming using steam is an endothermic process and therefore not a power generation process, hence the altered shading.

After the CO_2 is captured, it is transported and led to a storage site. There are four possible transportation means that could be used to deliver CO_2: motor carriers, railway carriers, water carriers, and pipeline (Li and Yan, 2006).

There are three different types of sites which are suitable candidates for geological storage: deep saline aquifers, depleted oil and gas fields, and non-exploitable coal seams. Among them, deep saline aquifers, which have an estimated potential storage volume of up to 10,000 Gt CO_2 and are nearly ubiquitous worldwide, appear to be the most promising option (Jung et al., 2013). This project therefore focuses on the deep saline aquifer as a potential storage site. The injected CO_2 will be in supercritical state in deep geologic

reservoirs (>800 m) where temperatures and pressures are greater than 304 K and 7.4 MPa, respectively (Bachu, 2003; White et al., 2003).

The operating conditions of the CCS chain are designed according to the requirements of different projects, such as capture strategies, transport methods and storage structures. The operating conditions of CCS chain are estimated in Table 1.1.

Table 1.1 Estimated operating conditions of CCS (Li et al., 2011a)

CCS process	P (MPa)	T (K)
CO_2 Conditioning:	0-11	219.15-423.15
Initial compression	0-3	293.15-423.15
Dehydration	2-3	283.15-303.15
Non-condensable gas separation	2-5	219.15-248.15
Further compression/pumping	5-11	283.15-303.15
CO_2 Transport:	0.5-20	218.15-303.15
Pipeline	7.5-20	273.15-303.15
Small tanks	1.5-2.5	238.15-248.15
Large tanks	0.5-0.9	218.15-228.15
CO_2 Storage	0.1-50	277.15-423.15

1.1 Mechanisms of CO_2 trapping in CCS

CO_2 can be stored in deep saline aquifers through three different mechanisms, which are physical, chemical and hydrodynamic trappings. Physical trapping mechanisms include mobile and immobile CO_2 trapped in stratigraphic and structural traps, and at irreducible saturation in the pore space. In this case, CO_2 is stored as CO_2 molecules and remains in its chemical and physical structures. Chemical (mineral) trapping mechanism occurs in the presence of water. At the interface between the CO_2 and aquifer formation water, CO_2 is partially dissolved in the aqueous phase under high pressure and forms carbonic acid via chemical reactions. Under this circumstance, the CO_2 is stored as molecular H_2CO_3 or ionic HCO_3^- and CO_3^{2-} in the aquifer water. Additionally, the precipitation of carbonates, such as $CaCO_3$, also occurs if the concentrations of potential ions are high enough in the water system. Thus, the CO_2 would be stored as insoluble carbonate minerals. In such chemical trapping mechanism, CO_2 changes its chemical and physical structure through geochemical reactions. Hydrodynamic trapping (Bachu et al., 1994), which also known as Migration

Assisted Storage (Spencer et al., 2011) refers to the process where the injected CO_2 moves very slowly with the aquifer formation water for a long time until it is trapped by residual, solubility or mineral trapping eventually.

1.2 CCS in Canada

Generally, a regular geological survey needs to be conducted before the operation of CO_2 storage. A CCS chain should be designed with local features, while taking into consideration of the potential storage strata, possible risks and environmental impacts as well.

The total emissions of Canada's anthropogenic greenhouse gas were 690 Mt of CO_2 equivalent (Environment Canada, 2009). Based on the power and energy industrial distribution in Canada, emissions from Alberta were estimated to be 48.9%, and where 80% of electricity was generated by fossil fuel (Talman et al. 2012). To estimate the storage capacity for CO_2 in Alberta, various studies (e.g., USDOE, 2010) and surveys were initiated to explore the potential storage sites. The 2010-2011 Geological Survey of Canada (GSC) report identifies that the Alberta Basin and the Canadian part of the Williston basin are two regions with greatest storage potential for the implementation of CCS, both in terms of the storage capacity and location of large stationary resources amenable to CO_2 capture.

As discussed above, saline aquifers are the most promising site for CO_2 storage. Accordingly, the geological formation evaluated in this study is the Basal Cambrian Saline Aquifer (termed as the Basal Aquifer). Because of fossil fuel exploration in Alberta, the majority of oil and gas reservoirs are still in production. For instance, the sedimentary succession from Devonian strata to Tertiary strata is penetrated by countless wells for natural resource extraction (Talman et al. 2012). In contrast to Devonian-Cretaceous sedimentary succession, most of the Cambrian-Silurian strata in Alberta basin and in the Canadian part of Williston part does not contain fossil fuels and is penetrated by fewer wells. Therefore, this sedimentary succession could be a potential storage stratum with a lower risk of CO_2 leakage. In addition, the water salinity in this area increases with the depth. The formations composing the Basal Aquifer are hydraulically connected (hence the treatment as one storage unit), and capped by a thick succession of shale which act as the primary confining unit. These features create a situation where fresh water would be pushed up to a relatively lower depth by the high-density saline water due to the buoyancy and therefore

decrease the environmental hazards on the available natural resources. As shown in Figure 1.3, the Basal Aquifer covers the southern half of Alberta and Saskatchewan and the southwest corner of Manitoba, and extends into the Northern Plains region of the United States. The large area of the basin in combination with low permeability, lack of fossil fuels and high salinity, make the Basal Aquifer an attractive candidate for CO_2 storage.

Figure 1.3 Areal extent of the Basal Aquifer in the Northern Great Plains region of the United States and the Prairie Region of Canada (Talman et al. 2012).

1.3 Research objectives

Carbon dioxide captured from a power platform always contains various impurities such as N_2, O_2, SO_2, Ar and H_2S. The purification of this impure gas, however, is inefficient and uneconomic (Ji and Zhu, 2013). Therefore co-capture and co-injection of these impurities with CO_2 have been considered in recent studies. Impurities in CO_2 stream have the potential to physically and chemically affect the transport and storage system.

Effects on CO_2 Storage Capacity

The inclusion of impurities may cause the reduction of storage capacity not only by lowering the concentration of CO_2, but also by decreasing the density of the CO_2 stream. To quantify the change of storage capacity, density is an important parameter because it reflects the amount of CO_2 fluid that can be stored at a fixed volume. Due to the presence of non-condensable impurities, which is not be liquefied at ambient temperature, the liquefaction of CO_2 would be restricted. Therefore, a larger volume is needed to store the same amount of CO_2. The transport and storage scenario should be adjusted according to these physical changes.

Effects on Transportation

The presence of non-condensable impurities can increase the bubble-point pressure and decrease the critical temperature. A CO_2 stream with 15% Ar, simulating a high-impurity CO_2 stream from oxyfuel combustion, shows a substantial difference in phase behaviour with respect to pure CO_2, as will be seen later. Therefore, a minimum pressure of 10 MPa is needed to avoid two phase flow at all temperatures. On the other hand, if the transportation is in the liquid phase then the lower critical temperature will require a lower pipeline temperature, attained by insulation or cooling.

Chemical Effects on rock minerals and well materials

CO_2 can be partially dissolved in aquifer water to form carbonic acid under the high pressure. Some minerals could react with this acid, resulting in changes to their chemical compositions. Compared with pure CO_2, the acids formed by acid gases such as SO_x and NO_x could reduce the pH drastically due to their high acidities. Some solids, which may not readily dissolve in carbonic acid formed by pure CO_2, could dissolve in these stronger acids, resulting in more mineral dissolution compared with pure CO_2. In addition to the dissolution, precipitation may occur; the pores could be blocked by the formation of low-solubility chemical species such as $CaSO_4$. The dissolution and precipitation are two major effects on the porosity of rock minerals, which affect the injectivity for CO_2.

The effect of O_2 is mainly related to its oxidability; its inclusion would increase the formation of sulphuric acid and nitric acid. During the CO_2 storage, it could influence the composition of rock by changing their stability and solubility. Jung et al. (2013) studied the potential impact of co-injected oxygen on the interaction between the CO_2-brine and shale caprock at ~10 MPa and ~75 ℃. In the presence of oxygen, the dissolution of calcite and

dolomite was enhanced and pyrite was oxidized. These chemical processes subsequently resulted in the precipitation of Fe (III) oxides and gypsum ($CaSO_4 \cdot 2H_2O$). Their experimental and modeling results both indicated that the interaction between shale caprock and CO_2 with oxygen can exert significant impacts on brine pH, solubility of carbonate minerals, and stability of sulphide minerals.

Furthermore, the acid gases would cause corrosion on the well materials. Even though the CO_2 stream can be dried before the injection, the return of underground water or acidic impurities from pipeline would still cause the corrosion on well materials. Therefore, the well materials for transporting this impure CO_2 stream need to be more corrosive-resistant to meet the safety requirement for CCS operation.

According to the CO_2 capture strategies applied in Alberta, this project aims to elucidate of the effects of potential impurities in CO_2 on CCS, including:

- Evaluating the density changes of CO_2 stream because of impurities and the corresponding effects on the capacity and buoyancy;
- Determining the operation conditions for CO_2 transport through the prediction of phase behaviour of CO_2 mixtures, in order to avoid multiphase fluids in the transportation;
- Conducting experiments and computer simulations for the geochemical reactions between the CO_2 mixtures and aquifer water-rock system;
- Discussing the potential corrosions on pipeline materials.

The findings from literature review and data survey are used to identify key issues, uncertainties and knowledge gaps. Based on this geological information and research objectives in this section, the next chapters will outline the knowledge gaps based on the literature and current research (literature review), describe the methodologies of this study, present and discuss the results, and give conclusions of the study.

1.4 Structure of thesis

Excluding the introduction chapter (Chapter 1), this thesis mainly consists of three sections, Chapters 2, 3 and 4, in paper format.

Chapter 2 presents a literature review on the thermodynamic properties and chemical reactions pursuant to the storage of pure or impurity-containing CO_2 stream. This chapter serves to show the state of art and knowledge of gaps, which led to the definition of major research objectives.

Chapter 3 presents the experimental results and modeling data on the effects of N_2, O_2, and Ar, some most common non-condensable impurities, and SO_2, a common condensable impurity, on the physical properties of CO_2 streams. Based on the change of density with non-condensable impurities involved, the CO_2 storage capacity and buoyancy were quantified and discussed.

Chapter 4 presents the effects of SO_2 on the chemical properties of aquifer system. Additionally, the effects of O_2 were also evaluated.

Finally, Chapter 5 presents the conclusions for this thesis.

1.5 References

1. Bachu, S. 2003. "Screening and Ranking of Sedimentary Basins for Sequestration of CO2 in Geological Media in Response to Climate Change." Environmental Geology 44 (3): 277-289.

2. Bachu, S., W. D. Gunter, and E. H. Perkins. 1994. "Aquifer Disposal of CO2: Hydrodynamic and Mineral Trapping." Energy Conversion and Management 35 (4): 269-279.

3. Environment Canada, 2009. http://www.ec.gc.ca/ges-ghg/

4. Ji, X. and C. Zhu. 2013. "Predicting Possible Effects of H2S Impurity on CO2 Transportation and Geological Storage." Environmental Science and Technology 47 (1): 55-62.

5. Jung, H. B., W. Um, and K. J. Cantrell. 2013. "Effect of Oxygen Co-Injected with Carbon Dioxide on Gothic Shale Caprock-CO2-Brine Interaction during Geologic Carbon Sequestration." Chemical Geology 354: 1-14.

6. Koornneef, J., A. Ramírez, W. Turkenburg, and A. Faaij. 2012. "The Environmental Impact and Risk Assessment of CO2 Capture, Transport and Storage - an Evaluation of the Knowledge Base." Progress in Energy and Combustion Science 38 (1): 62-86.

7. Li, H., J. P. Jakobsen, Ø Wilhelmsen, and J. Yan. 2011. "PVTxy Properties of CO2 Mixtures Relevant for CO2 Capture, Transport and Storage: Review of Available Experimental Data and Theoretical Models." Applied Energy 88 (11): 3567-3579.

8. Li, H. and J. Yan. 2006. "Impacts of Impurities in CO2-Fluids on CO2 Transport Process.".

9. Pehnt, M. and J. Henkel. 2009. "Life Cycle Assessment of Carbon Dioxide Capture and Storage from Lignite Power Plants." International Journal of Greenhouse Gas Control 3 (1): 49-66.

10. Spencer, L. K., J. Bradshaw, B. E. Bradshaw, A. -L Lahtinen, and A. Chirinos. 2011. "Regional Storage Capacity Estimates: Prospectivity Not Statistics.".

11. Talman, S., Zhang, M., and Bachu, S. "Geochemical Effects of CO2 Storage in the Basal Aquifer in the Prairie Region of Canada, Phase 3" Alberta Innovates – Technology Futures 2012

12. White, C. M., B. R. Strazisar, E. J. Granite, J. S. Hoffman, and H. W. Pennline. 2003. "Separation and Capture of CO2 from Large Stationary Sources and Sequestration in Geological Formations - Coalbeds and Deep Saline Aquifers." Journal of the Air and Waste Management Association 53 (6): 645-715.

Chapter 2

Literature Review

2.1 Introduction

Carbon dioxide captured from a power platform always contains various impurities such as N_2, O_2, SO_2, Ar and H_2S. Purification of this impure gas, however, is inefficient and uneconomic (Ji and Zhu, 2013). So co-capture and co-injection of these impurities with CO_2 have been considered in recent studies. The type and amount of the impurities introduced in CO_2 depend on the fuels used and the type of capture technology. The possible impurities and their concentrations in a typical CO_2 stream are summarized in Table 2.1 and Table 2.2.

Table 2.1 Possible Impurities

Capture technology	Possible impurities	Reference
Post-combustion capture	N_2, Ar, H_2O, O_2, SO_x and NO_x	Abbas et al., 2013; Sanpasertparnich et al., 2010.
Pre-combustion capture	H_2, CO, N_2, O_2, Ar, H_2S and CH_4	Kaufmann, 2010; Cosham et al., 2010.
Oxyfuel combustion capture	N_2, O_2, SO_2, NO_x and Ar	Pipitone and Bolland, 2009.

Table 2.2 Impurity concentration (de Visser et al., 2008)

Impurity	Maximum mol%	Minimum mol%
N_2	10	0.02
O_2	5	0.04
H_2	4	0.06
CH_4	4	0.7
Ar	3.5	0.005
SO_2	1.5	< 0.0001
H_2S + COS	1.5	0.01
NO_x	0.03	0.0002
CO	0.2	0.0001

These impurities can have negative effects on CO_2 stream during transport, injection and storage. For instance, non-condensable impurities, such as N_2 and O_2, would reduce the capacity of CO_2 storage by decreasing the density of CO_2 and volume fraction, as well as decreasing the critical temperature of CO_2 and increasing the bubble-point pressure. As a result, to avoid two-phase flow, lower temperature and additional overpressure are needed in pipeline transport. In addition to physical change, impurities like SO_2 and NO_2 would form acids with water, which may react with rocks and cause corrosion on the pipeline material. Therefore, an appropriate CCS system, which is dependent on the thermodynamic properties, operating facilities and materials, should be designed according to these physical and chemical effects.

Among the various thermodynamic parameters, PVTxy is commonly used to determine the vapour-equilibrium and other volumetric properties because it can be measured directly in many cases. However, because the CO_2 storage would take place underground, there are many limitations for obtaining the actual data. Phase changes would also occur during CO_2 transport. Therefore, evaluating the thermodynamic properties and chemical reactions through modeling and simulations is important.

This chapter is a review of the experimental data and models for calculation of thermodynamic properties and chemical reactions for CO_2 streams with impurities. To select an accurate model for the prediction of volumetric properties, a brief evaluation of equations of state (EOSs) with binary parameters, k_{ij} and several other modeling methods is given. This chapter serves to show facts and knowledge gaps for the studies in the chapters that follow.

2.2 Simulation model

2.2.1 Equations of state

To evaluate the physical effects of the impurities, a model is required to predict the changes of properties such as the density, viscosity and permeability. Equations of state are mathematical formulas relating volume, pressure, temperature and composition in the case of mixture. Since van der Waals proposed the first equation of state, numerous versions with more parameters have been developed to improve the accuracy. The most common EOSs applied in CCS are given in Table 2.3.

Table 2.3 EOSs for CCS system

EOS	Form	Mixing Rule
Redlich-Kong (RK) (Redlich and Kwong, 1949)	$P = \frac{RT}{V-b} - \frac{a/T^{0.5}}{V(V+b)}$	$a = \sum_i \sum_j x_i x_j \, a_i^{\frac{1}{2}} a_j^{\frac{1}{2}} (1-k_{ij})$; $b = \sum_i x_i b_i$; $k_{ij} = k_{ji}$
Redlich-Kong-Soave (SRK) (Soave, 1972)	$P = \frac{RT}{V-b} - \frac{a\alpha}{V(V+b)}$	$a = \sum_i \sum_j x_i x_j \, a_i^{\frac{1}{2}} a_j^{\frac{1}{2}} (1-k_{ij})$; $b = \sum_i x_i b_i$; $k_{ij} = k_{ji}$
Peng-Robinson (PR) (Peng and Robinson, 1976)	$P = \frac{RT}{V-b} - \frac{a\alpha}{V(V+b)+b(V-b)}$	$a = \sum_i \sum_j x_i x_j \, a_i^{\frac{1}{2}} a_j^{\frac{1}{2}} (1-k_{ij})$; $b = \sum_i x_i b_i$; $k_{ij} = k_{ji}$
Patel- Teja (PT) (Patel and Teja, 1982)	$P = \frac{RT}{V-b} - \frac{a\alpha}{V(V+b)+c(V-b)}$	$a = \sum_i \sum_j x_i x_j \, a_i^{\frac{1}{2}} a_j^{\frac{1}{2}} (1-k_{ij})$; $b = \sum_i x_i b_i$; $c = \sum_i x_i c_i$; $k_{ij} = k_{ji}$
3P1T (Yu et al., 1987)	$P = \frac{RT}{V-b} - \frac{a\alpha}{V(V+c)+b(3V+c)}$	$a = \sum_i \sum_j x_i x_j \, a_i^{\frac{1}{2}} a_j^{\frac{1}{2}} (1-k_{ij})$; $b = \sum_i x_i b_i$; $c = \sum_i x_i c_i$; $k_{ij} = k_{ji}$
MPR (Ji and Lempe, 1997)	$P = \frac{RT}{V-b} - \frac{a}{(V+b+2c)(V+c)+(b+c)(V-b)}$	$a = \sum_i \sum_j x_i x_j \, a_i^{\frac{1}{2}} a_j^{\frac{1}{2}} (1-k_{ij})$; $b = \sum_i x_i b_i$; $c = \sum_i x_i c_i$; $k_{ij} = k_{ji}$
MSRK (Péneloux et al., 1982)	$P = \frac{RT}{V-b} - \frac{a}{(V+b+2c)(V+c)}$	$a = \sum_i \sum_j x_i x_j \, a_i^{\frac{1}{2}} a_j^{\frac{1}{2}} (1-k_{ij})$; $b = \sum_i x_i b_i$; $c = \sum_i x_i c_i$; $k_{ij} = k_{ji}$

P and T denote the pressure and temperature; R is the universal gas constant; a, b, c and α are constants in equations of state; x_i denotes the mole fraction in the liquid phase; k_{ij} denotes the binary interaction parameter.

However, these EOSs have different accuracies for the different impurities and different ranges of temperature and pressure. To evaluate the performance of EOSs in calculation of vapour-liquid equilibrium, many studies were carried out for comparison of calculated values with experimental data. The average absolute deviation percentage (AAD) is commonly used to describe the accuracy of EOS, which is defined in Eq. (1).

$$AAD = \frac{\sum abs \left| \frac{M_{cal} - M_{exp}}{M_{exp}} \right| \times 100\%}{N} \qquad (1)$$

where *abs* is the abbreviation of absolute deviation; M_{cal} and M_{exp} denote the data measured in calculation and experiment, respectively; N denotes the number of experimental data.

Generally, these EOSs were developed performing on pure species. Their applications can be extended to multiple components after defining a mixing rule. The binary interaction parameters k_{ij}, whose values can be determined from fitting the calculation results to experimental data, is an important parameter in the mixing rule. Theoretically, it is a modification of the intermolecular attraction when calculating thermodynamic properties of mixture (Li and Yan, 2009a).

2.2.2 Evaluation of EOSs

The reliability of these cubic equations of state is discussed in the literature. Li and Yan (2009a), for instance, evaluated their different performance on predicting vapour liquid equilibrium of binary CO_2-mixtures and the results are shown in Table 2.4. From this table, one can see PR, PT and SRK are generally superior to RK and 3P1T. Comparatively, PR has a better accuracy on the calculations of CO_2/CH_4 and CO_2/H_2S; PT has a better accuracy on the calculations of CO_2/O_2, CO_2/N_2 and CO_2/Ar; while 3P1T has a better accuracy on the calculations of CO_2/SO_2.

Additionally, Li and Yan also carried out an evaluation of EOS for volume calculation of CO_2-mixture in CCS system (Li and Yan, 2009b) and the results were summarized in Table 2.5. Based on these AAD values, PR and PT are generally superior to other EOSs for all the studied mixtures. Comparatively, PT has a better accuracy on the calculation of CO_2/CH_4, V_l of CO_2/H_2S, CO_2/Ar and CO_2/SO_2, and V_g of CO_2/N_2; PR has a better accuracy on the calculations of V_l of CO_2/N_2 and V_g of CO_2/Ar; MPR has a better accuracy on the calculations of V_g of CO_2/SO_2, respectively.

Table 2.4 AAD of EOSs on the calculated VLE properties of binary CO_2-mixtures (Li and Yan, 2009b)

		PR	PT	RK	SRK	3P1T
CO_2/CH_4	P_s	1.68	2.00	5.73	1.87	20.74
	$y_{s_{co_2}}$	2.63	3.14	16.71	2.79	26.95
CO_2/O_2	P_s	4.17	3.62	4.08	4.02	3.50
	$y_{s_{co_2}}$	2.89	2.74	14.90	3.44	14.13
CO_2/H_2S	P_s	1.22	1.48	3.41	1.32	3.32
	$y_{s_{co_2}}$	4.54	4.28	9.28	4.49	4.79
CO_2/N_2	P_s	2.08	1.62	4.08	1.79	3.10
	$y_{s_{co_2}}$	2.23	2.17	5.25	2.83	13.15
CO_2/Ar	P_s	2.88	2.85	5.43	3.36	9.79
	$y_{s_{co_2}}$	-	-	-	-	-
CO_2/SO_2	P_s	4.64	4.67	10.62	4.28	4.17
	$y_{s_{co_2}}$	-	-	-	-	-

P_s denotes saturated pressure; $y_{s_{co_2}}$ denotes saturated vapour composition of CO_2.

Table 2.5 AAD of EOSs on both gas and liquid volume of various binary CO_2-mixtures (Li and Yan, 2009b)

		PR	PT	RK	SRK	MPR	MSRK
CO_2/CH_4	V_g	2.95	2.34	2.56	2.56	4.49	3.97
	V_l	4.17	3.70	5.19	5.12	5.50	6.08
CO_2/H_2S	V_g	4.71	5.57	8.84	7.34	3.37	4.26
	V_l	3.03	2.43	4.95	4.18	4.30	4.97
CO_2/N_2	V_g	1.58	0.98	1.47	1.50	2.85	2.59
	V_l	1.74	1.77	5.97	4.99	3.79	6.16
CO_2/Ar	V_g	5.96	6.08	6.43	6.45	7.21	7.16
	V_l	2.37	2.12	4.86	4.66	3.99	5.48
CO_2/SO_2	V_g	13.02	13.06	14.26	14.00	11.64	12.76
	V_l	9.43	9.28	11.96	10.84	10.51	12.15

V_g denotes gas volume; V_l denotes liquid volume.

In addition, Thiery et al. (1994) studied the VLE and volume calculation of binary and ternary CO_2 mixtures by using SRK EOS. The average deviation of P_s was around 1% for CO_2/CH_4 system, 4% for CO_2/N_2 system and 2-3% for $CO_2/CH_4/N_2$ system.

Chapoy et al. (2013b) investigated the phase behaviour of CO_2-rich system (O_2, Ar, N_2 and water) of CCS by using SRK EOS at range from 252.65 K to 293.35 K and 7.10 MPa to 8.96 MPa. The comparison of the experimental data with calculated results showed that SRK model could predict the phase envelope of the multicomponent systems with a good accuracy, the predictions are in better agreement at higher temperature conditions.

2.2.3 Other specific models

Some specific models were developed for research requirements to improve the accuracy in evaluating a special physical property.

Chapoy et al. (2013b) provided a model to simulate the effect of impurities on thermophysical properties and phase behaviour of CO_2 mixture. A corresponding-state viscosity model was developed to predict the viscosity of the stream, and a volume corrected equation of state approach was used to calculate densities.

A new EOS was developed by Ziabakhsh-Ganji and Kooi (2012) based on equating the chemical potentials in the system by using PR EOS to calculate the fugacity of the gas phase. It performs favourably with respect to existing EOS's and experimental data for single gas systems and accurately reproduces available data sets for gas mixtures.

Duan and Hu (2004) developed another EOS for both pure and mixture system. Compared with the general EOSs, their equation has only one empirical constant to be evaluated for each component and two constants for each binary mixture. The reliability was investigated by the comparison with the most frequently used EOS, and results indicated that this new equation is superior to the previous cubic equations in the overall performance in the calculation of vapour pressures and saturated volumes.

2.3 Survey of experimental data

2.3.1 PVTxy

Many studies were carried out for the thermodynamic properties of CO_2-mixtures and mainly focused on the impurities like O_2, N_2, CH_4, and H_2S. Furthermore, the calibration of

k_{ij} requires a large amount of experimental data. Table 2.6 summarizes experimental conditions from literature.

Table 2.6 Summary of the experimental conditions for CO_2-mixtures

CO_2 Mixture	Temperature (*K*)	Pressure (*MPa*)	Source
		Binary Mixture	
CO_2/N_2	270	3-12	Somait and Kidnay, 1978
	219.26-270	0.58-16.15	Al-Sahhaf et al., 1983
	223.15-273.15	3-20	Dorau et al., 1983
	273.2-298.2	4.5-8.14	Yorizane et al., 1985
	323-348	50-250	Hacura et al., 1988
	300 and 320	0.1-10.6	Brugge et al., 1989
	250-330	2.3-32	Ely et al., 1989
	205-320	0.1-48	Esper et al., 1989
	288 and 298	5.11-9.11	Xu et al., 1992
CO_2/O_2	213-260	3.7-14.5	Booth and Carter, 1930
	223.15-283.15	1-13	Fredenslund and Sather, 1970
	223.75	0.9-14.1	Fredenslund et al., 1972
CO_2/H_2S	258-313	1.0-5.5	Chapoy et al., 2013a
	303.15-383.15	4.0-40	Ji and Zhu, 2013
CO_2/CH_4	230-250	0.9-8.5	Davalos et al., 1976
	219.26-270	0.58-16.15	Somait and Kidnay, 1978
	225-400	2-35	Magee and Ely, 1988
	300 and 320	0.1-10.6	Brugge et al., 1989
	250-330	2.3-3.2	Ely et al., 1989
	288 and 293	5.11-9.11	Xu et al., 1992
	253.15-333.15	2-26	Blanco et al., 2012
CO_2/H_2	278.15-290.15	4.8-19.2	Bezanehtak et al., 2002
CO_2/Ar	293.15-303.15	0.101-2.58	Kestin et al., 1966
CO_2/CO	323.15-423.15	0-6.5	Mallu et al., 1987
		Ternary Mixture	
$CO_2/CH_4/N_2$	219.26-270	0.58-16.15	Al-Sahhaf et al., 1983
	303.15-333.2	3.79-12.64	McElroy et al., 1989
	220	2-12	Trappehl and Knapp, 1989
	230-250	6.21-10.34	Al-Sahhaf, 1990
	323.15-523.15	19.9-99.9	Seitz and Blencoe, 1996
$CO_2/CH_4/H_2S$	222-238.75	2.1-4.8	Hensel Jr. and Massoth, 1964

2.3.2 Binary interaction parameter, k_{ij}

Binary interaction parameter is an important constant in the mixing rule. Usually, k_{ij} is considered to be independent of temperature, pressure and composition (Danesh et al., 1991; Von Solms et al., 2002). In order to improve the accuracy of EOS, many studies were carried out to calibrate k_{ij}. For instance, Chapoy et al. (2013a) calibrated k_{ij} of PR and SRK EOSs in CO_2/H_2S system. Furthermore, they pointed out that the k_{ij} parameters have a weak quadratic temperature dependency.

Simulation software such as like PRO/II (developed by Invensys Software) also contains k_{ij} values in their databanks, which were used in many studies.

A systematic study of k_{ij} was conducted by Li and Yan (2009a); they calibrated k_{ij} values for different EOSs in different binary impurity system and their results are shown in Table 2.7.

Table 2.7 Calibrated k_{ij} for different binary CO_2-mixture (Li and Yan, 2009a)

	PR	PT	RK	SRK	3P1T
CO_2/CH_4	0.100	0.905	0.079	0.105	-0.034
CO_2/O_2	0.114	0.899	0.168	0.116	0.105
CO_2/H_2S	0.099	0.892	0.083	0.106	0.098
CO_2/N_2	-0.007	1.036	0.102	-0.014	-0.026
CO_2/Ar	0.163	0.882	-0.076	0.180	0.140
CO_2/SO_2	0.046	0.952	-0.041	0.048	0.083

2.4 Physical effects

2.4.1 Phase behaviour

Phase behaviour is important to transportation and injection process because two-phase flow in the pipeline could cause cavitation and pressure peaks, which would most likely damage the pipeline (Nimtz et al., 2010). Besides, two-phase flows are problematic in the operation of pumps, compressors and injection wells (Zirrahi et al., 2010). For a mixed fluid, the phase behaviour depends on the composition, temperature and pressure. Therefore, many studies focused on the phase behaviour to determine proper operation conditions.

Wang et al. (2011) showed that the effects on the critical temperature and pressure are quite different for different impurities. N_2, O_2, Ar and H_2 generated the greatest increase in the saturation pressure of the liquid and greatest decrease in the critical temperature, respectively. With the presence of 5.8% N_2, 4.7% O_2, 4.47% Ar and other impurities at ppm level, the critical temperature decreased by about 10 °C in comparison with that of pure CO_2, and the liquefaction pressure increased by over 50 bar. On the other hand, SO_2 had the opposite effect: it caused an increase in critical temperature and a decrease in liquefaction pressure.

Huh et al. (2011) studied the CO_2-N_2 behaviour at 70 bar and 21 °C, with N_2 mass fraction controlled from 0 to 9.35%. The CO_2-N_2 mixture was in a single phase of liquid state at mass fraction from 0 to 1.44%, and show two-phase behaviour from 2.08 to 4.55% and single gaseous phase behaviour from 5.25 to 9.35%.

Ji and Zhu (2013) predicted possible effects of H_2S impurity on CO_2 transportation and storage. The critical pressure of gas mixture increased with in presence of H_2S. Additionally, increasing levels H_2S resulted in decreased P_b and P_d at a given temperature, which implies a decrease in the minimum operation pressure for gas pipeline. P_b and P_d increased with elevated temperatures, requiring an increase of pressure level for high-pressure transportation in order to avoid two-phase flow. Finally, an increased temperature avoided phase split in a wide range of H_2S concentration, which is important to transportation and injection.

Chanpoy et al. (2013b) studied the effects of impurities on phase behaviour of a CO_2-rich (O_2, Ar, N_2 and water) system at temperature range from 253 K to 293 K. The results showed that the single liquid phase region of CO_2-rich mixture is 3-5 MPa, which is higher than that of pure CO_2 in the literature temperature ranges.

2.4.2 Density and normalized CO_2 storage capacity

The density of gas-mixture, which is a function of temperature, pressure and composition, is an important parameter in the evaluation of CO_2 transportation and storage capacity because it reflects the amount of fluid that could be stored at a fixed volume. After injection, CO_2 will be in the supercritical state and impurities will affect the volumetric properties of the fluid.

The effects of H_2S impurity on density of CO_2-H_2S mixture at pressures ranging from 40 to 400 bar were illustrated in the study of Ji and Zhu (2013). At 303.15 K, the mole density of the fluid increased with increasing H_2S concentration, while the mass density increased at low pressure but decreased at high pressure. Because the mass density of CO_2 mixture increased at low pressures, the mole volume of the mixture decreased. As a result, the amount of gas that can be stored in a same volume increased.

Chapoy et al. (2013b) measured the density of multicomponent (O_2, Ar and N_2) mixture with 10% impurity at different pressures and temperatures in gas, liquid and supercritical regions. They also predicted the density change by using SRK EOS and compared the results with experimental data. The results are plotted in Figure 2.1. Additionally, Figure 2.2 shows the difference between the densities of multicomponent mixture and pure CO_2 at 323.48 K. The density can be reduced by as much as 35% at the same temperature and pressure than pure CO_2, which can have a significant impact on transportation costs.

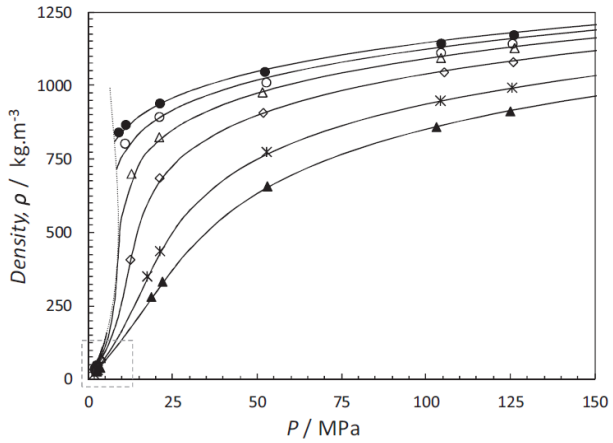

Figure 2.1 Predicted and experimental density of the multicomponent CO_2-rich stream. Black lines: Predictions using the corrected SRK-EOS model.
This work: (●) T = 273.26 K, (○) T = 283.31 K, (Δ) T = 298.39 K, (◊) T = 323.48 K, (*) T= 373.54 K, (▲) T = 423.43 K (Chapoy et al., 2013b).

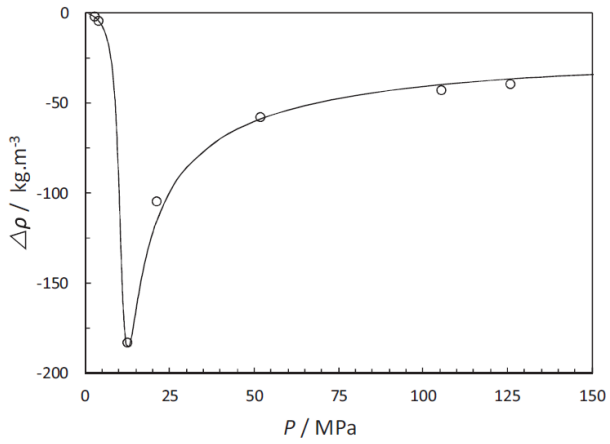

Figure 2.2 Predicted and experimental density difference: $\Delta\boldsymbol{\rho} = \boldsymbol{\rho}^{\mathbf{mix}} - \boldsymbol{\rho}^{\mathbf{CO_2}}$, between the multicomponent CO_2-rich stream and pure CO_2 density at 323.48 K. Black lines: Predictions using the corrected SRK-EOS model. This work: (○) T = 323.48 K (Chapoy et al., 2013b).

Wang et al. (2012) investigated the effects of impurities on the CO_2 density and pointed out this effect would increase with increasing the concentration of impurities. Figure 2.3 shows their results calculated by PR equation for high impurity oxyfuel CO_2 at 330 K. It can be seen that the non-condensable gas impurity significantly reduce the density of CO_2 stream, due to the fact that non-condensable impurities are less dense than CO_2 and hence take a greater volume.

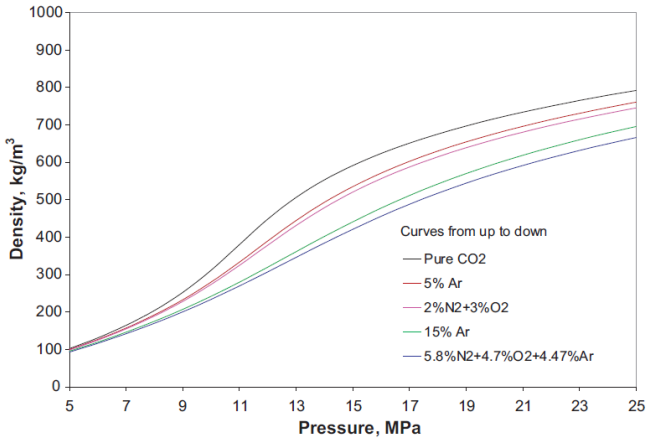

Figure 2.3 Calculated densities for CO_2 and CO_2 mixtures as a function of pressure at 330 K (Wang et al., 2012).

Furthermore, they quantified the effect of impurities on CO_2 storage capacity by developing the normalized storage capacity equation, which is shown in Eq. (2).

$$\frac{M}{M_0} = \frac{\bar{\rho}}{\rho_0(1 + \sum_i m_i/m_{co_2})} \qquad (2)$$

where M and M_0 denote the mass of CO_2 in the mixture and in the pure stream, which occupy the same volume, $\bar{\rho}$ and ρ_0 are the density of the mixture and the pure stream, and m_i/m_{co_2} is the ratio of the mass of impurity i to the mass of CO_2 in the mixture. The ratio M/M_0 on the left-hand side of the equation, which can also be viewed as the ratio of the mass of CO_2 per unit volume in the mixture to that in the pure state, represents a normalized storage capacity. The results are plotted in Figure 2.4.

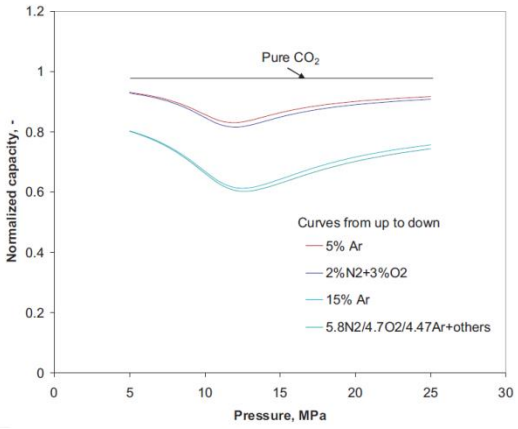

Figure 2.4 Normalized CO_2 storage capacities at 330 K (Wang et al., 2012).

2.4.3 Permeation

Darcy's Law is a phenomenologically derived constitutive equation that describes the flow of a fluid through a porous medium and is also used to analyze the physical effects of impurities on CO_2 permeation with the rocks. The form of Darcy's Law which can be used in the application of CCS is shown in Eq. (3).

$$\dot{M} = \frac{-\rho k}{\mu} \nabla p \qquad (3)$$

where $\dot{M}$ is the mass flow per unit area, ρ is the density of injected stream, k is rock permeability, ∇ is the gradient operator, p is the pressure, and μ is the viscosity of the fluid.

The mass flux is a function of density and viscosity. It will change in the presence of impurities due to the change of density and viscosity, which also depend on temperature and pressure. If the impurities reduce the density of CO_2 stream, the mass flux will decrease for the same pressure gradient. The impurities also affect the viscosity of the fluid. When the viscosity of the impure CO_2 stream is lower than the viscosity of pure CO_2, the flux will increase. Hence the decrease in density may be compensated by a corresponding decrease in viscosity. Wang et al. (2011) proposed an expression for normalized permeation flux to describe the effect of impurities, as shown in Eq. (4).

$$\frac{\dot{M}_{CO_2}}{\dot{M}_0} = \frac{\rho\left(\frac{\mu_0}{\mu}\right)}{\rho_0\left(1+\sum_i \frac{m_i}{m_0}\right)} \qquad (4)$$

where $\dot{M}_{CO_2}$, μ, and ρ are the mass flow per unit area, viscosity, and density of the CO_2 mixture, and $\dot{M}_0$, μ_0, and ρ_0 are those of the pure CO_2. Their calculated result for the high impurity CO_2 stream (with about 15% N_2/O_2/Ar and other minor-quantity impurities) shows that the permeation flux is lower than that of pure CO_2 by more than 15% at lower pressures.

Afterwards, Blanco et al. (2012) investigated the permeation flux of two CO_2 streams, $x_{CO_2} = 0.8525$ and $x_{CO_2} = 0.9902$, with methane as the impurity by using the same normalized permeation flux equation. From the results, which are shown in Figure 2.5, at the pressure range from 10 to 20 MPa, the permeation fluxes of these two mixtures were higher than that for pure CO_2 at 293.15 and 308.15 K. At 333.15 K the trend changed, and the permeation flux of the mixture with lowest CO_2 fraction was lower than that of pure CO_2, approaching unity as pressure increased; for the other mixture, the permeation flux was lower than one up to 14 MPa, and approximately equals one from this pressure.

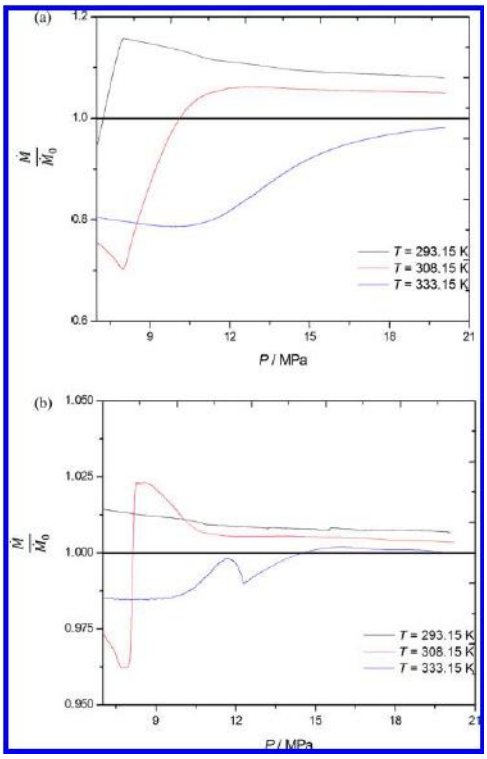

Figure 2.5 Normalized permeation flux, $\dot{M}_{CO_2}/\dot{M}_0$, for CO_2 + CH_4 mixtures with (a) $x_{CO_2} = 0.8525$ and (b) $x_{CO_2} = 0.9902$ at 293.15, 308.15, and 333.15 K (Blanco et al., 2012).

2.5 Chemical effects

Among the various impurities, H_2S, SO_2 and NO_2, which can form acids with the presence of water, are most common reactive gases. CO, which is highly reductive, will be oxidized to CO_2 by oxygen or mineral oxides. During the whole CCS, many chemical reactions could occur, depending on the type and concentration of the impurities.

2.5.1 Possible mineral in reservoirs

To simulate the chemical reaction of CO_2 stream with the rock in underground, batch experimental system of CO_2-brine-rock sample at certain pressure and temperature is commonly used. Analysis and determination of the possible minerals and solutes, which can be obtained from the analytical results of the initial samples or geochemical simulation, is an important step before the experiment.

NaCl brine is commonly used to provide an aqueous environment in batch experiments (Jung et al., 2013; Crandell et al., 2010; Wigand et al., 2008), because NaCl is usually the

main salt in saline aquifers (Ji and Zhu, 2013). Some studies applied special brines with multicomponent brine to simulate the chemical solution. Table 2.8 summarizes the possible solid minerals and aqueous ions in different cases. These results can be used as references in the design of simulations for chemical reactions.

Table 2.8 Possible minerals for simulation of geochemical reactions

Dissolved Species	Rock sample Analysis	Depth	Source
NaCl.	Quartz, calcite, dolomite, montmorillonite and prite. (Si, Ca, Al, Mg, C, Fe, K and S)	1640 m	Jung et al., 2013
Al^{3+}, Ba^{2+},Sr^{2+}, Ca^{2+}, CO_2(aq), Fe^{2+}, K^+, Mg^{2+}, Na^+, SiO_2(aq), Cl^-, SO_4^{2-}, O_2(aq).	Quartz (SiO_2), K-feldspar ($KAlSi_3O_8$), Illite/muscovite ($KAl_3Si_3O_{10}(OH)_2$), Calcite ($CaCO_3$), Kaolinite ($Al_2(Si_2O_5)(OH)_4$), Chlorite/Mg-clinochlore ($Mg_5Al_2Si_3O_{10}(OH)_8$), Labradorite ($Na_8Ca_6Al_2Si_2O_8$), Pyrite (FeS_2).	1500 m	Ghomian et al., 2008; Knauss et al., 2005
NaCl.	Halite, Kaolinite, Montmor-Na, Quartz, Albite, K-feldspar, Dolomite, Siderite, Phlogopite, Illite, Clinochlore.	1500-2000 m	Wigand et al., 2008
Al^{3+}, Ba^{2+},Sr^{2+}, Ca^{2+}, Fe, K^+, Mg^{2+}, Na^+, SiO_2, HCO_3^-, Cl^-, SO_4^{2-}.	----------	~1400 m	Wilkin and Digiulio, 2010
HCO_3^-, SO_4^{2-}, Cl^-, Na, K, Mg, Ca, Si, Al.	Quartz (SiO_2), K-feldspar ($KAlSi_3O_8$), Anorthite ($CaAl_2Si_2O_8$), Albite-low ($NaAlSi_3O_8$), Ca-montmorillonite ($Ca_{0.165}Mg_{0.33}Al_{1.67}Si_4O_{10}(OH)_2$), Calcite ($CaCO_3$), Gypsum ($CaSO_4{\cdot}2H_2O$), Kaolinite ($Al_2(Si_2O_5)(OH)_4$).	1100 m	Mito et al., 2013
Ca, Cl, K, Mg, Na, Si, S, C, Al.	Dolomite, Quartz, K-feldspar, Anhydrite, Illite, Kaolinite.	2477 m	Zhu et al., 2013

2.5.2 Formation of acid and dissolution of solid minerals

2.5.3 Pure CO_2

To evaluate the chemical effects of impure CO_2 on the reservoirs, the effects of pure CO_2 need be evaluated first for comparison. With the reaction shown in Eq. (5),

$$CO_2 + H_2O \leftrightarrow 2H^+ + CO_3^{2-} \quad (5)$$

pure CO_2 forms carbonic acid, which lowers the pH in the presence of water. As a result, the dissolution of dolomite, calcite etc., which are main components of rock, increases with increasing of concentration of CO_2. Due to different possible minerals, it is necessary to perform evaluations for specific type of reservoir before storage of CO_2. This work has been done by many studies over the past ten years.

To assess the potential effect of CO_2 releases into potable aquifers in terms of trace metal mobilization and transportation, Wang and Jaffe (2004) developed a numerical model to simulate this chemical process. The results showed that the intrusion of CO_2 into the potable aquifer may cause negative effects on groundwater quality by decreasing the pH and enhancing mineral dissolution of trace metals if the aquifer contains these mineral metal species. However, the effects can be significantly decreased in aquifers with high alkalinity and pH buffering capacity such as calcite bearing aquifers.

Kharaka et al. (2006) investigated the CO_2-water-rock interactions by analysis of the real CCS case and geochemical simulation. Before CO_2 injection, the initial sample showed Na-Ca-Cl–type brine with 93,000 mg/L total dissolved solutes (TDS). With CO_2 incursion, samples showed sharp drops in pH (6.5–5.7), pronounced increases in the dissolution of Fe (30–1100 mg/L), Ca and dissolved inorganic carbon (DIC). Geochemical modeling suggests that the pH would have dropped lower but for the buffering by dissolution of carbonate and iron oxyhydroxides. Additionally, this rapid dissolution of carbonate and other minerals could ultimately create pathways in the rock seals or well cements for CO_2 and brine leakage.

Wilgand et al. (2008) examined the geochemical reaction between the brine (1 M NaCl) and supercritical CO_2 ($SCCO_2$) on the reservoir rock (saline aquifers) by experimental simulation. The final analyses indicate that the injection of $SCCO_2$ caused a decrease of pH and the most of major elements (e.g. Ca, Mg, Fe, Mn) of the sandstone increase in

concentration during the reaction. These results are supported by scanning electron microscopy (SEM) which shows the dissolution of dolomite cement, K-feldspar and albite.

2.5.4 Impure CO_2

Like pure CO_2, impure CO_2 can also cause changes in pH and dissolution of reservoir minerals during CO_2 storage. As mentioned above, SO_x and NO_x would react with water and form sulphuric acid and nitric acid respectively, which can decrease pH drastically due to their high acidities. Possible chemical reactions are shown in Eq. (6) and (7):

$$2SO_2 + 2H_2O + O_2 \rightarrow 2H_2SO_4 \qquad (6)$$

$$4SO_2 + 4H_2O \rightarrow 3H_2SO_4 + H_2S \qquad (7)$$

Accordingly, higher dissolution of rock minerals occurs compared with the case of pure CO_2. For instance, Wilke et al. (2012) evaluated and compared the geochemical impact of pure and impure CO_2 (SO_2 and NO_2, respectively) on rock forming minerals of possible CO_2 storage reservoirs. They simulated the chemical reaction by developing a batch experiment of $SCCO_2$-brine-rock forming mineral system, and analysed by XRD, XRF, SEM and EDS for the solid, and ICP–MS and IC for the fluid reactants, respectively. Final results showed that the dissolution of carbonates can be microscopically characterized with both pure and impure $SCCO_2$. For pure CO_2 a pH of around 4 was observed with silicates and anhydrite, and 7–8 with carbonates. However, the presence of SO_2 or NO_2 in CO_2 stream caused the formation of H_2SO_4 or HNO_3, reflected in pH values between 1 and 4 for experiments with silicates and anhydrite and between 5 and 6 for experiments with carbonates.

These acids will be responsible for the large amount of cations dissolved from the mineral phases compared the pure CO_2 group. In addition to the dissolution on rock minerals, these reactive impurities will increase the corrosion on the pipeline materials. Special operating conditions and equipment need to be considered for carrying out the CCS project. Some studies were conducted to investigate the chemical effects of reactive impurities on the well materials and reservoir (Knauss et al., 2005; Gunter et al., 2000; Xu et al., 2007; Jacquemet et al., 2009).

2.5.5 Redox reaction by possible oxides in gas mixture

Some oxidants, like oxygen, would increase the acidity or accelerate the formation of sulphuric acid via the reaction shown in Eq. (6). During the CO_2 storage, oxides could influence the composition of rock by changing their stability and solubility. For instance, Jung et al. (2013) studied the potential impact of co-injected oxygen on the interaction between the CO_2-brine and shale caprock at ~10 MPa and ~75 ℃. In the presence of oxygen, the dissolutions of calcite and dolomite were enhanced and pyrite was oxidized. And these chemical processes subsequently resulted in the precipitation of Fe (III) oxides and gypsum ($CaSO_4 \cdot 2H_2O$). Their experimental and modeling results both indicated that the interaction between shale caprock and CO_2 in the presence of oxygen can impact significantly the pH of brine, solubility of carbonate minerals, and stability of sulphide minerals.

2.5.6 Effects of SO_2 on the porosity of reservoir

In addition to increasing the dissolution of mineral, sulphuric acid formed by SO_2 and water can also influence the porosity via the formation of calcium sulphate (Bacon et al., 2009), which is shown in Eq. (8).

$$Ca^{2+} + SO_4^{2-} \rightarrow CaSO_4 \qquad (8)$$

To evaluate the porosity change, it is important to determine whether dissolution or precipitation is the dominating process. Two possible mechanisms of calcium sulphate formation are shown below.

(1) SO_2 dissolves into water and forms the H_2SO_4, lowering the pH and causing the dissolution of minerals. At the beginning of injection, the dissolution is dominant because the concentration of cations is low. The solid minerals are dissolved to ions and pushed by CO_2 stream. So the porosity would be increased by the dissolution.

To determine the concentration where the precipitation will start, one can introduce the solubility product K_{sp}, which is also equilibrium constant for dissolutions of a solid ionic compound to ions in aqueous. Eq. (9) and Eq. (10) show the equations for solubility of calcium sulphate.

$$CaSO_4 \leftrightarrow {Ca^{2+}}_{(aq)} + {SO_4^{2-}}_{(aq)} \qquad (9)$$

$$K_{sp} = [Ca^{2+}] \times [SO_4^{2-}] \qquad (10)$$

The solubility product of calcium sulphate is K_{sp} = 4.93×10^{-5} mol^2L^{-2}. Once the concentration of the dissolved species reaches the level for sulphates to precipitate, where the product of concentrations of calcium ions and sulphate ions is higher than 4.93×10^{-5} mol^2L^{-2}, that is:

$$\left[Ca^{2+}\right] \times \left[{SO_4}^{2-}\right] > 4.93 \times 10^{-5}\, mol^2/L^2 \quad (11)$$

the precipitation starts. Then the porosity would be affected by both the dissolution and precipitation.

(2) Because supercritical CO_2 does not mix with water, the water is displaced by injected CO_2 stream. And this results in the formation of a dry-out zone starting from the injection well (André et al., 2007; Pruess and García, 2002). Without the presence of water, SO_2 reacts with calcium carbonate and oxygen and form calcium sulphate via the Eq. (12).

$$CaCO_3 + SO_2 + \frac{1}{2}O_2 \rightarrow CaSO_4 + CO_2 \quad (12)$$

At low to moderate temperatures, this reaction would be very slow.

Generally, the dissolution and precipitation would happen simultaneously. To study this effect on the porosity, the different situations of chemical environment need to be discussed. If the CO_2-SO_2 stream has NO_2 as an additional impurity, the nitric acid also forms together with sulphuric acid and cause dissolution. Compared with the CO_2-SO_2 system, more dissolution will occur in this case. If calcium compounds such as calcite and dolomite are the main components of the reservoir rocks, more calcium sulphates could form and reduce the pore volume of the reservoir rock as a result of SO_2.

However, the rates of mineral alternation are very low and the evaluation of real cases is difficult. In addition to several field case studies (Kharaka et al., 2006; Gunter et al., 1996; Bachu et al., 2005; Bacon et al., 2009), which show that the mineral trapping causes the porosity loss, many studies were performed by computer simulations (Knauss et al., 2005; Gunter et al., 2000; Jacquemet et al., 2009; Crandell et al., 2010; Li et al., 2011b).

For instance, Xu et al.'s work (2007) developed a numerical model and pointed out that the injection of acid gases and the resulting mineral alteration led to changes in porosity, and

a small change in porosity results in a significant change in permeability, which could modify fluid flow. Porosity increased significantly in the acidified zones where mineral dissolution dominates. With co-injection of SO_2, the porosity increased from an initial 30% to 43% after 100 years in acidified zones. However, within the CO_2 mineral-trapping zone, the porosity decreases to about 0.28 for the case of CO_2 and SO_2, because of the precipitation of secondary carbonates in the rock matrix.

Due to the dual effect of SO_2 on the porosity, the precipitation of sulphates can be offset by the dissolution of other minerals. For instance, Gunter et al. (2000) studied the interaction of CO_2, SO_2 and H_2S stream with the minerals in typical carbonate and sandstone aquifers from the Alberta Basin. Their results showed that the dissolution caused by acids can be offset by the formation of new mineral products in the chemical process, such as calcite, siderite, anhydrite/gypsum and pyrrhotite. In addition, Bacon et al. (2009) performed a geological model to simulate the chemical reaction between the acids gas and rock minerals. The results showed that the greatest change in calcite mass was a decrease of 0.4%, and the greatest change in dolomite mass was a decrease of 0.0087%. These changes in mass are not sufficient to cause a noticeable change in porosity or permeability of the formation.

2.6 Knowledge gaps

Based on the literature review in this chapter, there are several identifiable knowledge gaps in the literature:

(1) Even though the effects of SO_2 on the physical and chemical properties were simulated in many studies, the reference to real experiments for SO_2 is limited;

(2) To reduce the cost of CCS industrial application, co-injection and co-storage of the impurities with CO_2 have been considered in recent studies. However, the research on high concentration (~15%) of impurities as in the CO_2 streams from oxyfuel combustion is lacking;

(3) The high impurity CO_2 streams from oxyfuel combustion contain N_2, O_2 and Ar from air. It is speculated that Ar could be used to represent the total air-derived impurities in studying the behaviour of the impure CO_2 streams (Wang et al., 2011). However, this has not been verified.

(4) The possibilities of operating CCS in Alberta, Canada have not been comprehensively studied.

The next chapters will introduce the methodologies used in the research of physical and chemical effects of high-concentration impurities on CO_2 geological storage. According to the results provided by the simulations and experiments, these effects were quantified by different parameters. Finally, based on the geological survey and the situation of greenhouse emission in Canada, the possible operation conditions were estimated.

2.7 References

1. Abbas, Z., T. Mezher, and M. R. M. Abu-Zahra. 2013. "CO2 Purification. Part I: Purification Requirement Review and the Selection of Impurities Deep Removal Technologies." *International Journal of Greenhouse Gas Control* 16: 324-334.

2. Al-Sahhaf, T. A. 1990. "Vapor-Liquid Equilibria for the Ternary System N2 + CO2 + CH4 at 230 and 250 K." *Fluid Phase Equilibria* 55 (1-2): 159-172.

3. Al-Sahhaf, Taher A., Arthur J. Kidnay, and E. Dendy Sloan. 1983. "LIQUID Plus VAPOR EQUILIBRIA IN THE N//2 Plus CO//2 Plus CH//4 SYSTEM." *Industrial & Engineering Chemistry, Fundamentals* 22 (4): 372-380.

4. André, L., P. Audigane, M. Azaroual, and A. Menjoz. 2007. "Numerical Modeling of Fluid-Rock Chemical Interactions at the Supercritical CO2-Liquid Interface during CO2 Injection into a Carbonate Reservoir, the Dogger Aquifer (Paris Basin, France)." *Energy Conversion and Management* 48 (6): 1782-1797.

5. Bachu, S. et al. 2005. *Deep Injection of Acid Gas in Western Canada*. Developments in Water Science. Vol. 52.

6. Bacon, D. H., B. M. Sass, M. Bhargava, J. Sminchak, and N. Gupta. 2009. "Reactive Transport Modeling of CO2 and SO2 Injection into Deep Saline Formations and their Effect on the Hydraulic Properties of Host Rocks.".

7. Bezanehtak, K., G. B. Combes, F. Dehghani, N. R. Foster, and D. L. omasko. 2002. "Vapor-Liquid Equilibrium for Binary Systems of Carbon Dioxide + Methanol, Hydrogen + Methanol, and Hydrogen + Carbon Dioxide at High Pressures." *Journal of Chemical and Engineering Data* 47 (2): 161-168.

8. Blanco, S. T., C. Rivas, J. Fernández, M. Artal, and I. Velasco. 2012. "Influence of Methane in CO2 Transport and Storage for CCS Technology." *Environmental Science and Technology* 46 (23): 13016-13023.

9. Booth, H. S. and J. M. Carter. 1930. "The Critical Constants of Carbon Dioxide-Oxygen Mixtures." *Journal of Physical Chemistry* 34 (12): 2801-2825.

10. Brugge, H. B., C. -A Hwang, W. J. Rogers, J. C. Holste, K. R. Hall, W. Lemming, G. J. Esper, K. N. Marsh, and B. E. Gammon. 1989. "Experimental Cross Virial Coefficients for Binary Mixtures of Carbon Dioxide with Nitrogen, Methane and Ethane at 300 and 320 K." *Physica A: Statistical Mechanics and its Applications* 156 (1): 382-416.

11. Chapoy, A., C. Coquelet, H. Liu, A. Valtz, and B. Tohidi. 2013a. "Vapour-Liquid Equilibrium Data for the Hydrogen Sulphide (H2S)+carbon Dioxide (CO2) System at Temperatures from 258 to 313K." *Fluid Phase Equilibria* 356: 223-228.

12. Chapoy, A., M. Nazeri, M. Kapateh, R. Burgass, C. Coquelet, and B. Tohidi. 2013b. "Effect of Impurities on Thermophysical Properties and Phase Behaviour of a CO2-Rich System in CCS." *International Journal of Greenhouse Gas Control* 19: 92-100.

13. Cosham, A., R. J. Eiber, and E. B. Clark. 2010. "Gasdecom: Carbon Dioxide and Other Components.".

14. Crandell, L. E., B. R. Ellis, and C. A. Peters. 2010. "Dissolution Potential of SO2 Co-Injected with CO2 in Geologic Sequestration." *Environmental Science and Technology* 44 (1): 349-355.

15. Danesh, A., D. -H Xu, and A. C. Todd. 1991. "Comparative Study of Cubic Equations of State for Predicting Phase Behaviour and Volumetric Properties of Injection Gas-Reservoir Oil Systems." *Fluid Phase Equilibria* 63 (3): 259-278.

16. Davalos, J., W. R. Anderson, R. E. Phelps, and A. J. Kidnay. 1976. "Erratum: Liquid-Vapor Equilibria at 250.00 K for Systems Containing Methane, Ethane, and Carbon Dioxide (Journal of Chemical and Engineering Data (1976) 21, (81))." *Journal of Chemical and Engineering Data* 21 (4): 510.

17. de Visser, E., C. Hendriks, M. Barrio, M. J. Mølnvik, G. de Koeijer, S. Liljemark, and Y. Le Gallo. 2008. "Dynamis CO2 Quality Recommendations." *International Journal of Greenhouse Gas Control* 2 (4): 478-484.

18. Dorau, W., I. M. Al-Wakeel, and H. Knapp. 1983. "VLE Data for CO2-CF2Cl2, N2-CO2, N2-CF2Cl2 and N2-CO2-CF2Cl." *Cryogenics* 23 (1): 29-35.

19. Duan, Z. and J. Hu. 2004. "A New Cubic Equation of State and its Applications to the Modeling of Vapor-Liquid Equilibria and Volumetric Properties of Natural Fluids." *Geochimica Et Cosmochimica Acta* 68 (14): 2997-3009.

20. Ely, J. F., W. M. Haynes, and B. C. Bain. 1989. "Isochoric (P, Vm, T) Measurements on CO2 and on (0.982CO2 + 0.018N2) from 250 to 330 K at Pressures to 35 MPa." *The Journal of Chemical Thermodynamics* 21 (8): 879-894.

21. Esper, G. J., D. M. Bailey, J. C. Holste, and K. R. Hall. 1989. "Volumetric Behavior of Near-Equimolar Mixtures for CO2+CH4 and CO2+N2." *Fluid Phase Equilibria* 49 (C): 35-47.

22. Fredenslund, A., J. Mollerup, and O. Persson. 1972. "Gas-Liquid Equilibrium of Oxygen-Carbon Dioxide System." *Journal of Chemical and Engineering Data* 17 (4): 440-443.

23. Fredenslund, A. and G. A. Sather. 1970. "Gas-Liquid Equilibrium of the Oxygen-Carbon Dioxide System." *Journal of Chemical and Engineering Data* 15 (1): 17-22.

24. Ghomian, Y., G. A. Pope, and K. Sepehrnoori. 2008. "Reservoir Simulation of CO2 Sequestration Pilot in Frio Brine Formation, USA Gulf Coast." *Energy* 33 (7): 1055-1067.

25. Gunter, W. D., S. Bachu, D. H. -S Law, V. Marwaha, D. L. Drysdale, D. E. Macdonald, and T. J. McCann. 1996. "Technical and Economic Feasibility of CO2 Disposal in Aquifers within the Alberta Sedimentary Basin, Canada." *Energy Conversion and Management* 37 (6-8): 1135-1142.

26. Gunter, W. D., E. H. Perkins, and I. Hutcheon. 2000. "Aquifer Disposal of Acid Gases: Modelling of Water-Rock Reactions for Trapping of Acid Wastes." *Applied Geochemistry* 15 (8): 1085-1095.

27. Hacura, A., J. -H Yoon, and F. G. Baglin. 1988. "Density Values of Carbon Dioxide and Nitrogen Mixtures from 500 to 2500 Bar at 323 and 348 K." *Journal of Chemical and Engineering Data* 33 (2): 152-154.

28. Hensel Jr., W. E. and F. E. Massoth. 1964. "Phase Equilibria for the Ternary System: CH4-CO2-H2S at Low Temperatures." *Journal of Chemical and Engineering Data* 9 (3): 352-356.

29. Huh, C., S. -G Kang, M. -I Cho, and J. -H Baek. 2011. "Effect of Water and Nitrogen Impurities on CO2 Pipeline Transport for Geological Storage.".

30. Jacquemet, N., Y. Le Gallo, A. Estublier, V. Lachet, I. von Dalwigk, J. Yan, M. Azaroual, and P. Audigane. 2009. "CO2 Streams Containing Associated Components-A Review of the Thermodynamic and Geochemical Properties and Assessment of some Reactive Transport Codes.".

31. Ji, W. -R and D. A. Lempe. 1997. "Density Improvement of the SRK Equation of State." *Fluid Phase Equilibria* 130 (1-2): 49-63.

32. Ji, X. and C. Zhu. 2013. "Predicting Possible Effects of H2S Impurity on CO2 Transportation and Geological Storage." *Environmental Science and Technology* 47 (1): 55-62.

33. Jung, H. B., W. Um, and K. J. Cantrell. 2013. "Effect of Oxygen Co-Injected with Carbon Dioxide on Gothic Shale Caprock-CO2-Brine Interaction during Geologic Carbon Sequestration." *Chemical Geology* 354: 1-14.

34. Kaufmann, K. D. 2010. "Impurity Types, Concentration Influence Hydraulic Design." *Oil and Gas Journal* 108 (14): 60-63.

35. Kestin, J., Y. Kobayashi, and R. T. Wood. 1966. "The Viscosity of Four Binary, Gaseous Mixtures at 20° and 30°C." *Physica* 32 (6): 1065-1089.

36. Kharaka, Y. K., D. R. Cole, S. D. Hovorka, W. D. Gunter, K. G. Knauss, and B. M. Freifeld. 2006. "Gas-Water-Rock Interactions in Frio Formation Following CO2 Injection: Implications for the Storage of Greenhouse Gases in Sedimentary Basins." *Geology* 34 (7): 577-580.

37. Knauss, K. G., J. W. Johnson, and C. I. Steefel. 2005. "Evaluation of the Impact of CO2, Co-Contaminant Gas, Aqueous Fluid and Reservoir Rock Interactions on the Geologic Sequestration of CO2." *Chemical Geology* 217 (3-4 SPEC. ISS.): 339-350.

38. Li, H. and J. Yan. 2009a. "Evaluating Cubic Equations of State for Calculation of Vapor-Liquid Equilibrium of CO2 and CO2-Mixtures for CO2 Capture and Storage Processes." *Applied Energy* 86 (6): 826-836.

39. ———. 2009b. "Impacts of Equations of State (EOS) and Impurities on the Volume Calculation of CO2 Mixtures in the Applications of CO2 Capture and Storage (CCS) Processes." *Applied Energy* 86 (12): 2760-2770.

40. Li, Q., X. Li, N. Wei, and Z. Fang. 2011. "Possibilities and Potentials of Geological Co-Storage CO2 and SO2 in China.".

41. Magee, J. W. and J. F. Ely. 1988. "Isochoric (P, V, T) Measurement on CO2 and (0.98 CO2+0.02 CH4) from 225 to 400 K and Pressures to 35 MPa." *International Journal of Thermophysics* 9 (4): 547-557.

42. Mallu, B. V., G. Natarajan, and D. S. Viswanath. 1987. "Compression Factors and Second Virial Coefficients of CO2, CO, and {xCO+ (1 - X)CO2}." *The Journal of Chemical Thermodynamics* 19 (5): 549-554.

43. McElroy, P. J., R. Battino, and M. K. Dowd. 1989. "Compression-Factor Measurements on Methane, Carbon Dioxide, and (Methane + Carbon Dioxide) using a Weighing Method." *The Journal of Chemical Thermodynamics* 21 (12): 1287-1300.

44. Mito, S., Z. Xue, and T. Sato. 2013. "Effect of Formation Water Composition on Predicting CO2 Behavior: A Case Study at the Nagaoka Post-Injection Monitoring Site." *Applied Geochemistry* 30: 33-40.

45. Nimtz, M., M. Klatt, B. Wiese, M. Kühn, and H. Joachim Krautz. 2010. "Modelling of the CO2 Process- and Transport Chain in CCS Systems-Examination of Transport and Storage Processes." *Chemie Der Erde - Geochemistry* 70 (SUPPL. 3): 185-192.

46. Patel, N. C. and A. S. Teja. 1982. "A New Cubic Equation of State for Fluids and Fluid Mixtures." *Chemical Engineering Science* 37 (3): 463-473.

47. Péneloux, A., E. Rauzy, and R. Fréze. 1982. "A Consistent Correction for Redlich-Kwong-Soave Volumes." *Fluid Phase Equilibria* 8 (1): 7-23.

48. Peng, D. -Y and D. B. Robinson. 1976. "A New Two-Constant Equation of State." *Industrial and Engineering Chemistry Fundamentals* 15 (1): 59-64.

49. Pipitone, G. and O. Bolland. 2009. "Power Generation with CO2 Capture: Technology for CO2 Purification." *International Journal of Greenhouse Gas Control* 3 (5): 528-534.

50. Pruess, K. and J. García. 2002. "Multiphase Flow Dynamics during CO2 Disposal into Saline Aquifers." *Environmental Geology* 42 (2-3): 282-295.

51. Redlich, O. and J. N. S. Kwong. 1949. "On the Thermodynamics of Solutions. V: An Equation of State. Fugacities of Gaseous Solutions." *Chemical Reviews* 44 (1): 233-244.

52. Sanpasertparnich, T., R. Idem, I. Bolea, D. deMontigny, and P. Tontiwachwuthikul. 2010. "Integration of Post-Combustion Capture and Storage into a Pulverized Coal-Fired Power Plant." *International Journal of Greenhouse Gas Control* 4 (3): 499-510.

53. Seitz, J. C. and J. G. Blencoe. 1996. "Volumetric Properties for {(1 - X)CO2 + xCH4}, {(1 - X)CO2 + xN2}, and {(1 - X)CH4 + xN2} at the Pressures (19.94, 29.94, 39.94, 59.93, 79.93, and 99.93) MPa and the Temperature 673.15 K." *Journal of Chemical Thermodynamics* 28 (11): 1207-1213.

54. Soave, G. 1972. "Equilibrium Constants from a Modified Redlich-Kwong Equation of State." *Chemical Engineering Science* 27 (6): 1197-1203.

55. Somait, F. A. and A. J. Kidnay. 1978. "Liquid-Vapor Equilibria at 270.00 K for Systems Containing Nitrogen, Methane, and Carbon Dioxide." *Journal of Chemical and Engineering Data* 23 (4): 301-305.

56. Thiery, R., J. Vidal, and J. Dubessy. 1994. "Phase Equilibria Modelling Applied to Fluid Inclusions: Liquid-Vapour Equilibria and Calculation of the Molar Volume in the CO2CH4N2 System." *Geochimica Et Cosmochimica Acta* 58 (3): 1073-1082.

57. Trappehl, G. and H. Knapp. 1989. "Vapour-Liquid Equilibria in the Ternary Mixture N2-CH4-CO2 and the Quaternary Mixture N2-CH4-C2H6-C3H8." *Cryogenics* 29 (1): 42-50.

58. Von Solms, N., C. O. Anderson, H. W. Blanch, and J. M. Prausnitz. 2002. "Molecular Thermodynamics for Fluid-Phase Equilibria in Aqueous Two-Protein Systems." *AICHE Journal* 48 (6): 1292-1300.

59. Wang, J., D. Ryan, E. J. Anthony, A. Wigston, L. Basava-Reddi, and N. Wildgust. 2012. "The Effect of Impurities in Oxyfuel Flue Gas on CO2 Storage Capacity." *International Journal of Greenhouse Gas Control* 11: 158-162.

60. Wang, J., D. Ryan, E. J. Anthony, N. Wildgust, and T. Aiken. 2011. "Effects of Impurities on CO2 Transport, Injection and Storage.".

61. Wang, S. and P. R. Jaffe. 2004. "Dissolution of a Mineral Phase in Potable Aquifers due to CO2 Releases from Deep Formations; Effect of Dissolution Kinetics." *Energy Conversion and Management* 45 (18-19): 2833-2848.

62. Wigand, M., J. W. Carey, H. Schütt, E. Spangenberg, and J. Erzinger. 2008. "Geochemical Effects of CO2 Sequestration in Sandstones Under Simulated in Situ Conditions of Deep Saline Aquifers." *Applied Geochemistry* 23 (9): 2735-2745.

63. Wilke, F. D. H., M. Vásquez, T. Wiersberg, R. Naumann, and J. Erzinger. 2012. "On the Interaction of Pure and Impure Supercritical CO 2 with Rock Forming Minerals in Saline Aquifers: An Experimental Geochemical Approach." *Applied Geochemistry* 27 (8): 1615-1622.

64. Wilkin, R. T. and D. C. Digiulio. 2010. "Geochemical Impacts to Groundwater from Geologic Carbon Sequestration: Controls on pH and Inorganic Carbon Concentrations from Reaction Path and Kinetic Modeling." *Environmental Science and Technology* 44 (12): 4821-4827.

65. Xu, N., J. Dong, Y. Wang, and J. Shi. 1992. "High Pressure Vapor Liquid Equilibria at 293 K for Systems Containing Nitrogen, Methane and Carbon Dioxide." *Fluid Phase Equilibria* 81 (C): 175-186.

66. Xu, T., J. A. Apps, K. Pruess, and H. Yamamoto. 2007. "Numerical Modeling of Injection and Mineral Trapping of CO2 with H2S and SO2 in a Sandstone Formation." *Chemical Geology* 242 (3-4): 319-346.

67. Yorizane, M., S. Yoshimura, H. Masuoka, Y. Miyano, and Y. Kakimoto. 1985. "New Procedure for Vapor-Liquid Equilibria. Nitrogen + Carbon Dioxide, Methane + Freon 22, and Methane + Freon 12." *Journal of Chemical and Engineering Data* 30 (2): 174-176.

68. Yu, J. -M, B. C. -Y Lu, and Y. Iwai. 1987. "Simultaneous Calculations of VLE and Saturated Liquid and Vapor Volumes by Means of a 3P1T Cubic EOS." *Fluid Phase Equilibria* 37 (C): 207-222.

69. Zhu, J., T. M. Parris, J. Richard Bowersox, and D. C. Harris. 2013. "Modeling CO2-Brine-Rock Interactions in the Knox Group: Implications of a Deep Carbon Storage Field Test in Western Kentucky." *Applied Geochemistry* 37: 29-42.

70. Ziabakhsh-Ganji, Z. and H. Kooi. 2012. "An Equation of State for Thermodynamic Equilibrium of Gas Mixtures and Brines to Allow Simulation of the Effects of Impurities in Subsurface CO2 Storage." *International Journal of Greenhouse Gas Control* 11 (SUPPL): 21-34.

71. Zirrahi, M., R. Azin, H. Hassanzadeh, and M. Moshfeghian. 2010. "Prediction of Water Content of Sour and Acid Gases." *Fluid Phase Equilibria* 299 (2): 171-179.

Chapter 3

Effects of Impurities on the Physical Properties of CO_2 in Geological Storage Sites

Abstract

The physical effects of impurities on CO_2 transportation and geological storage were studied. Two different gas mixtures, Gas Mixture 1 – N_2 6.03%, O_2 5%, Ar 4.5%, CO_2 balance and Gas Mixture 2 – Ar 14.25%, CO_2 balance, were selected to represent the CO_2 streams with high-concentration impurities from oxyfuel combustion.

The density changes were analyzed through calculations and experiments, and the results showed that 15% impurities caused density to decrease by 61% at 35 ℃. Based on calculated and experimental results, the CO_2 storage capacity and buoyancy were calculated and compared with those of pure CO_2. With the inclusion of non-condensable impurities, the highest reduction of CO_2 storage capacity was 65% and the normalized buoyancy of CO_2 fluids increased by 2.3 times. However, all these effects decreased with increasing temperature. To estimate suitable operation conditions of CCS, the phase behaviours were simulated and the results showed that 15% impurities caused phase behaviours to change vastly. A minimum pressure of 10 MPa was needed to avoid two phase flow at all temperature. Conversely, if the transportation is in the liquid phase then the lower critical temperature would require a lower pipeline temperature. Finally, a hypothesis that the total air-derived impurities in oxyfuel combustion CO_2 streams could be represented by Ar in calculations and experiments for evaluating phase and volumetric behaviours was studied. This replacement by Ar showed a good performance in the evaluations of density and storage capacity changes. However, this hypothesis was not well satisfied in the calculation of buoyancy and the simulation of phase behaviour.

Keywords: CO_2 transportation and storage, density, phase behaviour, storage capacity.

3.1 Introduction

Carbon capture and storage has been identified as one of the major technologies for reducing atmospheric CO_2 emissions. As the various chemical compositions of different fuels, the CO_2 emission originated from power plants and other industrial facilities contains various impurities, such as N_2, O_2, Ar, NO_x, SO_x and H_2S, in various concentrations (Abbas et al., 2013; Sanpasertparnich et al., 2010; Kaufmann, 2010; Cosham et al., 2010; Pipitone and Bolland, 2009; de Visser et al., 2008). Generally, the purification of impure CO_2 streams would drastically increase the cost of CCS (Ji and Zhu, 2013). In order to reduce the cost of CO_2 capture and storage, co-injection and co-storage of the impurities with CO_2 have been considered in recent studies. However, the possible impurities, which are shown in Table 2.1, would influence the physical properties of CO_2 in the transportation and storage performance. For instance, non-condensable impurities would reduce the density and the volume fraction of CO_2. The storage capacity therefore decreases due to the presence of impurities in the CO_2 stream. Also, the inclusion of non-condensable gases would increase the bubble-point pressure and decrease the critical temperature. As a result, to avoid two-phase flow, lower temperature and additional overpressure are needed in pipeline transport. Therefore, an appropriate CCS system, which is dependent on thermodynamic properties, operating facilities and materials, should be designed in accordance with these physical and chemical effects.

The concentrations of impurities in the CO_2 stream vary with the different CO_2 capture methods. According to the IEAGHG (International Energy Agency's Greenhouse Gas R&D Programme), there are three scenarios for CO_2 purity from oxyfuel combustion stream:

Scenario 1 – high impurity (CO_2 purity between 85-90%)

Scenario 2 – medium purity (CO_2 purity between 95-97%)

Scenario 3 – low impurity (CO_2 purity greater than 99%)

where N_2, O_2 and Ar comprise the major part of the impurities. As discussed above, this project focused on the possibilities of co-injection and co-storage CO_2 with high concentration of impurities. Two types of CO_2 gas mixture were used for the study of CO_2 physical properties:

Gas mixture 1 – N_2 6.03%, O_2 5%, Ar 4.5%, CO_2 balance;

Gas mixture 2 – Ar 14.25%, CO_2 balance.

According to the literature survey of thermodynamic data before this study, whose results have been shown in Table 2.6, the experiments for CO_2 streams with 15% impurities in the pressure and temperature ranges for CO_2 storage have not been conducted. This section aims to elucidate the effects of 15% impurities on the physical properties of CO_2 streams in typical CO_2-storage pressure and temperature ranges. Density is an important parameter in the evaluation of CO_2 transportation and storage capacity. For instance, it reflects the amount of fluid that could be stored at a fixed volume. Thus, density is the main topic in this chapter for theoretical and experimental evaluations. Based on the experimental and simulation results, the change of storage capacity and buoyancy were quantified further.

There are two hypotheses with regard to the phase and volumetric behaviours of the impure CO_2 discussed above. One is based on the simulation results by Wang et al. (2011) that non-condensable impurities would affect the density of CO_2 stream and storage capacity by much more than its percentage in the mixture. The other scenario is that the behaviour of CO_2 containing15% multi-impurities (N_2, O_2 and Ar) is similar to that containing 15% Ar.

In this study, the effects of high concentration impurities on physical properties of CO_2 stream will be evaluated, and the two hypotheses above will be verified by simulation and experimental results.

3.2 Methodologies

3.2.1 Simulation by REFPROP

Software REFPROP was used to predict the physical properties of CO_2 gas mixture. This program, which was developed by the National Institute of Standards and Technology (NIST), calculates the thermodynamic and transport properties of industrially important fluids and their mixtures. The modified Benedict-Webb-Rubin equation of state was used to implement the thermodynamic calculation of pure fluids. Mixture calculations employ a model that applies mixing rules to the Helmholtz energy of the mixture components; it uses a departure function to account for the departure from ideal mixing.

3.2.2 Experimental method

A density measurement system comprising a measuring cell unit DMA HPM (Density Measuring Cell for High pressures and High Temperature) and an evaluation unit mPDS 5

manufactured by Anton Paar© was used in the experiments and analysis. DMA HPM is designed to measure the density of liquids and gases in a temperature range of -10 °C to +200 °C (+14 °F to +392 °F) and at a pressure range of 0 to 1400 bar (0 to 20300 psi). A sketch of the experimental setup is shown in Figure 3.1. The DMA HPM consists of the measuring cell and an interface module. The interface module generates oscillation, and measures the period of the oscillation which will be converted to the density value. To display the measuring parameters, the DMA HPM must be connected to the mPDS 5 evaluation unit. Temperature and pressure are controlled externally. In the present study the temperature of the measuring system was maintained through a circulating water bath connected to DMA HPM by hoses. The CO_2 mixtures were injected into the measuring cell through a high-pressure syringe pump where the pressure could be accurately controlled.

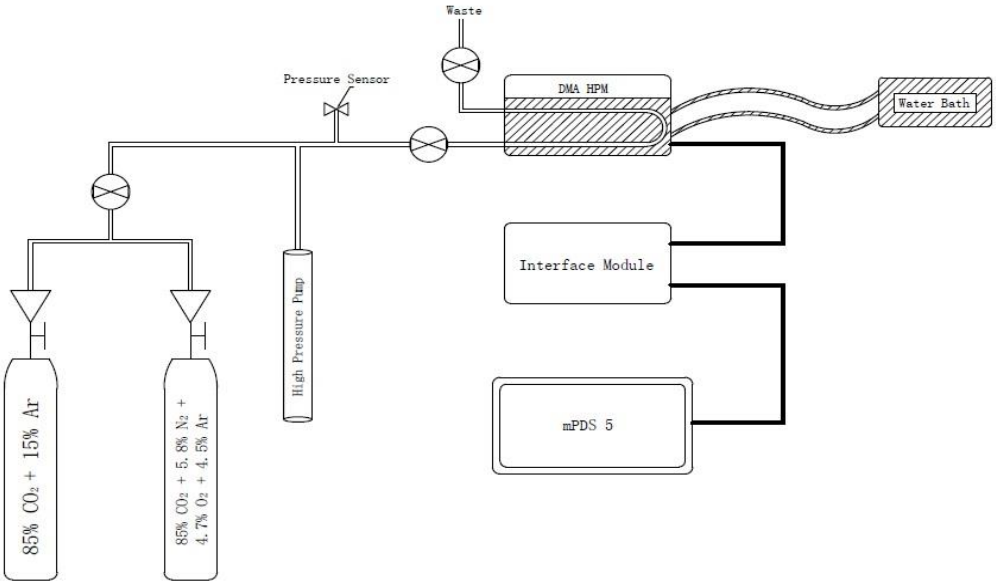

Figure 3.1 Sketch of experimental setup

Before the measurement, DMA HPM has to be adjusted using two different samples of known density at required temperature and pressure. With the data collected during the adjustment, the evaluation unit could determine a mathematical relation between different densities and the corresponding oscillation periods, and express this relation in the form of constants or polynomial coefficients. The measuring system can then calculate the density

values from oscillation periods using the mathematical relation. Eq. 13 (Manual Book of Anton Paar©) is used to calculate the density from the sample's period of oscillation measured by DMA HPM.

$$Density = AA + AB * dt + AC * dd + AD * dt^2 + AE * dd^2 + (AF + AG * dt + AH * dd + AI * dt^2 + AJ * dd^2) * dp^2 + AK * dp^4 \quad (13)$$

where *dt, dd, dp* denote the temperature, pressure and oscillation period, respectively; AA…AK…are the polynomial coefficients in the density calculation.

In this study, Ar and pure CO_2 were used for the adjustment before the measurements. The coefficients were calculated by the software provided by company Anton Paar©. The average deviation between the results measured by DHM HPM and the results calculated by REFPROP was 0.02%. To verify the accuracy of this measurement system further, the density of pure CO_2 at 75 ℃ and 120 bar was measured and compared with the calculated density. The deviation was 0.09%, which suggests that the system could measure the densities with good accuracy.

3.3 Results and discussions

Effects of Impurities on Density

The density of Gas Mixture 1 was measured in the pressure range from 7 MPa to 25 MPa and at three different temperatures, 35, 55 and 75 ℃. As shown in Figure 3.2, the density of mixture 1 increased with increasing pressure and the increase was most significant in the range 10-15 MPa at 35 ℃. This is similar to the case of pure CO_2, where a small increase in pressure results in a large increase in density. However, it is clear that the non-condensable impurities decreased the pressure dependence of the density. When temperature increased, the pressure dependence of the density decreased further. At 75 ℃, the pressure dependence was almost linear. The average deviation between calculated results and experimental data in this study was 1.39%.

To evaluate the effects of impurities on the density of the CO_2 stream further, the change of density of CO_2 stream with pressure was plotted in Figure 3.3. Here, the normalized

density was defined as a quotient in percentage, (density of CO_2 gas mixture) / (density of pure CO_2) × 100. As shown in Figure 3.3, there was a minimum value of the data at each temperature. The lowest values of the normalized density of the CO_2 steam were 39%, 62% and 73% for 35, 55 and 75 ℃, respectively. Therefore, it is clear that the effects of ~15% impurities on the density of CO_2 stream would be much greater than 15%. For instance, the density could decrease by 61% of that of pure CO_2 with 15% impurities involved, under the condition 35 ℃ and 9 MPa. Accordingly, such operation conditions should be avoided, in order to avoid excessive reduction of CO_2 storage capacity. It is also clear that with temperature increasing, the reduction of the storage capacity due to the air-derived impurities decreases.

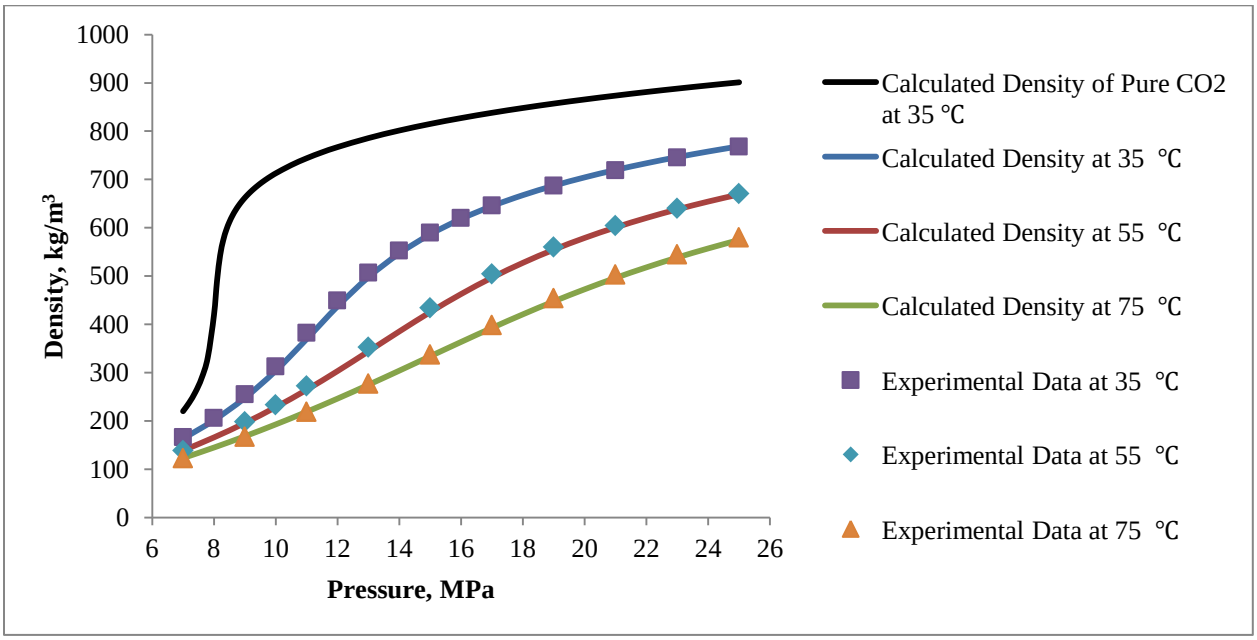

Figure 3.2 The comparisons of calculated density with measured density of Gas Mixture 1 (N_2 6.03%, O_2 5%, Ar 4.5%, CO_2 balance).

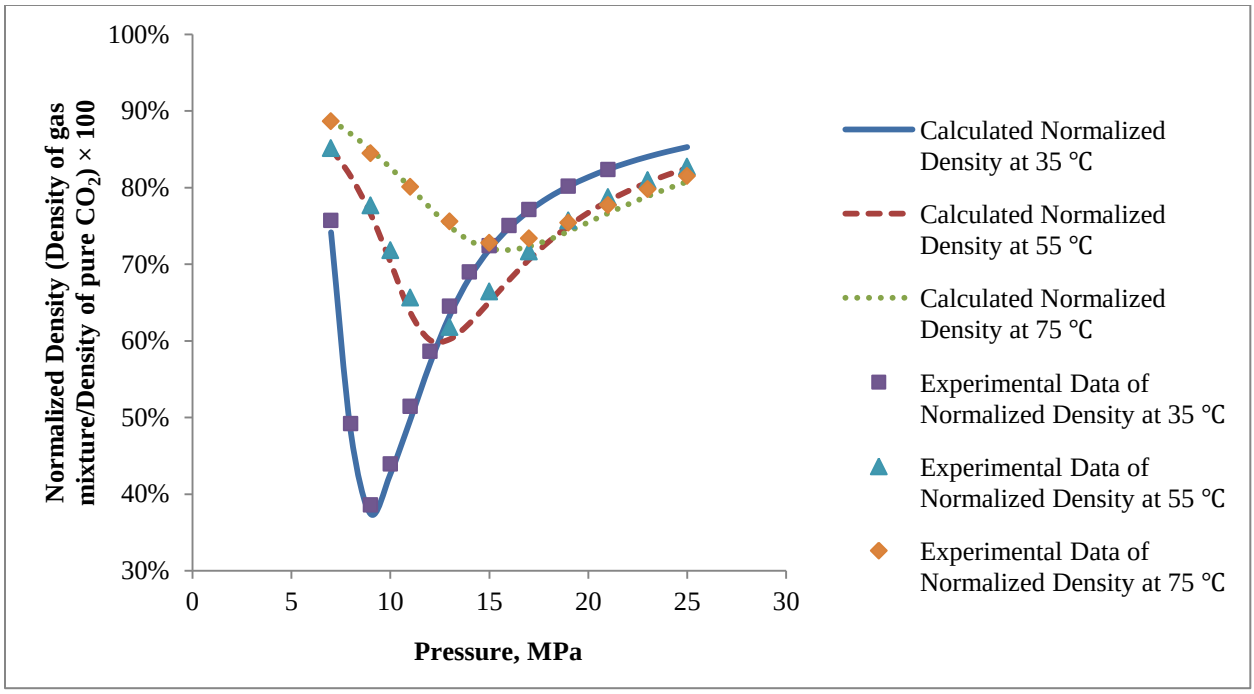

Figure 3.3 The comparisons of calculated normalized density with measured normalized density of Gas Mixture 1 (N_2 6.03%, O_2 5%, Ar 4.5%, CO_2 balance).

To verify the second hypothesis, the behaviour of CO_2 containing 15% multi-impurities (N_2, O_2 and Ar) is similar to that containing 15% Ar, the density of CO_2 mixture 2 was measured at 35 and 75 ℃ in pressure range 7-25 MPa. The trends of density change with pressure, which can be seen in Figures 3.4 and 3.5, indicate that the behaviour of CO_2 mixture 2 is similar to that of CO_2 mixture 1. As shown in Figure 3.4, the density increased substantially with increasing pressure at 35 ℃ in pressure range 10-15 MPa. The maximum reduction (~60%) of CO_2 density at 35 ℃ can be found at 9 MPa on Figure 3.5, which is under the same condition discussed for CO_2 mixture 1. At higher temperature (75 ℃), the pressue dependence is weaker, showing a similar trend to that of CO_2 mixture 1. In addition, the calculated values show a better agreement with the experimental data (with an average deviation 1.18%), suggesting that the calculated values are closer to measured results with the temperature moving away from the critical temperature.

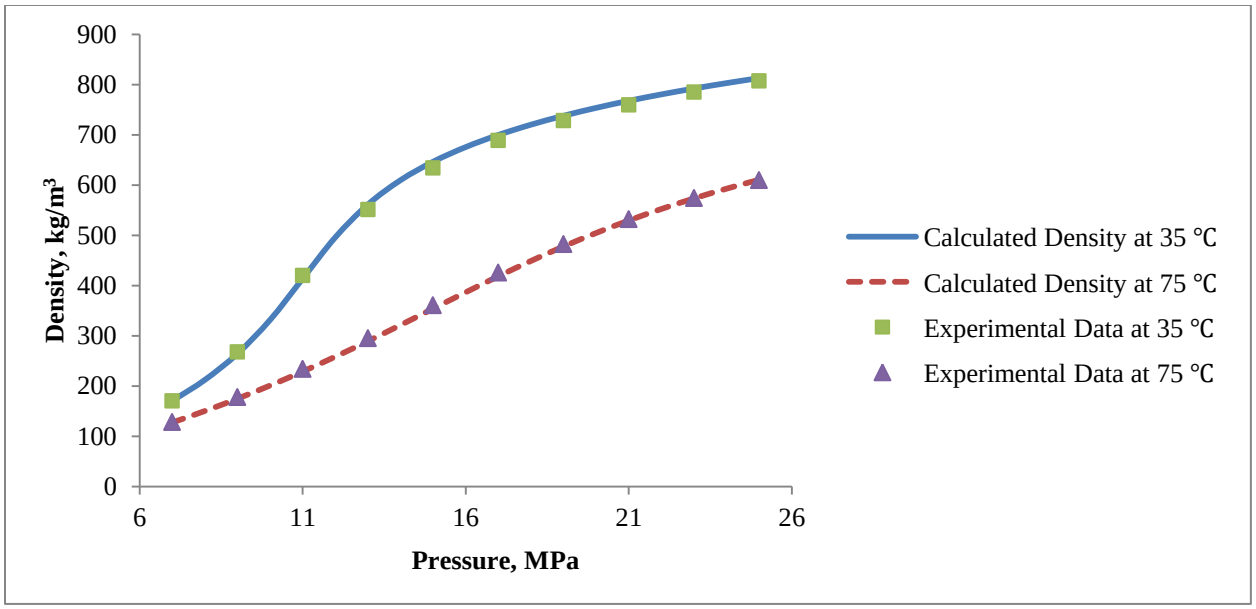

Figure 3.4 The comparisons of calculated density with measured density of Gas Mixture 2 (Ar 14.25%, CO_2 balance).

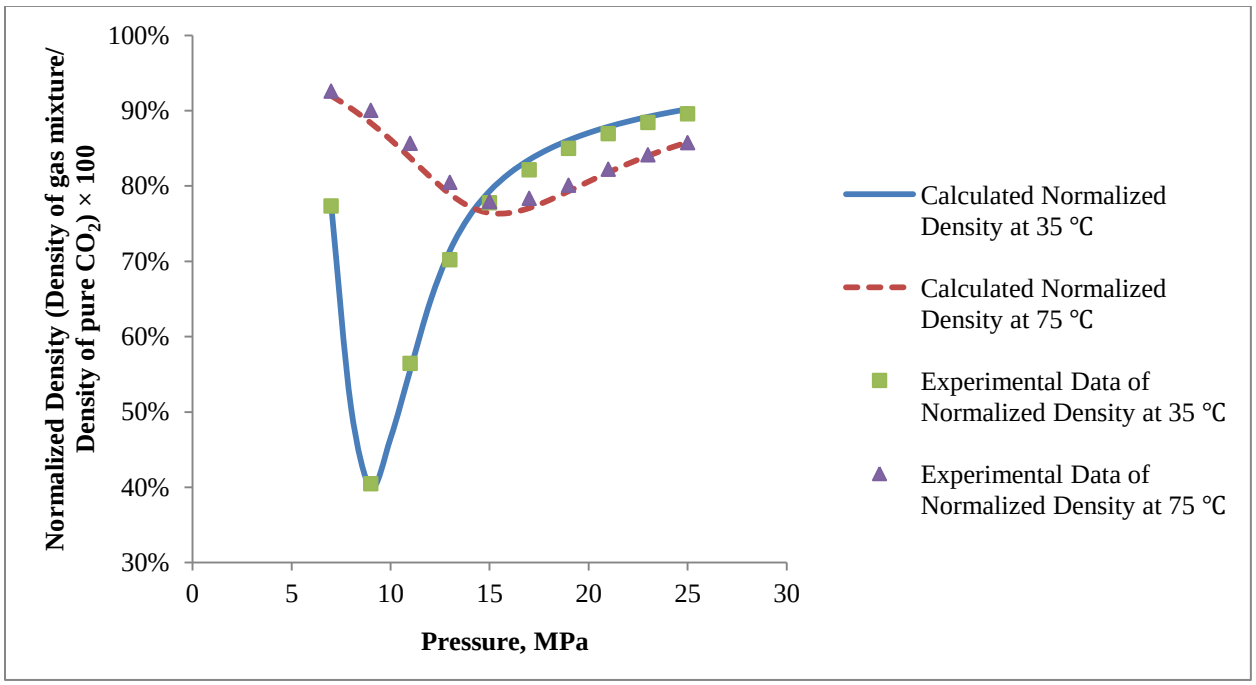

Figure 3.5 The comparisons of calculated normalized density with measured normalized density of Gas Mixture 2 (Ar 14.25%, CO_2 balance).

To further evaluate the performance of representing air-derived impurities using Ar, the measured and calculated density values of CO_2 mixture 1 were compared with those of CO_2 mixture 2 in Figure 3.6, and the deviation in percentage of CO_2 mixture 1 (Density difference of Gas Mixture 1 and 2/ Density of Gas Mixture 1) was plotted against pressure in Figure 3.7. As shown in Figure 3.6, the measured values and calculated values show a similar trend, but the density of CO_2 mixture 2 was consistently slightly higher than that of CO_2 mixture 1. The degree of the deviation can be seen in Figure 3.7, which indicates that the average deviation between the two mixtures is around 5%. The difference could be partly attributed to the deviations in the concentrations. The total concentration of impurities in CO_2 mixture 1 was 15.53% and in CO_2 mixture 2 was 14.25% due to the technical limitation on the gas preparation, meaning that the density of CO_2 mixture 2 should be higher than that of CO_2 mixture 1 because of the lower concentration of the impurities. Therefore, another calculation was also performed to eliminate the effect of different impurity concentrations and the results are shown in Figure 3.8. The calculated values were for CO_2 Gas Mixture 1 and a CO_2/Ar mixture with the same impurity concentration as that of CO_2 mixture 1. As shown in Figure 3.8, the deviation was minor at low pressures and increased with increasing pressure. The peak of deviation, around 8%, can be seen at 35 ℃ from 10-16 MPa. When the temperature increased, the peak became smaller and the pressure dependence became weaker. The average deviation was 5%, which was the same as the average deviation discussed earlier. The results suggest that Ar can be used to represent the air-derived impurities in the study of density change with acceptable accuracy.

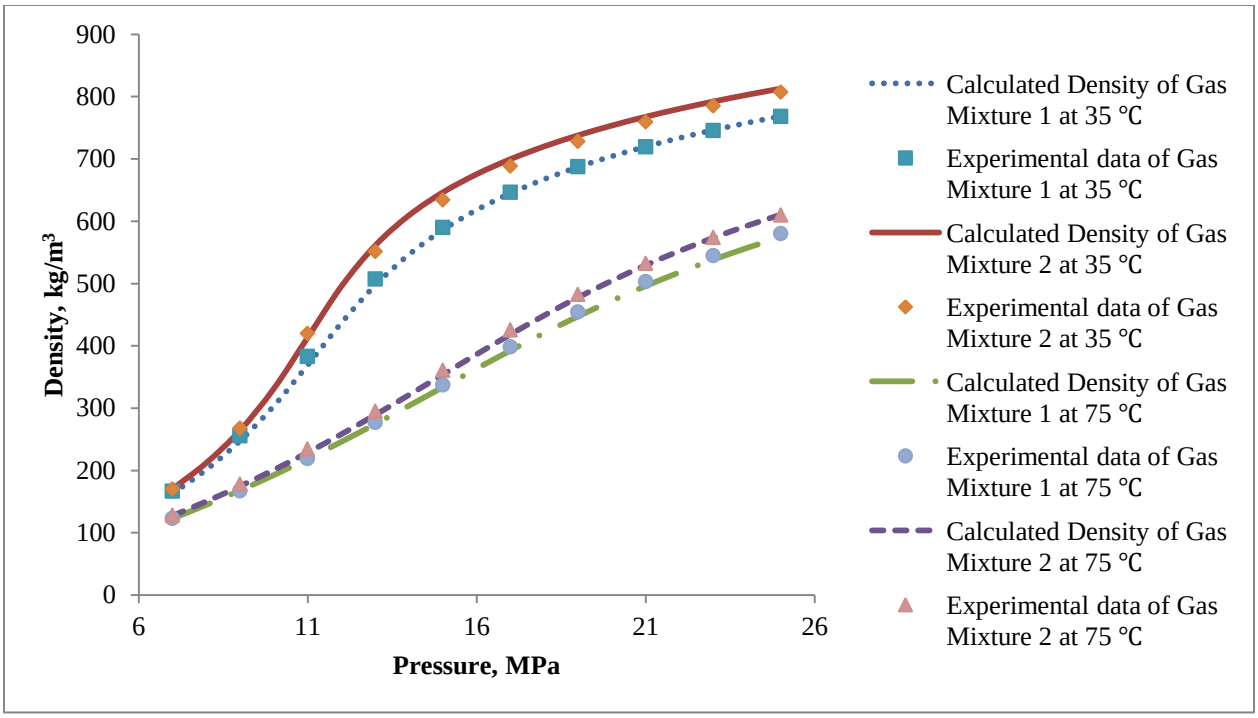

Figure 3.6 The comparison of the density of Gas Mixture 1 and Gas Mixture 2.

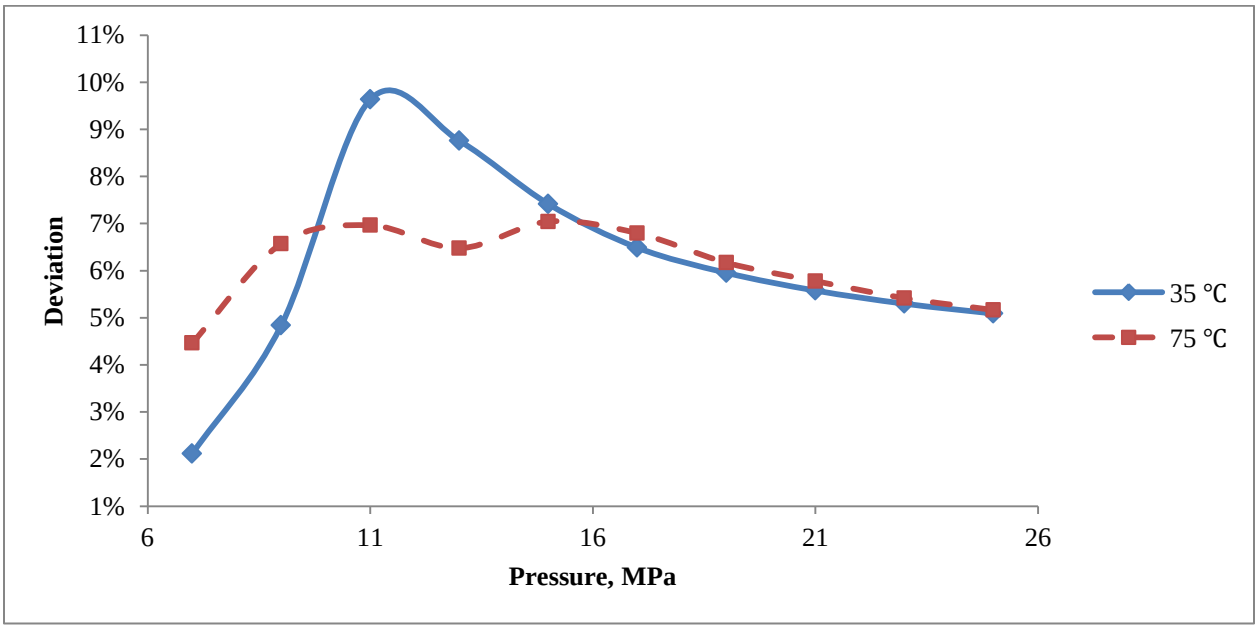

Figure 3.7 The deviation of representing 15% multi-light impurities by Ar.

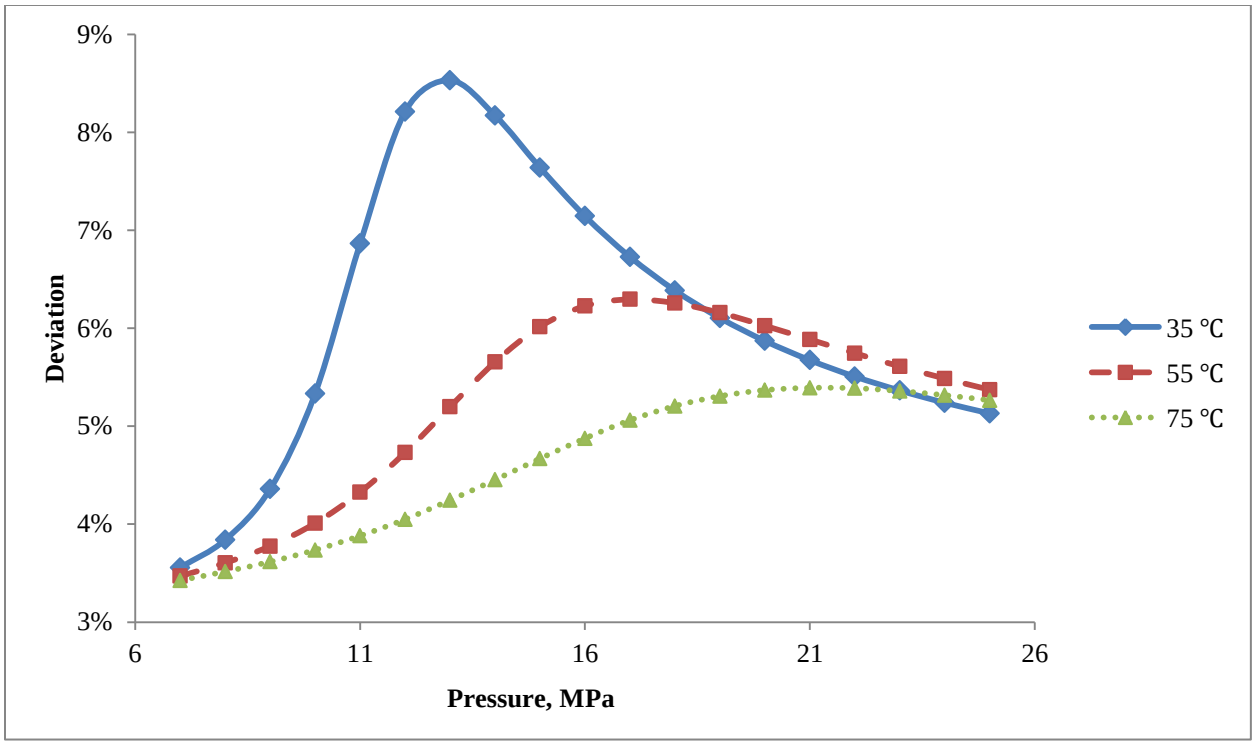

Figure 3.8 Calculated deviation between the density of Gas Mixture 1 and the gas with a same concentration of impurities represented by Ar.

Effects on CO_2 Storage Capacity

Due to the inclusion of non-condensable impurities involved in CO_2 streams, the CO_2 storage capacity would decrease because of lower volume fraction of CO_2 and lower fluid density. In order to quantify the change of storage capacity, a normalized storage capacity equation (Wang et al., 2012), which is shown in Eq. 14, is used here to evaluate the capacity change.

$$\frac{M}{M_0} = \frac{\bar{\rho}}{\rho_0(1 + \sum_i m_i/m_{co_2})} \qquad (14)$$

where M and M_0 denote the mass of CO_2 in the mixture and in the pure stream, which occupy the same volume, $\bar{\rho}$ and ρ_0 are the density of the mixture and the pure stream, and m_i/m_{co_2} is the ratio of the mass of impurity i to the mass of CO_2 in the mixture. The ratio M/M_0 on the left-hand side of the equation, which can also be viewed as the ratio of the mass of CO_2 per unit volume in the mixture to that in the pure state, represents a normalized

storage capacity. This equation provides a better accuracy in the quantification of storage capacity than using the "normalized density", because the "normalized density" does not exclude the mass of the impurities mixed with CO_2 whereas Eq. (14) gives the change of storage capacity for CO_2 only. In the case of pure CO_2 the normalized CO_2 capacity becomes unity.

The results were plotted in Figure 3.9 with different pressures. As can be seen, at 35 ℃, the storage capacity was reduced to as low as 35% of the pure CO_2 case at 9 MPa. When temperature increased, the reductions in the storage capacity became smaller. The storage capacity for CO_2 mixture 1 reduced 54% under 55 ℃ and 13 MPa, and 64% under 75 ℃ and 15 MPa, respectively. These results indicate that effect of 15% impurities in the CO_2 stream on the geological storage capacity was much greater than 15%.

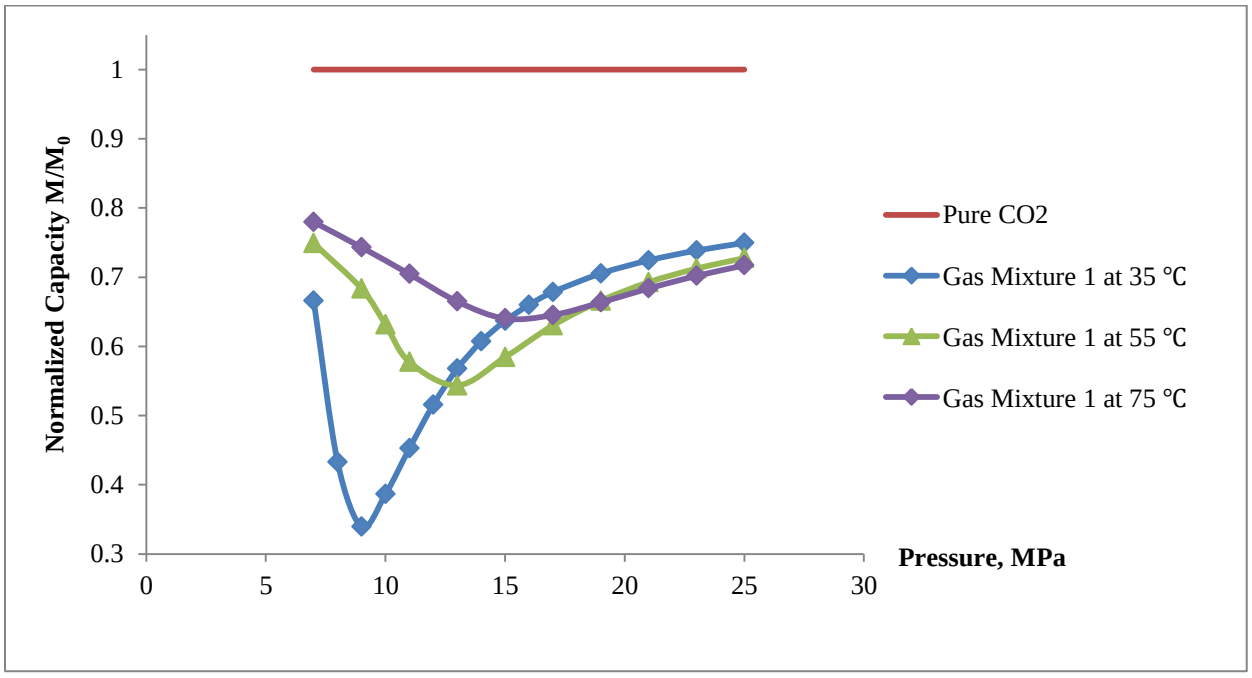

Figure 3.9 Normalized CO_2 storage capacity for Gas Mixture 1.

Effects on Buoyancy

The ideal situation of CCS is CO_2 stored stably underground. However, CO_2 would migrate upward due the difference between the density of CO_2 stream and aquifer brine. The speed of the migration could affect the dissolution of CO_2 in aquifer brine, and trapping of

CO_2 in rock pores, and hence affect the efficiency for CO_2 trapping. Therefore, the buoyancy of CO_2 needs to be considered in the evaluation of CO_2 storage.

The buoyancy would increase due to the decreased density when light impurities are involved. Here we consider a mass in a unit volume where the buoyancy force can be expressed in terms of density:

$$F = \left(\rho_{H_2O} - \rho_m\right)g \qquad (15)$$

where F is the buoyancy in a unit volume, ρ_{H_2O} and ρ_m are the density of the water and the CO_2 fluid, and g is the gravitational acceleration. When the changes in relative permeability and capillary pressure are neglected, the effect of impurities on this force with reference to pure CO_2 may be normalized, like storage capacity, as:

$$\frac{F}{F_0} = \frac{\rho_{H_2O} - \rho_m}{\rho_{H_2O} - \rho_{CO_2}} \qquad (16)$$

where F and F_0 are the buoyancy force for the CO_2 mixture and pure CO_2, respectively. As shown in Eq. 16, the buoyancy would be affected by the density of saline water in the storage site and the normalized density due to the impurities involved. As mentioned above, rock samples from two wells of Alberta were analyzed in this project. The two wells are referred to as 12W4 and 7W4, respectively. The density of saline water from 12W4 was 1200 kg/m^3 and that from 7W4 was 1020 kg/m^3, which were both assumed as constants. Thus, Figure 3.10 and 3.11 show the normalized buoyancy of CO_2 mixture 1 for 12W4 and 7W4, respectively, which was calculated in accordance with the measured density values. The normalized buoyancy of CO_2 fluids increased with the increasing of pressure in general. However, the curves showed different trends at different temperatures. The peaks, which were 1.8 towards 12W4 and 2.3 towards 7W4, can be seen at 35 ℃ around a pressure of 10 MPa in both Figure 3.10 and 3.11. Above that pressure, the normalized buoyancy decreases with increasing pressure. The pressure dependences of buoyancy at 55 ℃ and 75 ℃ were weaker compared with those at 35 ℃. The normalized buoyancy increased drastically in the pressure range from 7-13 MPa and turned linear after this range.

Increased buoyancy would result in increased escape velocity of injected CO_2 and less time for the CO_2 to react with the saline brine. This will reduce the trapping efficiency for CO_2 because of decreased dissolution of CO_2 in the saline brine and decreased trapping of CO_2 in rock pores. The results shown in Figures 3.10 and 3.11 suggest that the effect of the air-derived impurities on the buoyancy decreases with increasing temperature. Accordingly, injecting CO_2 deeper in the subsurface would reduce the negative impurity effect on CO_2 trapping efficiency, because at greater depth the temperature is higher, and the greater depth enables longer time for CO_2 to react with saline during its upward migration.

The effects of saline density on CO_2 buoyancy can be identified by the comparison between Figure 3.10 and 3.11. The buoyancy change is more pronounced in 7W4 than in 12W4. This could be explained by the different densities of 12W4 and 7W4. Eq. 17 shows the difference of normalized buoyancy towards 12W4 and 7W4,

$$\left(\frac{F_{12W4}}{F_0}\right) - \left(\frac{F_{7W4}}{F_0}\right) = \frac{\rho_{12W4} - \rho_M}{\rho_{12W4} - \rho_{CO_2}} - \frac{\rho_{7W4} - \rho_M}{\rho_{7W4} - \rho_{CO_2}} = \frac{(\rho_{12W4} - \rho_{7W4})(\rho_m - \rho_{CO_2})}{(\rho_{12W4} - \rho_{CO_2})(\rho_{7W4} - \rho_{CO_2})} \quad (17)$$

where $\left(\frac{F_{12W4}}{F_0}\right)$ and $\left(\frac{F_{7W4}}{F_0}\right)$ denote the normalized buoyancy of the fluids in storage sites 12W4 and 7W4, respectively. In the result of Eq.17, the conditions $\rho_{12W4} - \rho_{7W4} > 0$, $\rho_m - \rho_{CO_2} < 0$, $\rho_{12W4} - \rho_{CO_2} > 0$ and $\rho_{7W4} - \rho_{CO_2} > 0$ suggest that the difference of normalized buoyancy between 12W4 and 7W4 is negative, which is consistent with the results shown in Figure 3.10 and 3.11.

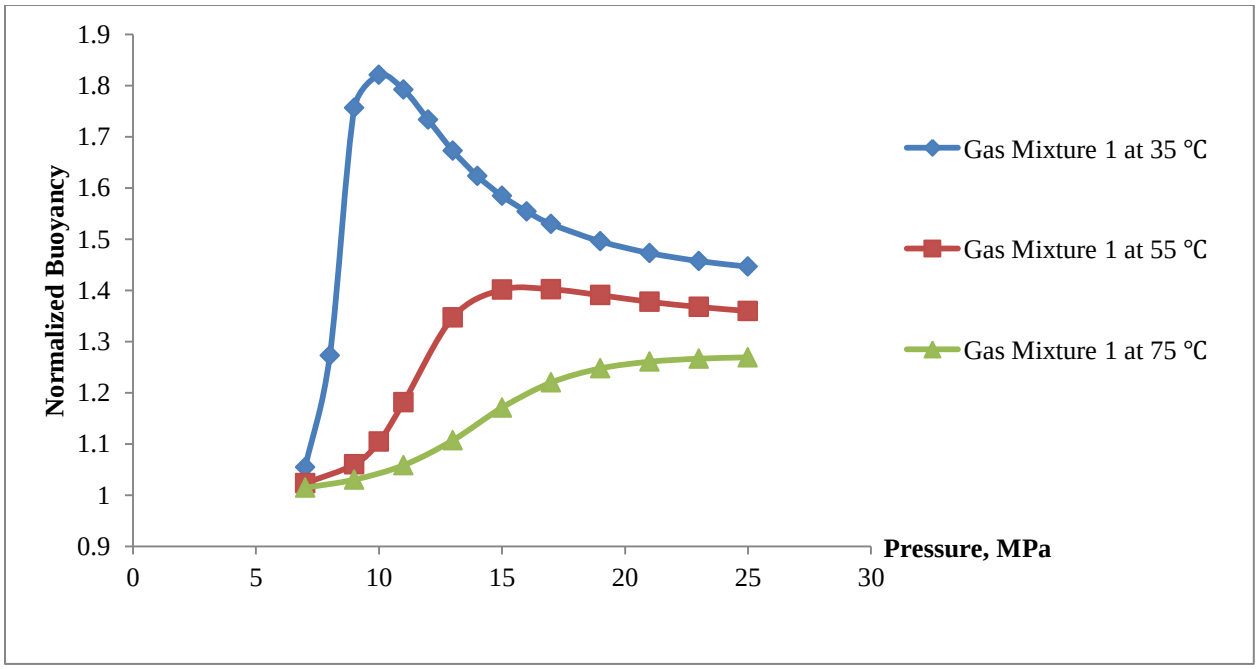

Figure 3.10 Normalized buoyancy towards 12W4.

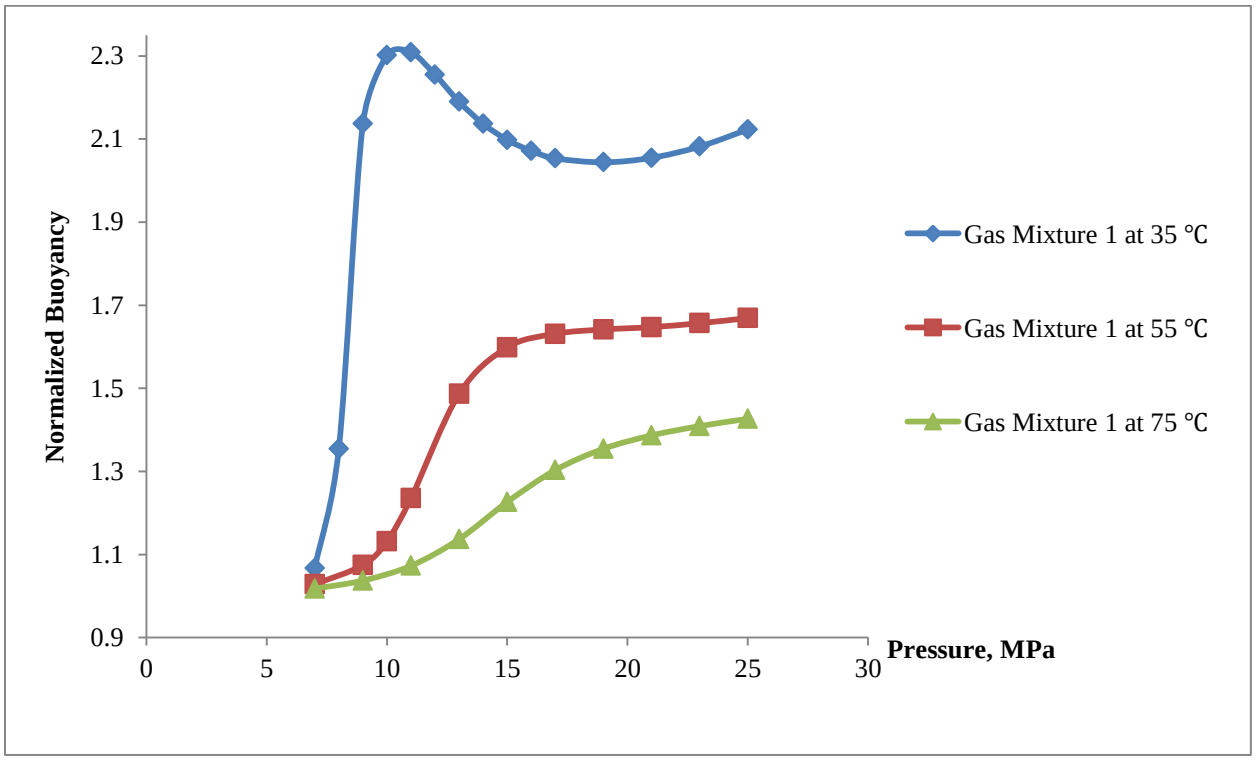

Figure 3.11 Normalized buoyancy towards 7W4.

Effects on Phase Behaviour

To estimate the operation conditions, the phase behaviours of Gas Mixture 1 and Gas Mixture 2 were simulated by UNISIM©. As shown in Figure 3.12, the phase behaviours changed significantly. The two-phase regions can be formed in both Gas Mixture 1 and Gas Mixture 2. Additionally, the bubble point pressure increased and the critical temperature decreased with the inclusion of non-condensable impurities. Therefore, a minimum pressure 10 MPa would be needed to avoid two phase flow. On the other hand, if the transportation is in the liquid phase then the lower critical temperature would require lower pipeline temperature, which may be attained by insulation or cooling. In the calculation of phase behaviour, the accuracy of representing the light impurities by Ar was unsatisfactory. In particular, the difference of bubble point pressure is extremely large (1.2 MPa).

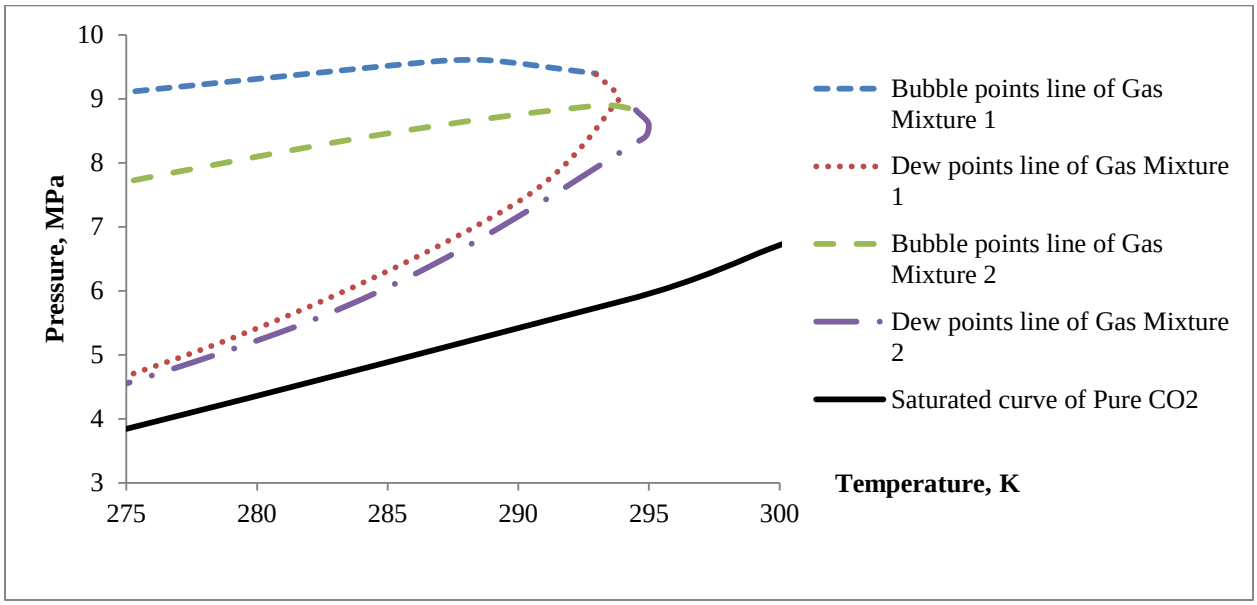

Figure 3.12 Phase Behaviours of Gas Mixture 1, Gas Mixture 2 and pure CO_2.

Effects of SO_2 on CO_2 physical properties

Besides the above non-condensable impurities, SO_2 is a common condensable impurity in CO_2 streams. Due to the physical properties of SO_2, particularly the high critical temperature, it shows a different effect on phase and density behaviour of CO_2 mixtures. Because SO_2 can be compressed more easily compared with CO_2, mixing with SO_2 could increase the

compressibility of CO_2 and increase the density. An interesting result is shown in Figure 3.13. In a CO_2 mixture with 2.5% SO_2, the storage capacity would increase to above unity at 9 MPa. That is to say, around this pressure SO_2 increases rather than decreases CO_2 storage capacity. However, SO_2 is an acid gas which would cause corrosion on pipeline and well materials. It could also increase dissolution of caprock and compromise CO_2 storage integrity. These chemical effects need to be evaluated before co-injecting SO_2 with CO_2.

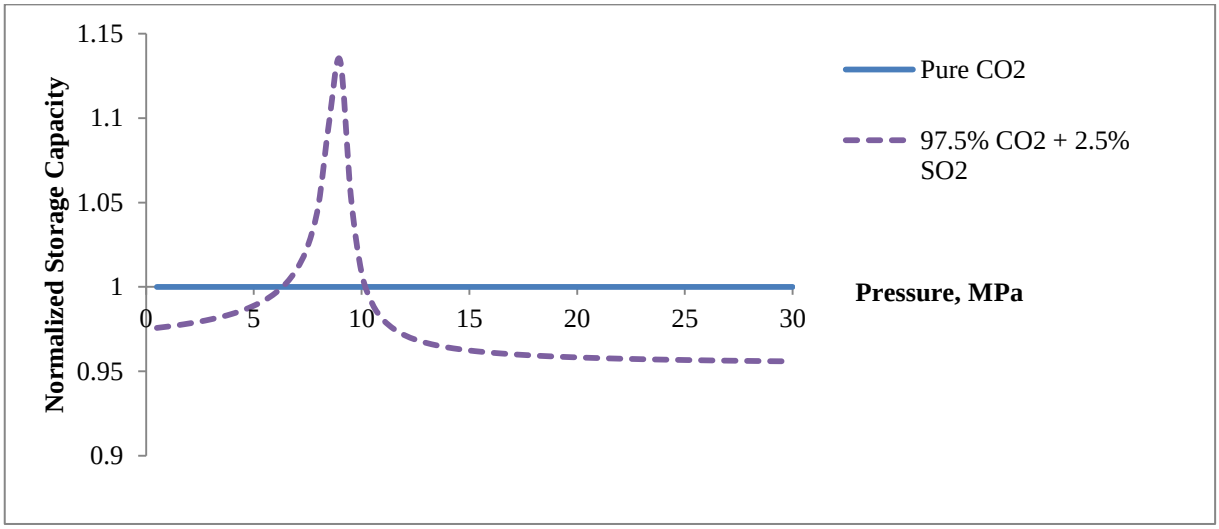

Figure 3.13 Calculated normalized capacity showing the effect of SO_2 on CO_2 storage capacity.

3.4 Conclusion

The densities of two different CO_2 mixtures were studied in this chapter through theoretical simulation and experimental testing. With these results, the effects of impurities on CO_2 storage capacity and buoyancy were evaluated further. To estimate the possible operation conditions of CCS, the phase behaviours were simulated by UNISIM software. Finally, the hypothesis, using Ar to represent the light impurities in order to simplify the calculation and experimental procedures, was discussed through the comparison of experimental data with calculated results.

1) Non-condensable impurities

a. With the non-condensable impurities involved, the density decreased, and a minimum point of normalized density could be found at each temperature. The highest reduction was 61% at 35 ℃ and 9 MPa.

b. Based on the normalized density, the CO_2 storage capacity was normalized and the results showed that the capacity decreased by as much as 65% under 35 ℃ and 9 MPa compared with pure CO_2.

c. The normalized buoyancy of impure CO_2 changed with pressure. At 35 ℃ it showed a peak value. The pressure dependence decreased with increasing temperature. Impurities could cause a more significant change in buoyancy in saline aquifers with lower saline density.

d. The phase behaviours changed significantly with the inclusion of non-condensable impurities. To avoid phase split, higher pressure and lower temperature are required in CO_2 transportation.

2) Condensable impurities

The inclusion of SO_2 showed different effects on CO_2 physical properties. Its presence increased the density and storage capacity.

3) The deviation of representing the light impurities by Ar was 5% in the evaluation of density change. In the calculation of CO_2 normalized capacity, the average difference of replacing light impurities by Ar was 3%. However, the second hypothesis was not well satisfied in the evaluation of phase behaviour.

3.5 References

1. Abbas, Z., T. Mezher, and M. R. M. Abu-Zahra. 2013. "CO2 Purification. Part I: Purification Requirement Review and the Selection of Impurities Deep Removal Technologies." *International Journal of Greenhouse Gas Control* 16: 324-334.

2. Cosham, A., R. J. Eiber, and E. B. Clark. 2010. "Gasdecom: Carbon Dioxide and Other Components.".

3. de Visser, E., C. Hendriks, M. Barrio, M. J. Mølnvik, G. de Koeijer, S. Liljemark, and Y. Le Gallo. 2008. "Dynamis CO2 Quality Recommendations." *International Journal of Greenhouse Gas Control* 2 (4): 478-484.

4. Ji, X. and C. Zhu. 2013. "Predicting Possible Effects of H2S Impurity on CO2 Transportation and Geological Storage." *Environmental Science and Technology* 47 (1): 55-62.

5. Kaufmann, K. D. 2010. "Impurity Types, Concentration Influence Hydraulic Design." *Oil and Gas Journal* 108 (14): 60-63.

6. Pipitone, G. and O. Bolland. 2009. "Power Generation with CO2 Capture: Technology for CO2 Purification." *International Journal of Greenhouse Gas Control* 3 (5): 528-534.

7. Sanpasertparnich, T., R. Idem, I. Bolea, D. deMontigny, and P. Tontiwachwuthikul. 2010. "Integration of Post-Combustion Capture and Storage into a Pulverized Coal-Fired Power Plant." *International Journal of Greenhouse Gas Control* 4 (3): 499-510.

8. Wang, J., D. Ryan, E. J. Anthony, A. Wigston, L. Basava-Reddi, and N. Wildgust. 2012. "The Effect of Impurities in Oxyfuel Flue Gas on CO2 Storage Capacity." International Journal of Greenhouse Gas Control 11: 158-162.

9. Wang, J., D. Ryan, E. J. Anthony, N. Wildgust, and T. Aiken. 2011. "Effects of Impurities on CO2 Transport, Injection and Storage.".

Chapter 4

The Geochemical Reactions of CO_2 Mixtures in Saline-aquifer Storage Sites

Abstract

The geochemical reactions of CO_2 mixtures in saline aquifers were studied in this chapter. Small scale batch reactions were conducted. To describe the effects of CO_2 mixture on aquifer system, the physical and chemical changes in the reactors containing CO_2 with impurities were compared with the changes in the reactor containing pure CO_2 after a 45-day period of reaction. In addition, modelling work was performed in conjunction with lab tests to provide the theoretical explanation for the experimental results. Both the calculated and experimental results showed a similar trend of change before and after the reaction of each reactor.

After the 45-day period, the pH of the systems subjected to pure CO_2 dropped from ~6.5 to ~5.8. With the presence of impurities, the formation of sulphuric acid caused a drastic decrease in pH. The lowest pH was found in the reactors which were reacted with CO_2+SO_2+O_2 in each group. The XRD results showed that the mineral phases of solid sample were intensively involved in the chemical reaction. A combined analysis of XRD with ion results suggested that dissolution and precipitation were the two major chemical processes brought about by the reactions. Finally, the porosity, which was considered as the most important aspect for CO_2 injection, was quantified by the XRD results and TDS. Even though the formation of $CaSO_4$ blocked the pores of rock mineral, the dissolution was still dominant in this geochemical reaction. An equation was therefore proposed in order to quantify the change of porosity. The highest increase of the porosity was from 0.141 to 0.266, and highest reduction was from 0.147 to 0.125.

Keywords: CO_2 storage, impurities, chemical effects, PHREEQC, aquifer.

4.1 Introduction

Generally, it is accepted that the main cause of the global warming is the increase in atmospheric concentration of greenhouse gas, such as carbon dioxide (CO_2), methane (CH_4) and nitrous oxide (N_2O). From the IPCC (intergovernmental panel on climate change) report, CO_2, whose atmospheric concentration has risen from pre-industrial levels of 280 ppm to 380 ppm in 2005, is the most important greenhouse gas, being responsible for about 2/3 of the enhanced greenhouse effect. Many studies were developed in order to seek a balance between the economic development and environmental protection. Carbon capture and storage (CCS) is a technology aiming at reducing the concentration of atmospheric carbon dioxide. Several capture options and large treatment capacity make the application of CCS flexible.

Deep saline aquifers, depleted oil-gas fields and non-exploitable coal streams are three different sites which are suitable candidates for CO_2 geological storage. Among them, deep saline aquifers, which have an estimated potential storage volume of up to 10,000 Gt CO_2 and are nearly ubiquitous worldwide, appear to be the most promising option (Jung et al., 2013). However, CO_2 reactions with the reservoir in the presence of water could cause changes in the reservoir and caprock.

Carbon dioxide captured from a power platform always contains various impurities such as N_2, O_2, SO_2, Ar and H_2S. The purification of this impure gas, however, is inefficient and uneconomic (Ji and Zhu, 2013), so co-capture and co-injection of these impurities with CO_2 have been considered in recent studies. Among the various impurities, the acid gases, such as SO_2 and NO_2, would form strong acids with water, which may react with rocks and cause corrosion on the pipeline and well materials. Therefore, an appropriate CCS system should be designed taking into account of these chemical effects.

Based on the previous studies (Wilke et al., 2012; Knauss et al., 2005; Gunter et al., 2000; Xu et al., 2007; Jacquemet et al., 2009), the acids formed by acid gases could decrease the pH drastically due to their high acidities. Further, some solids, which have low solubility in carbonic acid formed by pure CO_2, could dissolve in these stronger acids. Therefore, more dissolution of rock minerals would happen compared with pure CO_2 (Ellis et al., 2010; Wilke et al., 2012). In addition to the dissolution, some precipitation processes would also occur through the reaction between Ca^{2+} and SO_4^{2-}. The dissolution and precipitation are

two major factors which could influence the permeability and porosity of the rock(Bacon et al., 2009; André et al., 2007; Pruess and García, 2002; Kharaka et al., 2006; Gunter et al., 1996; Bachu et al., 2005; Li et al., 2011b; Gunter et al., 2000; Jacquemet et al., 2009; Crandell et al., 2010; Knauss et al., 2005).

Furthermore, some oxidants, like oxygen, would increase the acidity or accelerate the formation of sulphuric acid. During the CO_2 storage, oxides could influence the composition of rock by changing their stability and solubility. For instance, Jung et al. (2013) studied the potential impact of co-injected oxygen on the interaction between the CO_2-brine and shale caprock at ~10 MPa and ~75 ℃. In the presence of oxygen, the dissolution of calcite and dolomite was enhanced and pyrite was oxidized. These chemical processes subsequently resulted in the precipitation of Fe (III) oxides and gypsum ($CaSO_4 \cdot 2H_2O$). Their experimental and modeling results both indicated the interaction between shale caprock and CO_2 with oxygen can exert significant impacts on brine pH, solubility of carbonate minerals, and stability of sulphide minerals.

The maximum concentration of SO_2 for CO_2 storage studies found in the literature was 1.5%, which was the highest concentration of all acid gas impurities (SO_2, H_2S, COS and NO_x). Thus, SO_2 has been considered as the main acid gas impurity. According to the literature review, studies for the reactions of the CO_2-SO_2 mixtures and rock minerals were mainly conducted through modelling (Bacon et al., 2009; Crandell et al., 2010; Knauss et al., 2005; Nohra et al., 2012; Koenen et al., 2011; Ellis et al., 2010; Xu et al., 2007). Compared with modelling studies, experimental studies were limited (Wilke et al., 2012).

This chapter presents experimental test and computer simulation results for geochemical reactions between CO_2 mixtures, brine solutions and rock minerals. The chemical effects were quantified by comparing the pH, solubility, TDS (total dissolved solutes) and the concentration of different main solutes species before and after the reactions. Along with the discussion of the effects on porosity of reservoir rock, the effects of acidic impurities on CO_2 injectivity was discussed. Besides, the effects on the corrosion of pipeline material were discussed for the safety of CCS applications.

4.2 Methodologies

4.2.1 Sample description

Generally, a regular geological survey must be conducted before the industrial operation of CO_2 storage. According to the evaluation of potential storage strata, possible risks and environmental impacts, the CCS chain should be designed depending on these factors with local features.

The total emissions of Canada's anthropogenic greenhouse gas were 690 Mt of CO_2 equivalent (Environment Canada, 2009). Based on the situation of power and energy industrial distribution in Canada, emissions from Alberta were estimated 48.9%, and where 80% of electricity is generated by fossil fuel (Talman et al. 2012). To estimate the storage capacity for CO_2 in Alberta, various studies (e.g., USDOE, 2010) and surveys were initiated to explore the potential storage sites. The 2010-2011 Geological Survey of Canada (GSC) report identifies the Alberta Basin and the Canadian part of the Williston basin as the two greatest potential storage regions for the implementation of CCS, both in terms of the storage capacity and location of large stationary resources amenable to CO_2 capture.

The geological formation evaluated in this study is the Basal Cambrian Saline Aquifer (termed as the Basal Aquifer). The Basal Aquifer is a succession of Cambrian to Silurian sandstone and carbonate formations that overlie the basal Precambrian bedrock of the Canadian Shield in the Western Canada Sedimentary Basin. As shown in Figure 1.3, the Basal Aquifer covers the southern half of Alberta and Saskatchewan and the southwest corner of Manitoba, and extends into the Northern Plains region of the United States. Owning to fossil fuel exploration in Alberta, the majority of oil and gas reservoirs are still in production. For instance, the sedimentary succession from Devonian strata to Tertiary strata is penetrated by countless wells for natural resource extraction (Talman et al. 2012). Compared to Devonian-Cretaceous sedimentary succession, most of the Cambrian-Silurian strata in Alberta basin and in the Canadian part of Williston part does not contain fossil fuels and is penetrated comparatively fewer wells. Therefore, this sedimentary succession could be a potential storage site with a lower risk of CO_2 leakage. In addition, the water salinity in this area increases with the depth. The formations composing the Basal Aquifer are hydraulically connected (hence the treatment as one storage unit), and capped by a thick succession of shales which act as the primary confining unit. These features create a

situation where fresh water would be pushed up to a relatively lower depth by the high-density saline water due to buoyancy and therefore decreases the environmental hazards on the available natural resources. The large area of the basin in combination with the low permeability, lack of fossil fuels and high salinity, make the Basal Aquifer an attractive storage target.

The Basal Aquifer is penetrated by 533 wells in the region which are suitable for CO_2 storage as determined in Phase 1 of Alberta Innovates Technology Futures (AITF) Basal Aquifer study by Bachu et al. (2011). For the Phase 1 study, 12 cored wells were selected for sampling and analysis. Figure 4.1 shows the mapped locations of these wells.

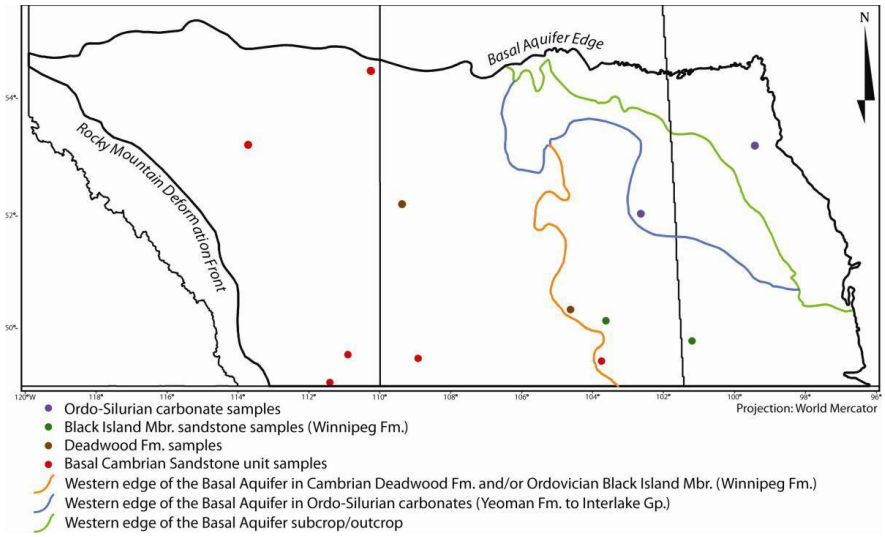

Figure 4.1 Location of wells from which samples were collected and analyzed for mineralogy of the Basal Aquifer in the Prairie region of Canada (Bachu, et al., 2011).

Core samples in this study were collected from the cored Basal Aquifer portions of the wells at Alberta's Core Research Facility in Calgary. Samples were extracted from the previously slabbed core by Core Research Facility technicians. One of the wells is located north of Edmonton, in the Cold Lake area. The other is near Medicine Hat and is also used in the AITF study. Carbon dioxide emissions in the area around Cold Lake were 4.3 Mt CO_2 according to emissions data available through Environment Canada's 2009 greenhouse gas inventory 1 and were from Shell's Orion Complex refinery, and Imperial Oil Resources Cold Lake refinery (Wigston and Ryan 2011). Shell's Quest project is located in the Cold

Lake area. Carbon dioxide emissions from the Medicine Hat area were ~1.7 Mt CO_2 in 2009 (Wigston and Ryan 2011). Table 4.1 shows the details on the samples that were taken from the two cores from Cold Lake and Medicine Hat areas.

Table 4.1 List of wells and core samples for laboratory testing

Well ID	Location	Porosity	Depth (mbgs*)	Mass (g)
10-11-067-12W4	Closet of Cold Lake (West of it)	≈ 0.147	1459.08	65.64
			1459.08	79.00
			1463.01	64.60
			1463.01	63.49
			1465.48	89.89
06-29-007-07W4	Medicine Hat	≈ 0.141	2124.76	62.05
			2124.76	63.40
			2125.10	64.16
			2125.10	67.85
			2125.43	57.83

** mbgs denotes meters below ground surface.*

4.2.2 Experimental method

The original well water and solid samples were analyzed after collecting from Alberta and the results are shown in Tables 4.2 and 4.3, respectively. The analysis methods are discussed in the next section.

Table 4.2 Original well water analyses

Well ID	Depth (m)	Pressure (kPa/psi)	Temp (°C)	Composition (mg/L)					
				TDS	Na	Ca	Mg	Cl	SO_4
10-11-067-12W4	1460	13650/1979	35	310521	118797	1796	688	186031	3111
06-29-007-07W4	2125	18750/2719	50	49686	16009	2200	267	25250	4160

Table 4.3 Original solid sample analyses by XRD

Mineral Phase	10-11-067-12W4	06-29-007-07W4
Quartz low	94.70%	97.90%
Sodalite group	0.52%	0.80%
Kaolinite	0.60%	0.30%
Dobassite	0.98%	1.00%
Microcline	1.09%	---
Anhydrite	1.65%	---
Halite	0.48%	---
Weight (%)	100.02%	100.00%

In order to quantify the geochemical reactions, seven reactors were set for the batch reactions between the gas mixtures, aqueous solutions, and solid samples of rock minerals. Considering the limitation of equipment and the safety, the pressure was set at 1500 psi, which was the highest achievable pressure of the reactor. As shown in Table 4.4, the reactors were divided in two groups, 10-11-067-12W4 (12W4) and 06-29-007-07W4 (7W4). In group12W4, 400 mL brine solution was placed in contact with 49 g consistent solid sample at 1500 psi and 35 °C for 45 days in each reactor. In group 7W4, 400 mL brine solution reacted with 41 g consistent solid sample at 1500 psi, 50 °C for a same time period in each reactor. These ratios of solid to liquid samples were calculated by the initial ratios of well collections. There were three different gas mixtures for testing the chemical effects on rock minerals, pure CO_2, CO_2 (97.5%) - SO_2 (2.5%), and CO_2 (95%) - SO_2 (2.5%) - O_2 (2.5%), with a duplicate control reactor for N_2 in group 12W4.

Table 4.4a Overview of the batch reaction

	Reactor 1	**Reactor 2**	**Reactor 3**	**Reactor 4**
Gas Injection	N_2	CO_2	CO_2-SO_2	CO_2-SO_2-O_2
Pressure	1500 psi			
Temperature	35 °C			
Brine Solution	400 mL			
Rock Sample	49 g			
Well ID	10-11-067-12W4			

Table 4.4b Overview of the batch reaction

	Reactor 5	**Reactor 6**	**Reactor 7**
Gas Injection	CO_2	CO_2-SO_2	CO_2-SO_2-O_2
Pressure	1500 psi		
Temperature	50 °C		
Brine Solution	400 mL		
Rock Sample	41 g		
Well ID	06-29-007-07W4		

Because the total volume of brine solution required for the experiments in these reactors exceeded the volume of liquid sample collected from Alberta, two brine solutions were made in accordance with the compositions and ID numbers of the two liquid samples from Alberta. NaCl, Na_2SO_4, $CaCl_2$ and $MgCl_2 \cdot 6H_2O$ were used to provide the four chemical species in the liquid samples, as shown in Table 4.5.

Table 4.5 Chemical compositions of brine solutions

Brine Solution ID	**$CaCl_2$ (g/L)**	**Na_2SO_4 (g/L)**	**$MgCl_2 \cdot 6H_2O$ (g/L)**	**NaCl (g/L)**
10-11-067-12W4	5.38	4.98	6.23	322.82
06-29-007-07W4	6.24	5.51	2.29	36.53

Figures 4.2 and 4.3 show the sketch and photograph of the experimental setup. The total volume of Reactor 1 is 0.9 L, and that of Reactors 2-7 are the same 1.3 L. To avoid chemical corrosion, all the reactors were coated with Teflon. Initially, the solid sample and brine were

added in the reactor. To make sure the solids and brine were mixed homogenously, N_2 was introduced first in the reactors for bubbling. And then, the test gas was injected by high pressure syringe-pump. After purging for 30 s, all the valves were closed for pressurizing. The reactors were heated by heat-jackets and their temperatures and pressures were monitored by controllers.

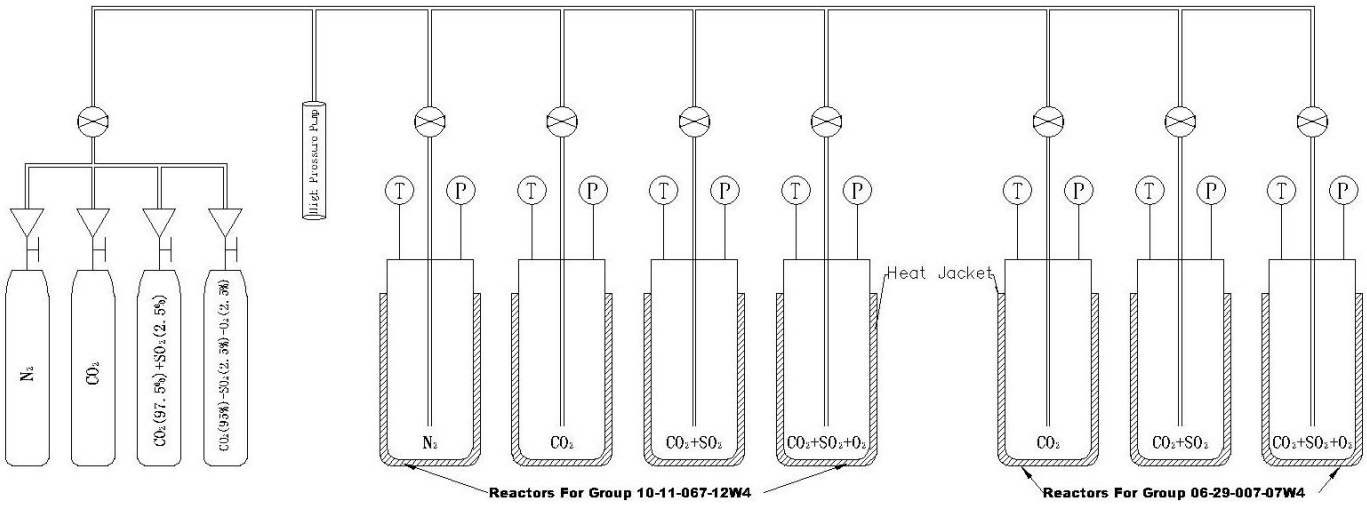

Figure 4.2 Schematic diagram of experimental setup

Figure 4.3 Reactor for static test

Due to the delay of heat transfer from heat jacket to reactants to thermometer and the dependence of pressure on temperature, there were oscillation ranges of temperature and pressure with the average conditions of 35 or 50 °C and 1500 psi. To check the leakages of the reactors, the average of the highest and lowest temperature and pressure were compared with 35 or 50 °C and 1500 psi. In this experiment, the oscillation of temperature was 1-2 °C and that of pressure was around 100 psi. The gas leakage was controlled in < 50 psi.

Reactors were shut down after 45 days. The pH and the conductivities of the liquids were measured in the sealed box and the solids were analyzed by X-ray Diffraction (XRD) to identify the mineral phase and by X-ray Fluorescence (XRF) to identify the elements. Combustion infrared detection technique (LECO-S) was used to accurately quantify the concentration of sulphur in the solid. Secondary Electron Microscopy (SEM) equipped with Energy Dispersive X-ray (EDX) was chosen to study the morphology. All the solid samples were dried to make sure water was evaporated before the characterization. The liquids analyses were performed by MAXXAM Company.

4.2.3 Modelling method (PHREEQC)

To simulate the geochemical reactions between the gas mixtures, brine solutions, and rock minerals, PHREEQC Modelling software was used to calculate the physical properties of reaction system and the concentrations of different chemical species before and after reaction.

PHREEQC is a computing code, written in C and C++ programming languages, used for the geochemical calculations. PHREEQC analyzes the input files using several different aqueous models: two ion-association aqueous models (the Lawrence Livermore National Laboratory model and WATEQ4F), a Pitzer specific-ion-interaction aqueous model, and the SIT (Specific ion Interaction Theory) aqueous model. Depending on this mechanism, PHREEQC has the capabilities for speciation and saturation-index calculation, batch-reaction with reversible and irreversible reactions, which includes aqueous, gas, solid-solution, ion-exchange equilibrium and specified mole transfers of reactants with temperature and pressure changes. For the reactor samples, the salinity of water was high, which exceeded the range of application for the Debye-Hückel theory. Thus, the Pitzer aqueous model was selected instead of Debye-Hückel model. The volumetric properties of

gases were calculated by the Peng-Robinson equation of state with the constants of different gas defined in the input files.

In this work, the data of solutions prepared before the experiments, which is shown in Table 4.5, was used as the initial brine solution in the input file. The results of XRD, which is shown in Table 4.3, were used as the solid composition in the PHREEQC modelling. Other reaction conditions, such as temperature and pressure, are consistent with experimental method.

4.3 Analytical methods and results

4.3.1 Solid characterization

4.3.1.1 XRD

The chemical formulas and their corresponding densities of all the mineral crystals in XRD are listed in Table 4.6.

Table 4.6 Chemical formulas of mineral phases in XRD

Mineral Phase	Chemical Compound	Density (g/cm^3)
Quartz	SiO_2	2.66
Sodalite group	$Na_8Al_6(SiO_4)_6(BrO_3)_{1.77}(OH)_{0.23}$	2.57
Kaolinite	$Al_2Si_2O_5(OH)_4$	2.63
Microcline	$K(AlSi_3O_8)$	2.56
Dobassite	$Al_{4.5}(Al_{.8}Si_{3.2})O_{10}(OH)_8$	2.68
Anhydrite	$CaSO_4$	2.97
Halite	NaCl	2.16
Gypsum	$CaSO_4 \cdot 2H_2O$	2.32
Sulphur	S	2.06
Siderite	$Fe(CO_3)$	3.96
Iron Carbonate Hydroxide Hydrate	$(Fe_3(OH)_6)((CO_3)_{0.5}(H_2O)_{1.45})$	3.40

10-11-067-12W4. Figure 4.4 (A) and (B) show the XRD results of solid sample of 12W4 after reaction and compared with the original. The percentages of quartz in the solids decreased successively from the original 94.70% to 70.66% of Reactor 4; however, halite showed an opposite trend which increased from the original 0.48% to the highest 24.36%. The amount of kaolinite was slightly lower in the Reactors 1 and 2; however, it was completely absent in the solid samples from the Reactors 3 and 4, which contained the CO_2

mixture with SO_2. Microcline was undetectable in both the solid samples from Reactors 2, 3 and 4, which were subjected to pure CO_2 or CO_2 mixture. The ratio of dobassite decreased to half of the original in both reactors of this group. Anhydrite was formed after the reactions and its highest amount was around 3.90% shown in Reactors 3 and 4. The amount of sodalite group increased from the initial 0.5% to 0.6% in both Reactors 1 and 3, and it almost remained unchanged in Reactors 2 and 4. Finally, sulphur was detected in the solid sample from Reactor 4 subjected to CO_2+SO_2+O_2.

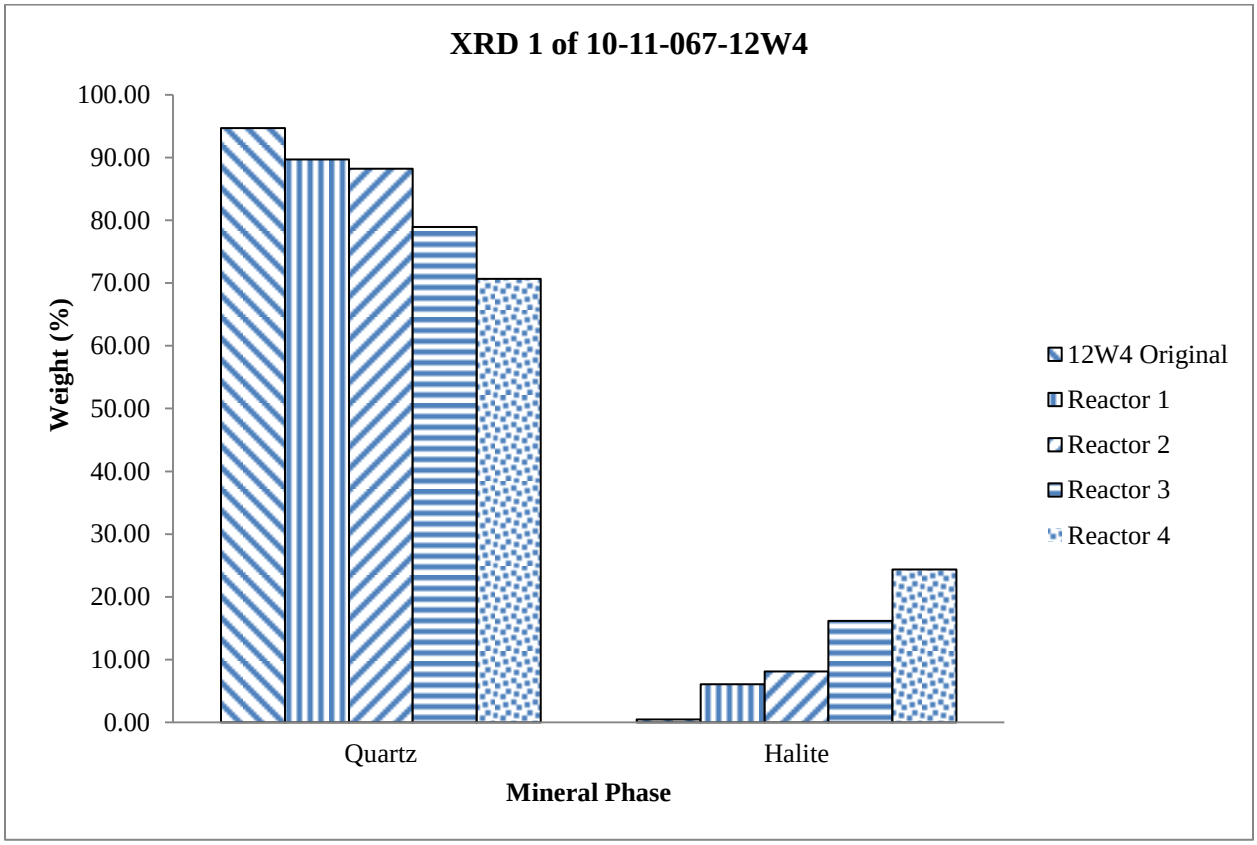

(A)

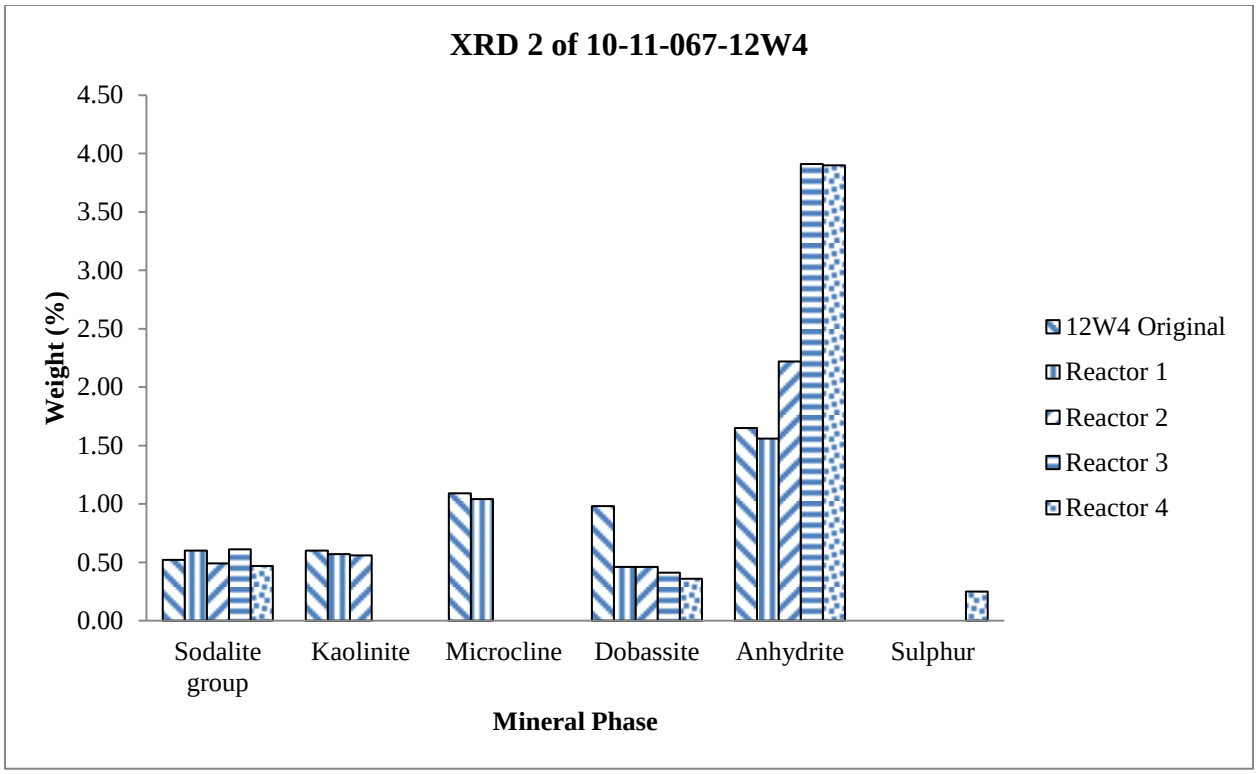

(B)

Figure 4.4 XRD results of 10-11-067-12W4.

06-29-007-07W4. Figures 4.5 (A) and (B) show the XRD results of solid sample of 07W4 after reactions and compared with the original. The amount of quartz decreased with the impurities involved in the reactions and the highest reduction was from the original 97.90% to 91.87%, which was observed in Reactor 6 containing mixture CO_2+SO_2. Sodalite group showed a successively decreased trend from the original 0.80% to 0.51% of Reactor 7; however, halite showed an opposite trend which was crystalized after reactions and its concentration increased from 0.42% of Reactor 5 to 1.17% of Reactor 7. Similar to group 12W4, the ratio of dobassite decreased to half of the original in both reactors of this group. Anhydrite was detected after the batch reactions and the highest one is 3.11%, which was observed in Reactor 6. Sulphur was formed in Reactors 6 and 7, and the highest amount was 2.79% detected from Reactor 6. Finally, some iron mineral phases, iron carbonate hydroxide hydrate and siderite, were observed after the reaction in Reactor 7 containing CO_2+SO_2+O_2. Kaolinite did not show any significant differences before and after the reactions.

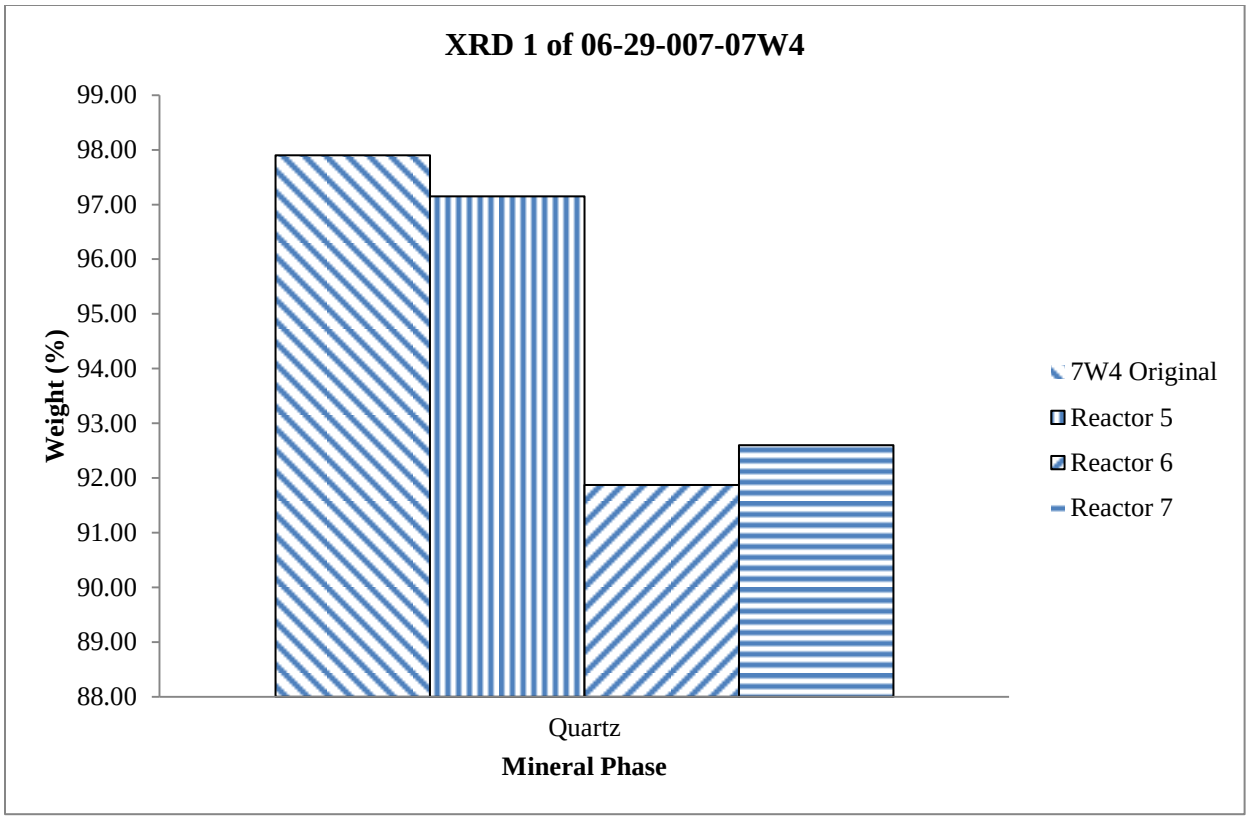

(A)

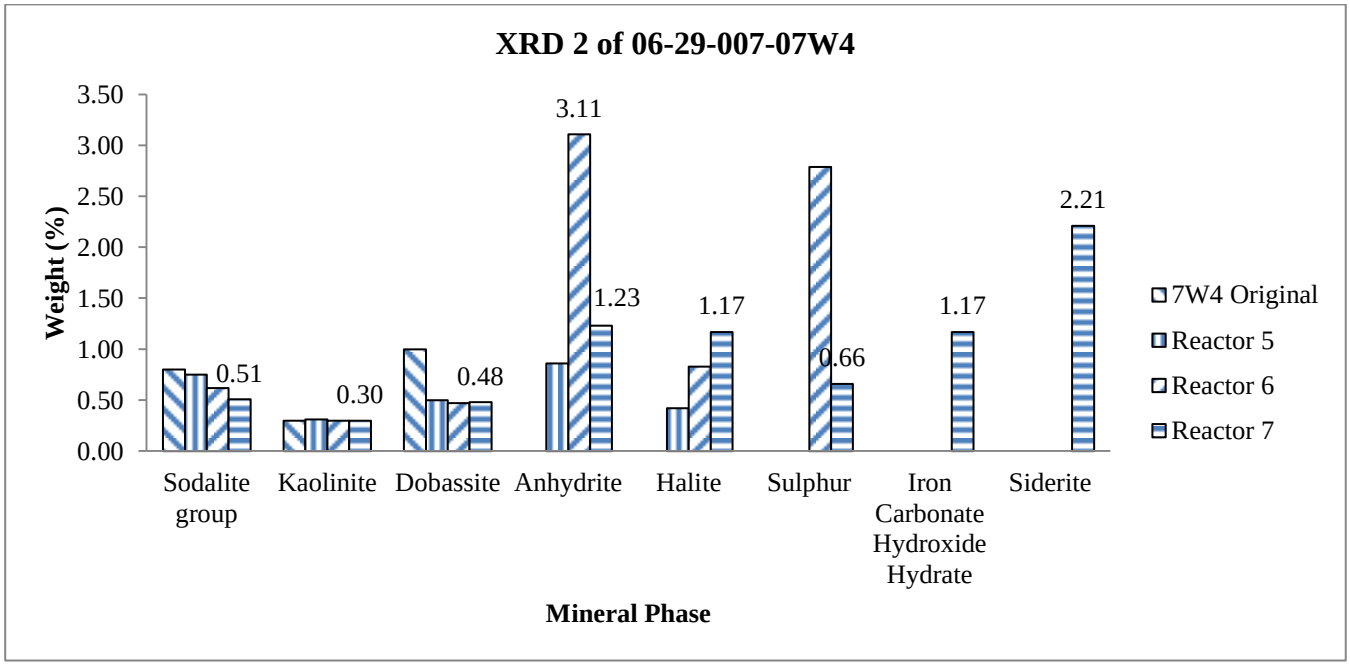

(B)

Figure 4.5 XRD results of 06-29-007-07W4.

4.3.1.2 XRF and LECO-S

Because both samples were quartz dominant, the changes of the other elements would be not be recognized easily if the high concentration SiO_2 is included in Figure 4.6. Thus, SiO_2 is not shown in this figure. The weight percentages of SiO_2 from Reactors 1 to 4 were 86.94%, 84.81%, 75.26% and 65.24% in group 12W4 and from Reactors 5 to 7 were 97.52%, 88.1% and 73.74% in group 7W4, respectively. Therefore, the amount of Si decreased with the concentration of impurities increased in the gas mixture and the highest reduction could be detected in the Reactors 4 and 7, which were subjected to the CO_2 mixture containing impurities SO_2 and O_2. The results of XRF and LECO-S are shown in Figure 4.6 (A) and (B). In group 12W4, the concentration of sulphur and Ca increased with the presence of SO_2 in the gas mixture and the highest weight percentage of sulphur was 1.28% and that of Ca was 1.58% could be both observed in the solid sample from Reactor 4. Na showed a notable change after the reaction, and the concentration was the lowest 3.62% detected from Reactor 2 to the highest was 12.59% detected from Reactor 4. Other metal ions did not show any obvious differences. In group 7W4, the original solid sample did not show any detectable S and Na. After the reaction with SO_2, the highest concentration of S could be observed 4.71% in Reactor 6 and the second highest was 2.5% in Reactor 7. Na was detected in the solid sample from Reactors 6 and 7, which contained CO_2 mixture with SO_2. Comparing with the other reactors, solid from Reactor 7 showed a high concentration of Fe, which is 7.32%. Other metal ions did not show any obvious differences.

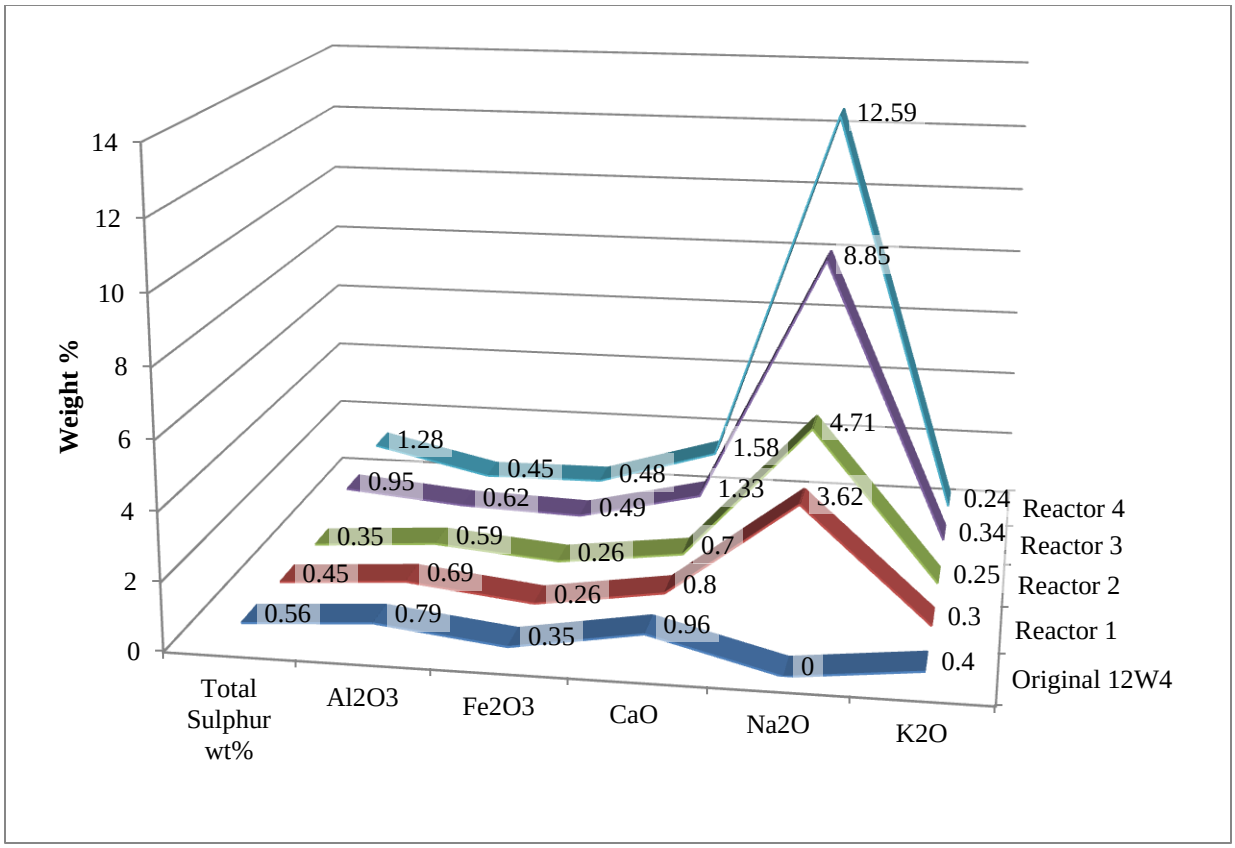

(A)

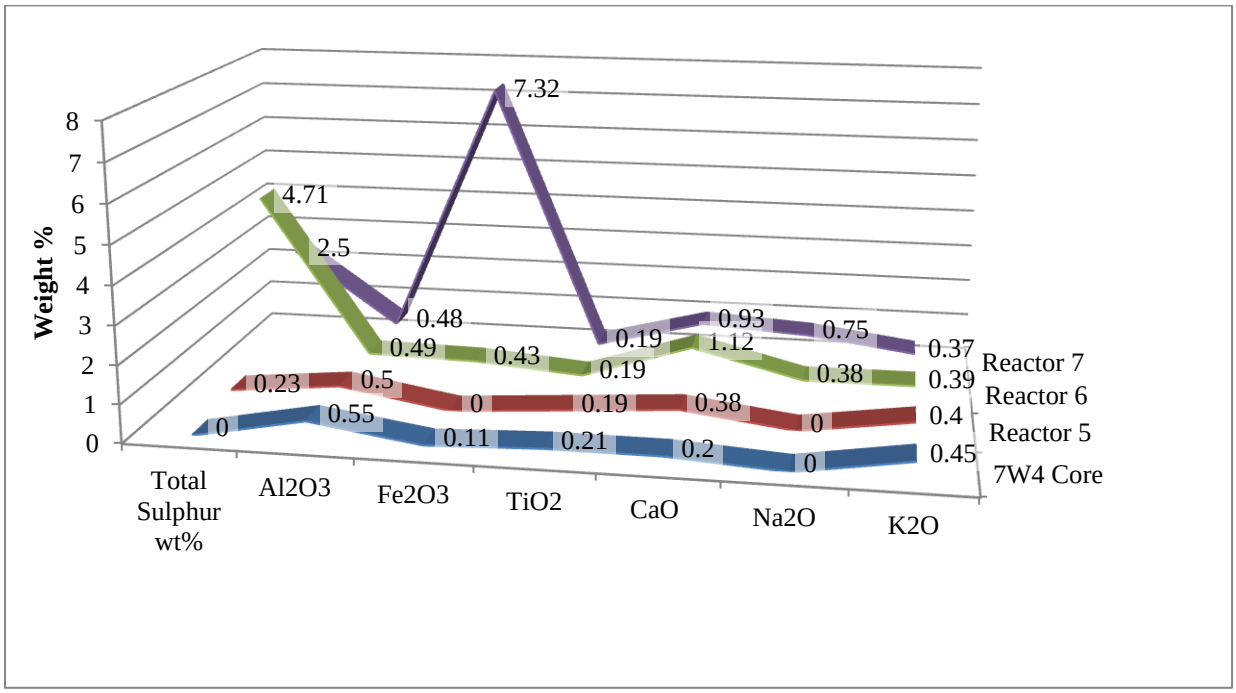

(B)

Figure 4.6 Results of XRF and LECO-S. (A): Group 12W4. (B): Group 7W4.

4.3.1.3 SEM-EDS

The results of SEM are presented in Figure 4.7 and the corresponding EDS results are shown in Table 4.7. As shown in the figures of originals, the core samples were well-structured rock particles with smooth surfaces. EDS shows that these quartz-dominant rocks were consisted of different elements. The solid sample of Reactor 1, which was the duplicate of group 12W4 subjected to N_2 only, was covered by a number of small speckles, which were NaCl accumulated after the reactions. Due to the formation of carbonic acid, minor amount dissolution could be detected on rocks from Reactor 2 and Reactor 5. However, the dissolution increased with the inclusion of SO_2 in CO_2, and the particles dissolved by sulphuric acid were replaced by the NaCl crystals (white and light cubes), which is shown in figures of Reactor 3 and Reactor 6. The most serious weathering can be found in the samples from Reactor 4 and Reactor 7. In the presence of O_2, the surface of particles turned coarse due to the reactions with strong acidity, and the debris interlaced between every larger particle.

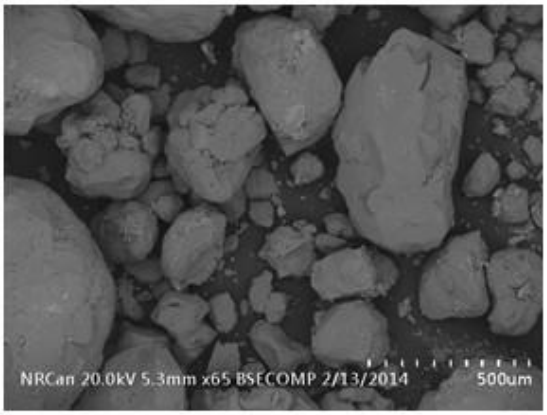

Original 12W4

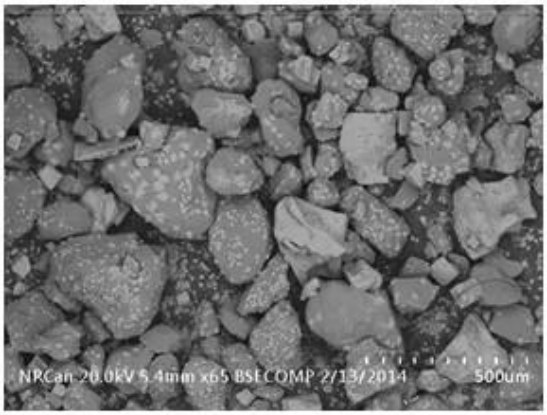

Reactor 1

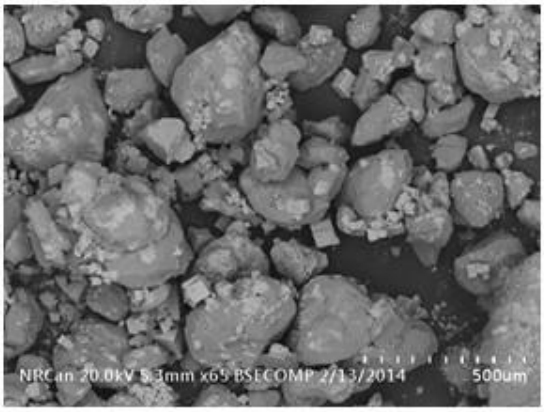

Reactor 2

Reactor 3

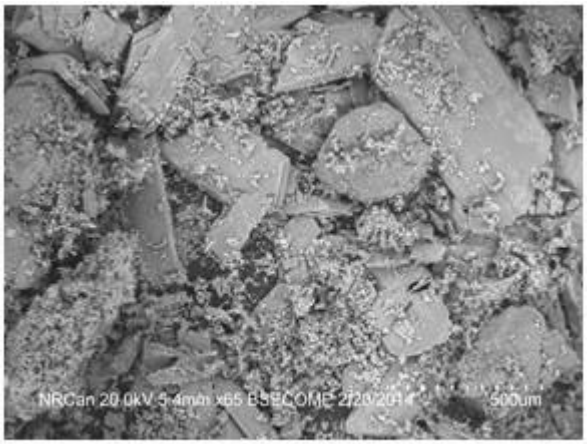

Reactor 4

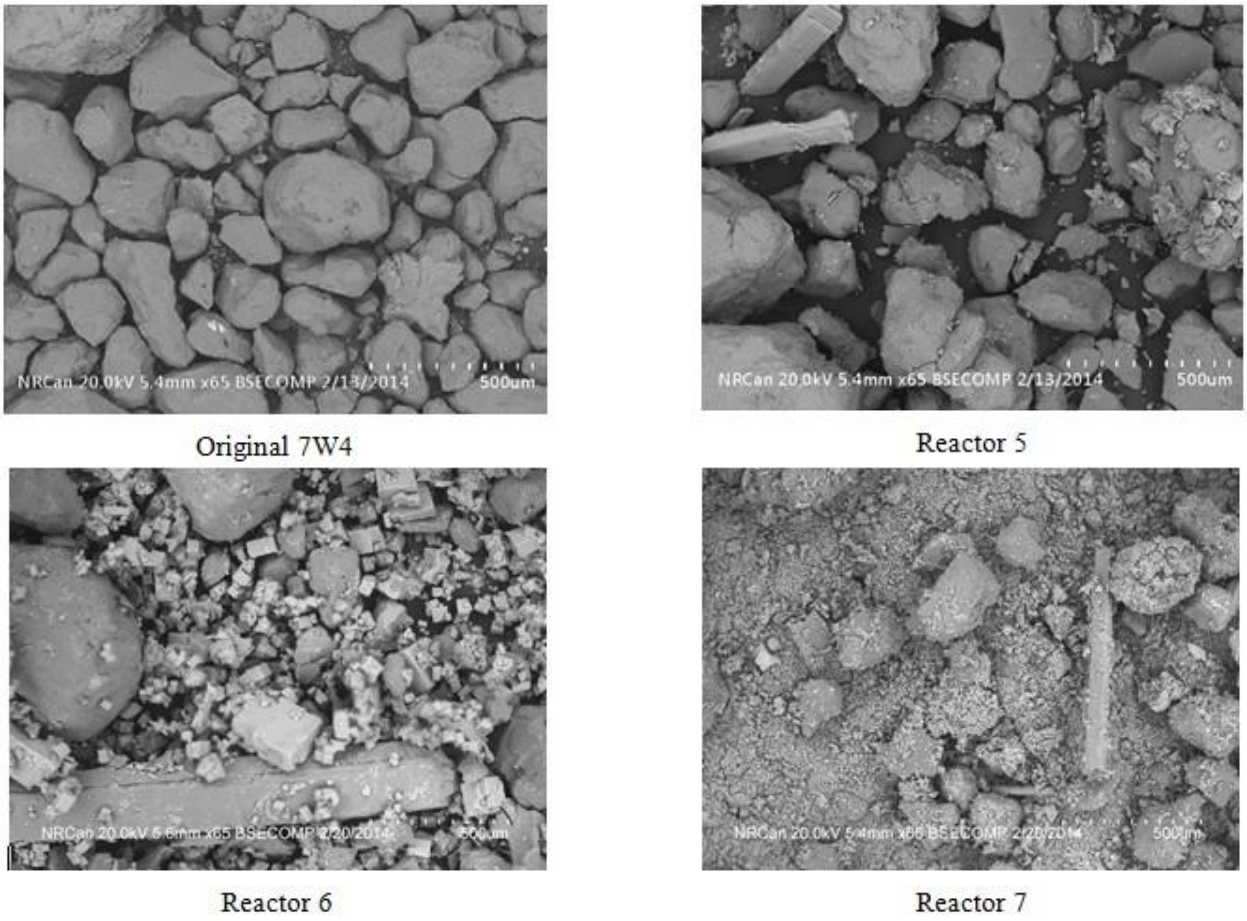

Figure 4.7 SEM results of solid samples.

Table 4.7 EDS results

Element/Avg.wt%	O	Na	Mg	Al	Si	S	Cl	K	Ca	Fe
Original 12W4	50.47	1.74	0.00	2.43	39.51	0.34	2.16	0.96	0.52	1.89
Reactor 1	41.62	12.92	0.00	2.30	18.24	0.97	19.73	1.02	1.17	1.92
Reactor 2	32.69	14.88	0.00	2.10	21.73	0.74	24.49	0.85	0.79	1.42
Reactor 3	35.43	13.67	0.46	1.08	19.18	4.11	21.83	0.48	1.65	1.87
Reactor 4	34.97	15.36	0.31	0.81	16.79	5.48	22.05	0.42	0.90	2.38
Original 7W4	52.45	0.00	0.00	0.63	45.89	0.00	0.00	0.76	0.21	0.07
Reactor 5	47.30	1.68	0.00	0.67	42.55	1.86	3.13	0.81	1.79	0.00
Reactor 6	31.68	17.71	0.25	0.64	12	6.08	25.79	0.33	2.26	2.68
Reactor 7	39.53	4.14	0.01	0.27	14.44	7.18	5.01	0.25	2.07	15.64

4.3.2 Liquids analyses

Table 4.8 shows the analysis results of initial brine and liquids after reaction. The pH values of the liquids from reactors, which were reacted with CO_2, dropped to around 5.8 in both groups. With the presence of SO_2, the pH dropped significantly to around 2. The highest concentration of inorganic carbon could be found in the reactors subjected to pure CO_2. SO_4 increased with the presence of SO_2 in CO_2 mixture and the highest concentration could be observed after the reaction with the gas CO_2+SO_2+O_2. The concentration of Ca successively decreased in both groups with the components increased in the gas mixture. The Si and Al were detected in Reactors 3, 4, 6 and 7, which were subjected to CO_2 mixture. The Cl, Mg and Na did not show any notable changes. Some contaminants could be observed after the 45 days reactions, such as Fe, Cr, Mn and Ni. TDS (total dissolved solids) were calculated by the sum of concentrations of main chemical species (total inorganic carbon, total sulphur, Cl, Ca, Mg, Na, Al and Si). As the results shown in Table 4.8, the TDS successively increased with the concentration of impurities increased in the gas mixture in both groups 12W4 and 7W4.

Table 4.8 Results of liquid analyses

	12W4					7W4			
Reactor No.		**1**	**2**	**3**	**4**		**5**	**6**	**7**
Gas Injection	Initial	N_2	CO_2	CO_2+SO_2	CO_2+SO_2+O_2	Initial	CO_2	CO_2+SO_2	CO_2+SO_2+O_2
pH	6.21	6.37	5.77	0.8	1.73	6.87	5.83	1.85	3.9
Conductivity (μmho/cm)	292,400	246,350	239,450	224,200	197,500	68,500	66,782	81,865	80,700
Density	1.20	1.15	1.18	1.20	1.22	1.02		1.06	1.05
Total Inorganic Carbon (mg/L)	3	3	31	< 10	11	2	96	13	< 10
Cl (mg/L)	190,000	190,000	190,000	190,000	190,000	26,000	26,667	28,500	29,500
Total Sulphur (mg/L)	1,200	6,850	1,200	13,000	18,000	---	7,100	9,500	11,500
SO_4 (mg/L)	3,200	3,650	3,150	14,000	47,500	3,500	2,700	33,000	44,500
Ca (mg/L)	1,400	1,050	1,400	815	250	1,600	1,300	680	500
Mg (mg/L)	720	660	685	740	775	250	330	390	290
Na (mg/L)	110,000	98,000	110,000	100,000	99,500	15,000	17,000	14,500	13,000
Al (mg/L)	---	< 10	< 10	72	100	< 0.25	< 10	13	< 10
Si (mg/L)	---	< 20	< 20	52	54	---	< 20	88.5	62
TDS (mg/L)	**303,323**	**296,563**	**303,316**	**304,679**	**308,690**	**42,852**	**52,493**	**53,685**	**54,852**
Fe (mg/L)	---	---	22	6,400	17,000	---	120	10,400	20,000
Cr (mg/L)	---	---	3	1,450	4,100	---	2	2,600	480
Mn (mg/L)	---	---	---	115	340	---	3	165	530
K (mg/L)	---	120	100	110	105	62	< 100	< 100	< 100
Sr (mg/L)	24	22	23	20	17	29	26	23.5	14
Co (mg/L)	---	---	---	7	29	---	---	8	8
Mo (mg/L)	---	---	---	30	44	---	---	20.5	< 2
Ni (mg/L)	---	---	---	550	1,100	---	---	890	330
V (mg/L)	---	---	---	4	20	---	---	11	< 1

4.3.3 Simulation results

PHREEQC was used to simulate the batch reactions between brine solutions, rock minerals and CO_2 gas mixtures; and the results are shown in Table 4.9.

As a weak acid, the carbonic acid could only partially dissociate in aqueous solutions. So there exists an equilibrium chemical reaction in the water, which is shown in Eq. 18.

$$CO_2 + H_2O \leftrightarrow H_2CO_3 \leftrightarrow H^+ + HCO_3^- \leftrightarrow 2H^+ + CO_3^{2-} \qquad (18)$$

According to Chatelier's principle, the solubility and acidity of H_2CO_3 are sensitive to the experimental pressure. As shown in Table 4.9, there are two groups of results for each reactor simulated by PHREEQC. A group of chemical and physical parameters was simulated under the experimental conditions discussed in Table 4.4. Further, to investigate the pressure dependence, a secondary reaction was also simulated after the conditions were changed from 1500 psi and 35 or 50 °C to atmospheric pressure 1 atm and 25 °C, which were the conditions for the experimental measurement.

Table 4.9 Modelling results by PHREEQC

	12W4									7W4						
Reactor No.		**1**		**2**		**3**		**4**			**5**		**6**		**7**	
	Initial	N_2		CO_2		CO_2+SO_2		CO_2+SO_2+O_2		Initial	CO_2		CO_2+SO_2		CO_2+SO_2+O_2	
		Ex	Am	Ex	Am	Ex	Am	Ex	Am		Ex	Am	Ex	Am	Ex	Am
pH	6.372	6.259	6.435	3.533	5.142	0.056	0.045	-0.066	-0.078	6.691	3.254	4.569	0.214	0.185	0.105	0.078
Conductivity	415600	415124	336888	414786	336576	635944	462745	703232	512230	67466	108262	67484	460967	263402	558235	317051
Density	1.19	1.15	1.15	1.16	1.15	1.19	1.19	1.2	1.2	1.03	1.04	1.03	1.08	1.08	1.09	1.09
Ca (mol/L)	4.85E-02	1.77E-02		1.77E-02		5.72E-04		5.94E-04		5.63E-02	5.63E-02		5.73E-02		5.73E-02	
Cl (mol/L)	5.68E+00	4.52E+00		4.51E+00		4.46E+00		4.43E+00		7.60E-01	7.60E-01		7.75E-01		7.74E-01	
Mg (mol/L)	3.07E-02	3.07E-02		3.07E-02		3.12E-02		3.12E-02		1.13E-02	1.13E-02		1.15E-02		1.15E-02	
Na (mol/L)	5.59E+00	4.43E+00		4.43E+00		4.37E+00		4.34E+00		7.03E-01	7.03E-01		7.16E-01		7.16E-01	
S^{-2} (mol/L)	0.00E+00	0.00E+00		6.51E-15	1.75E-15	2.54E-01		0.00E+00		0.00E+00	5.82E-15	1.90E-14	2.65E-01		0.00E+00	
S_4 (mol/L)	0.00E+00	0.00E+00		0.00E+00		3.10E-16	6.23E-17	0.00E+00		0.00E+00	0.00E+00		4.41E-15	5.37E-16	0.00E+00	
SO_4 (mol/L)	3.51E-02	4.22E-03		4.29E-03		7.49E-01		1.01E+00		3.88E-02	3.88E-02		8.34E-01		1.07E+00	
Al (mol/L)	0.00E+00	5.87E-10		7.02E-04		1.04E-02		1.04E-02		0.00E+00	3.65E-04		2.55E-03		2.55E-03	
Si (mol/L)	0.00E+00	2.30E-05		2.25E-05		1.65E-05		1.51E-05		0.00E+00	1.77E-04		1.38E-04		1.30E-04	
C (mol/L)	0.00E+00	0.00E+00		4.58E-01	1.86E-02	3.68E-01	1.12E-02	3.40E-01	1.04E-02	0.00E+00	9.17E-01	2.91E-02	7.59E-01	2.63E-02	7.08E-01	2.47E-02
K (mol/L)	0.00E+00	0.00E+00		4.75E-03		4.84E-03		4.84E-03		0.00E+00	0.00E+00		0.00E+00		0.00E+00	
TDS (mg/L)	336,420	264,000		270,000	264,000	345,000	340,000	359,000	355,000	49,400	60,400	49,700	144,000	135,000	157,000	149,000

'Ex' means the results had been simulated under the experimental conditions (35 or 50 °C and 1500 psi). 'Am' means the results had been simulated under the ambient conditions (25 °C and 1 atm).

As shown in Table 4.9, the pH of the liquids that had reacted with CO_2 dropped to around 3.4 under the experimental conditions, and increased to around 4.8 after the pressure and temperature changed to 1 atm and 25 °C, respectively. Some low pH values could be observed in the Reactors 3, 4, 6 and 7, especially the pH of liquid from Reactor 4, which was negative. However, the pH of these reactors did not show any notable changes under different pressure and temperature. The conductivities increased when the pH decreased in each group and decreased after the reaction conditions dropped to 1 atm and 25 °C in each reactor. The concentration of Ca decreased after the reactions in 12W4 and the highest reduction could be observed in Reactors 3 and 4 which were reacted with a gas mixture containing SO_2. However, Ca did not show any significant changes in 7W4. Because CO_2 and SO_2 were involved in the reactions, the concentration of total carbon and sulphur increased in both groups. For S, the highest concentration could be found in the reactor where SO_2 and O_2 were introduced as impurities. Because the solubility of CO_2 in the water is sensitive to the pressure as previously discussed, the concentration of total C would decrease when the pressure dropped. The CO_2 would release from water to the gas phase and the conductivity therefore decreased with this tendency of C concentration. The Cl, Mg and Na concentrations did not show obvious differences before and after the reaction. Some ions, which were not detected in the initial brine solution, could be found as ion species after the reaction, such as Al, Si and K.

The calculated TDS showed a similar trend to that of the experimental results. TDS increased with the presence of impurities in gas mixture and the highest TDS were observed in the reactors reacted with impurity O_2 in each group.

The saturation index of each reactor was also calculated by PHREEQC. As observed from Table 4.10, the saturation index of most minerals increased as the pressure dropped from experimental conditions to 1 atm. However, several minerals such as anhydrite showed an opposite trend. The saturation state dropped with the impurities involved, reflecting the relationship between the pH and mineral equilibrium. Kaolinite and microcline were significantly affected by the change of pH.

Table 4.10a Calculated equilibrium mineral saturation index

	Before Gas Injection		**Reactor 1**		**Reactor 2**		**Reactor 3**		**Reactor 4**	
	EX	AM	EX	AM	EX	AM	EX	AM	EX	AM
Quartz	-0.21	-0.16	-0.21	-0.16	-0.21	-0.07	-0.23	-0.01	-0.24	-0.01
Kaolinite	-3.03	-2.87	-3.06	-2.87	-2.82	5.6	-22.55	-23.91	-23.49	-24.85
Microcline	-2.92	-2.51	-2.92	-2.51	-7.02	-1.06	-20.4	-20.86	-21	-21.47
Anhydrite	-1.84	-1.87	-1.84	-1.87	-1.84	-1.87	-1.72	-1.73	-1.73	-1.73
Halite	-0.43	-0.41	-0.43	-0.41	-0.43	-0.41	-0.4	-0.37	-0.4	-0.37
Gypsum	-1.77	-1.71	-1.77	-1.71	-1.78	-1.71	-1.69	-1.55	-1.7	-1.55
Sulphur	-20.3	-19.88	-20.53	-19.14	-7.9	-9.03	4.62	4.86	-87.97	-88.72

Table 4.10b Calculated equilibrium mineral saturation index

	Before Gas Injection		**Reactor 5**		**Reactor 6**		**Reactor 7**	
	EX	AM	EX	AM	EX	AM	EX	AM
Quartz	0	0.35	0	0.34	0	0.42	0	0.43
Kaolinite	-3.13	-0.99	-3.19	2.72	-20.5	-23.27	-21.24	-24.02
Anhydrite	0.03	-0.13	0.02	-0.13	-0.06	-0.08	-0.1	-0.11
Halite	-2.25	-2.2	-2.25	-2.2	-2.23	-2.18	-2.22	-2.17
Gypsum	0.06	0.15	0.04	0.15	-0.06	0.22	-0.1	0.19
Sulphur	-15.62	-11.91	-7.94	-7.86	3.99	4.5	-83.28	-88.77

'Ex' means the results had been simulated under the experimental conditions (35 or 50 °C and 1500 psi). 'Am' means the results had been simulated under the ambient conditions (25 °C and 1 atm). Before injection means the equilibrium calculation was simulated in solid-liquid system only, without the presence of gas.

4.4 Discussion

4.4.1 Effects of CO_2 gas mixture on pH and conductivity

Due to the reactions between the gas mixtures and brine solutions, carbonic acid and sulphuric acid were formed after CO_2 and SO_2 dissolved in the water. The possible reactions are shown in Eq. 18-20.

$$SO_2 + H_2O \leftrightarrow H_2SO_3 \leftrightarrow H^+ + HSO_3^- \leftrightarrow 2H^+ + SO_3^{2-} \quad (19)$$

$$2SO_2 + O_2 + 2H_2O \rightarrow 2H_2SO_4 \rightarrow 2H^+ + SO_4^{2-} \quad (20)$$

The pH of the solid-brine system decreased as more CO_2 and SO_2 dissolved in the water; this trend could be observed in both experimental and modelling results. As shown in Table 4.8, after the solid-brine system of group 12W4 and 7W4 were subjected to pure CO_2, the pH dropped from 6.21 and 6.87 to 5.77 and 5.83, respectively. From the data of modelling results, under the experimental conditions (1500 psi and 35 or 50 °C) of 12W4 and 7W4, the pH changed from initial 6.34 and 6.69 to 3.53 and 3.25, respectively. With the reaction pressure and temperature dropped to test environmental conditions (1atm and 25 °C), the pH increased to 5.14 and 4.57. This difference of pH with the pressure change is related to the fact that the solubility of CO_2 is the function of pressure. When the pressure drops, the chemical equilibrium between the CO_2, H_2O and H_2CO_3, which was shown in Eq. 18, is destroyed and the equilibrium of reaction moves backward from the right to left side. H^+ and CO_3^{2-} then combine to form H_2CO_3 and which dissociates to CO_2 and H_2O. The gas which had been dissolved in the brine solution is released from liquid to gas phase. Therefore, the pH would increase and conductivities of the reactors would decrease.

The pH of the solution from the reactors subjected to the CO_2 mixture containing SO_2 decreased significantly more than that of the reactors subjected to pure CO_2. This difference was indicated in both experimental and simulation results. At ambient conditions, the pH decreased to 0.8-1.85 for the experimental data after the reaction and to 0.045-0.185 for the modelling results. The reason is the sulphuric acid formed by SO_2 and H_2O is strong acid compared with carbonic acid, therefore it could dissociate completely in the water.

In the modelling results, the lowest pH could be found in the reactor containing CO_2, SO_2 and O_2. Comparing the Reactor 3 results with Reactor 4 or Reactor 6 with Reactor 7, the effect of O_2 in the chemical reaction could be evaluated. The SO_2 reacts with water to form H_2SO_3, whose acidity is lower than H_2SO_4. As shown in Eq. 20 and 21, there are two routes for H_2SO_4 formation from SO_2 and H_2O. H_2SO_3, which is the intermediate of these reactions, could be oxidized with the presence of oxidants such as some ions in brine solutions. In the reaction of Reactors 4 and 7, the gas mixture contained O_2 as an impurity. Thus, the SO_3^{2-} could more easily be oxidized to SO_4^{2-} in this case. The pH was therefore lower than the reactors containing CO_2 mixture with SO_2 as the only impurity.

$$SO_3^{2-} + H_2O \leftrightarrow SO_4^{2-} + 2H^+ + 2e^- \quad (21)$$

Comparing the experimental results with modelling results, the trends of pH and conductivity are consistent, but with some gaps for each reactor. For example, the experimental and modelling results of pH and conductivity for Reactor 7 are 3.9, 80700 μmho/cm and 0.078 and 317051 μmho/cm under ambient conditions, respectively. This difference could be explained by the influence of contaminants and the buffer standard used in calibration. As shown in Table 4.8, there were some metal contaminants in the brine solution after the reactions. Figure 4.8 shows the photos of Reactors 4 and 7 taken after the reactions, where the CO_2 mixture contained SO_2 and O_2 and showed the highest concentrations of contaminants were found. The reactions caused some serious corrosion on the reactors. The Teflon coatings were damaged after the reactions. Alloys of reactors were dissolved under the low pH and high pressure, therefore some metals were found in the brine solution in an ionic state. From the XRD results, iron minerals were observed in the solid sample of Reactor 7. Therefore, it appears that Fe was dissolved and involved in the chemical reactions. Some Fe was observed in liquid as ions, the rest was detected in the solid analysis as iron minerals. The oxidation of Fe^{2+} and the formation of iron minerals would influence the pH of the solid-liquid system via Eq. 22-23. With sufficient O_2, the Fe^{2+} would be oxidized completely and as a result reduce the pH of the solution. Both the ferrous and ferric ions would undergo a secondary formation of iron minerals and the acidity stored in a solid form (Nordstrom et al., 2000). According to the analyses of solids and liquids from Reactor 7, the amounts of iron carbonate hydroxide hydrate and siderite were limited and the concentration of Fe detected in liquid was high. Thus, the chemical reaction shown in Eq. 22 is dominant and the pH increased because of this contaminant. In simulation work, the corrosion problem was not included and the ideal pH decreased to the equilibrium based on the calculation. Furthermore, the calibration work of pH and conductivity must be done before the test. An appropriate buffer standard is important for linear measurement of these physical parameters. Due to the limitation of the buffer standards, the results would contain some errors. For Reactor 4, which contained CO_2 mixture with SO_2 and O_2 in group 12W4, the pH dropped to -0.078. The possibility of negative pH has been proved in some articles (Nordstrom et al., 2000).

$$Fe^{2+} + \frac{1}{4}O_2 + H^+ \rightarrow Fe^{3+} + \frac{1}{2}H_2O \qquad (22)$$

$$2Fe^{2+} + Fe^{3+} + \frac{1}{2}CO_3^{2-} + 7.45H_2O \rightarrow Fe_2^{II}Fe^{III}(H)_6(CO_3)_{0.5}(H_2O)_{1.45} + 6H^+ \quad (23)$$

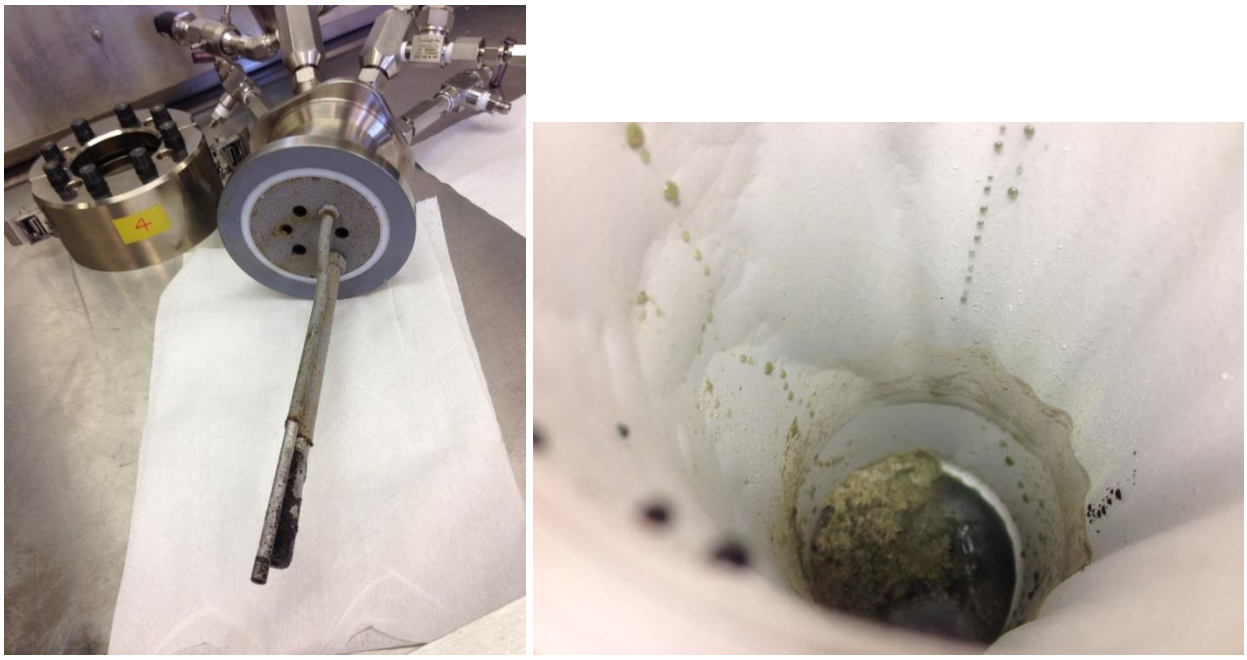

(A)

(B)

Figure 4.8 The corrosions of Reactors 4 and 7 after reaction.

Reactor (A) are two pictures of Reactor 4 and (B) are two pictures Reactor7.

4.4.2 Chemical reactions of rock minerals

During the 45 day batch reactions, almost all the mineral phases were involved in the chemical reactions, even though some minerals did not show obvious changes before and after the reactions. The possible chemical reactions between the gas mixtures, water and rock minerals are listed in Table 4.11. Quartz would be as a form of SiO_2 (aq) in the water, which would partially dissociate Si^{4+}. According to the previous studies (Soong et al., 2013; Renard et al., 2011), the acidity is a driven force in the chemical equilibrium between the quartz and water, and pushes this reaction proceed from left to right. Therefore, the amount of quartz decreased with the acidity increased. As shown in Figures 4.4 and 4.5, due to the formation of sulphuric acid, notable dissolution of quartz could be observed in the solids reacted with a gas mixture containing SO_2. However, as discussed above, the pH was higher than ideal in Reactor 7 due to the presence of Fe; the amount of quartz was slightly higher than that of Reactor 6. Microcline was one of the original components in group 12W4. This mineral would be dissolved under the acidic conditions and form Al^{3+}, K^+ and H_4SiO_4. From the XRD results, the amount of microcline was almost unchanged in the control reactor filled with N_2. However, it was undetectable in the solid samples from Reactors 2, 3 and 4, which were subjected to either pure CO_2 or CO_2 mixture. Even though the acidity of carbonic acid is lower than that of sulphuric acid, the microcline still dissolved completely. Anhydrite appeared in group 12W4, both as a component in the original solid sample, and formed by precipitation from ionic Ca^{2+} and SO_4^{2-} in the solutions. In Reactors 2 and 5, which were reacted with pure CO_2, the formation of $CaSO_4$ was only from ions in the initial solutions. With the presence of SO_2, the concentration of SO_4^{2-} in the solution increased drastically and this high concentration enhanced the formation of anhydrite. Therefore, the highest amount of anhydrite formation was observed in the reactors which were reacted with SO_2. However, Reactor 7 in group 7W4 showed a different trend compared with Reactor 4 in group 12W4, which were both subjected to mixture CO_2+SO_2+O_2. This appearance could be explained by the higher concentration of Fe caused by the contaminants. At 50 °C, the solubility of $CaSO_4$ decreased with the increasing of the concentration Fe at range from 0-0.5 mol/kg (Li and Demopoulos, 2006). From the liquid ion analysis, the concentration of Fe was 20,000 mg/L (0.36 mol/L) in Reactor 7 which would be enhance the dissolution of anhydrite (gypsum). The amount of anhydrite in the solid from Reactor 7 was therefore lower than Reactor 6. Halite was crystalized after reactions and its concentration increased

with the increasing acidity in both groups 12W4 and 7W4. The crystallization of NaCl would result from the high concentration of Na^+ and Cl^-. As for the experimental and modelling results shown in Tables 4.8 and 4.9, the concentrations of Na^+ and Cl^- were almost the same before and after reactions, suggesting that the Na^+ and Cl^- from the initial brine solution were not involved in the batch reactions and the dissolution equilibrium had not been changed. With the increasing acidity, the dissolution of minerals increased and Na^+ was released from the solid to the liquid in ionic state. As for the SEM results, after the solution became saturated with Na^+, excess Na^+ began to crystalize on the surface of the solids, thereby maintaining the solubility equilibrium. Thus, the amount of halite increased with the increasing acidity after the reactions. Kaolinite showed different results between 12W4 and 7W4. With the presence of acid gas SO_2, this mineral was completely dissolved in group 12W4, which indicates that the high acidity would influence significantly on the dissolution of kaolinite. However, the amounts of this mineral remained unchanged after the reactions in group 7W4. Thus, the acid gas showed a higher influence on 12W4 than 7W4. Dobassite showed the same amount of dissolution in each reactor and it therefore did not appear to be affected by the pH and concentrations of other ions. The hydrolysis reaction was the only possible reaction occurring in this mineral.

Table 4.11 The possible reactions of rock minerals

Mineral Phase	Chemical Compound	Chemical Reaction	Source
Quartz	SiO_2	Quartz → SiO_2 (aq)	Bea et al., 2013
Kaolinite	$Al_2Si_2O_5(OH)_4$	Kaolinite + $6H^+$ → H_2O + $2H_4SiO_4$ + $2Al^{3+}$	Gunter et al., 2000
Anhydrite	$CaSO_4$	Anhydrite → Ca^{2+} + SO_4^{2-}	
Microcline	$K(AlSi_3O_8)$	Microcline + $4H_2O$ + $4H^+$ → Al^{3+} + K^+ + $3H_4SiO_4$	Li et al., 2014
Calcite	$CaCO_3$	Calcite → Ca^{2+} + CO_3^{2-}	
		Calcite + SO_2 + $1/2O_2$ → Anhydrite + CO_2	
Gypsum	$CaSO_4 \cdot 2H_2O$	Gypsum → Anhydrite + $2H_2O$	
Sulphur	S	$4SO_2$ + $4H_2O$ → $3H_2SO_4$ + H_2S	Wang et al., 2011a
		$2H_2S$ + SO_2 → $3S$ + $2H_2O$	

4.4.3 Ion analyses

The highest concentration of total carbon could be observed in Reactors 2 and 5, which were subjected to pure CO_2. As shown in Eq. 18, the chemical equilibrium between the CO_2

molecules and CO_3^{2-} should remain a same constant at a certain pressure. With the formation of sulphuric acid by SO_2, this equilibrium of CO_2 dissolution changes via the chemical reaction shown in Eq. 24. Therefore, the concentration of total carbon decreased with the acidity increased.

$$CO_3^{2-} + 2H^+ \rightarrow CO_2 + H_2O \qquad (24)$$

With the presence of SO_2 in the gas mixture, the dissolved SO_2 gas molecules formed SO_4^{2-} via Eq. 19 - 21 and its concentration was therefore at a higher level in Reactors 3, 4, 6 and 7. As shown in Eq. 20, the formation of SO_4^{2-} would be accelerated under the oxidizability of O_2. Thus, the highest increase of the concentration of SO_4^{2-} could be detected in the solids subjected to CO_2 mixture containing both SO_2 and O_2. Under these circumstances, the concentration of Ca^{2+} decreases by the formation of $CaSO_4$ (gypsum or anhydrite) and its reduction increases as the concentration of SO_4^{2-} increased. As shown in Table 4.3, the mineral samples in both 12W4 and 7W4 were initially mostly quartz (>90%), which gradually decreased in weight percentage as the acidity increased. By comparing the different mineral phases in the solid samples, the element Si came from many sources including quartz, sodalite group, kaolinite, microcline and dobassite. Therefore, element analysis-XRF was used to quantify the concentration change of Si in the solid after the reaction. As discussed above, the weight percentage of Si gradually decreased from the initial 94.70% to lowest 70.20% of Reactor 4 in group 12W4 and from the initial 97.90% to lowest 92.30% of Reactor 7 in group 7W4. The amount of reduction of Si was dissolved in the brine as SiO_2 (aq) after reaction. According to the dissolution of quartz discussed above, the concentrations of Si should increase. This is consistent to the ion analyses and modelling results (Tables 4.8 and 4.9). Ionic Al^{3+} was more detectable in Reactors 3 and 4 compared with other reactors. Because the dissolution of minerals contained element aluminum such as microcline and dobassite, the Al would emerge in solution as ion state under the reactions with acids. However, because the percentage of Al minerals in group 12W4 was higher than that in group 7W4, the concentration of Al^{3+} in group 12W4 therefore slightly higher than that in group 7W4.

Other ions such as Na^+, Cl^- and Mg^{2+} may be not involved in the chemical reactions and their concentrations did not show an obvious difference before and after reactions. The minor difference of the concentrations could have been caused by the crystallization process.

Finally, the total dissolution of minerals was evaluated using TDS of different reactors. In the presence of acid gas, strong acid forms and increases the dissolution of rock minerals. After 45 day batch reactions, the increases in the concentration of main chemical species were therefore observed in the reactors containing CO_2 mixed with SO_2. As discussed in the introduction, the dissolution of rock minerals could be enhanced in the presence of oxygen (Jung et al., 2013). The highest TDS were detected in Reactors 4 and 7, which were subjected to gas mixture contained O_2, even though the pH were relatively higher than the reactor containing CO_2+SO_2. Both experimental and modelling results showed the same trend of TDS successively increasing from Reactors 2 to 4 in group 12W4 and from Reactors 5 to 7 in group 7W4. Therefore, the dissolution was enhanced by the lower pH and the presence of oxygen.

4.4.4 Saturation equilibrium of minerals

The saturation index (SI) is always used for the prediction of solid equilibrium in the water system. As shown in Eq. 25, it is a ratio between the ion activity products (IAP) and K equilibrium constant (K_{sp}).

$$SI \equiv \log\left(\frac{IAP}{Ksp}\right) \qquad (25)$$

If IAP=K_{sp}, SI=0, the water is saturated with the mineral. If IAP<K_{sp}, SI<0, water is undersaturated with the mineral and the reaction is proceeding to the direction of dissolution. If IAP>K_{sp}, SI>0, water is supersaturated with the mineral and the reaction is proceeding to the direction of precipitation.

Due to the high acidity, the dissolution of minerals was enhanced. As discussed above in the XRD results, the minerals kaolinite and microcline were influenced by acidity significantly and the trend was also be detected in Table 4.10. The saturation index of these two minerals dropped from ~-3 to ~-20. Rather, the saturation indexes were almost unchanged with impurities involved because of the stability of quartz in acids.

In general, the saturation index decreased with the decreasing of pH, which indicates the porosity would be increased correspondingly.

4.4.5 The quantification of porosity change

According to the definition, the porosity is the fraction of the volume of voids over the total volume. Here, the storage sites were considered as mineral solids with a certain volume of pores. In the case of CO_2 storage of the saline aquifer, the total volume of the pores and minerals was assumed to be constant, which was only a function of geological structure and conditions. Therefore, Eq. 26 and 27 could be used to quantify the porosity.

$$\emptyset = \frac{V_{pore}}{V_{total}} \quad (26)$$

$$V_{total} = V_{mineral} + V_{pores} \quad (27)$$

where Φ denotes the porosity of the rock minerals, $V_{mineral}$ and V_{pores} denote the volumes of mineral phase and pores, respectively. V_{total} is the total volume of the rock minerals with the pores. As discussed above, the different mineral phases were detected by XRD analysis method. Thus, the volume of overall mineral phases in the saline aquifer could be described as the sum of the volume of each mineral phase. Furthermore, the volume of each mineral phase could be calculated by the quotient of the mass to the density. An alternative expression of $V_{mineral}$ is therefore shown in Eq. 28.

$$V_{mineral} = \frac{m_1}{\rho_1} + \frac{m_2}{\rho_2} + \frac{m_3}{\rho_3} + \cdots = \frac{am}{\rho_1} + \frac{bm}{\rho_2} + \frac{cm}{\rho_3} + \cdots \quad (28)$$

where m_n and ρ_n denote the mass and the density of a kind of mineral phase, *a (b, c…)* denotes the mass fraction of a mineral phase in the total mass (m). Combine the Eq. 26, 27 and 28, V_{total} could be expressed by the variables *a, m,* ρ and Φ.

$$V_{total} = \frac{\frac{am}{\rho_1} + \frac{bm}{\rho_2} + \frac{cm}{\rho_3} + \cdots}{1 - \emptyset} \quad (29)$$

After the chemical reactions between the CO_2 gas mixture and aquifer water and minerals, the porosity would change due to the precipitation or dissolution. Same as above, the porosity after reaction could be also described by *a, m, ρ* and *Φ*.

$$\emptyset' = \frac{V'_{pore}}{V_{total}} = \frac{V_{total} - V'_{mineral}}{V_{total}} = 1 - \frac{\frac{a'm'}{\rho_1} + \frac{b'm'}{\rho_2} + \frac{c'm'}{\rho_3} + \cdots}{V_{total}} \quad (30)$$

where *Φ', V'pore* and *V'mineral* are the porosity and the volume of the pores and mineral phases after the reactions, respectively. *a' (b', c'...)* denotes the mass fraction of a mineral phase in the total mass (*m'*) after the reactions. Eq. 31 is the combination of Eq. 29 and 30, *Φ'* could be therefore calculated.

$$\emptyset' = 1 - \frac{\frac{a'm'}{\rho_1} + \frac{b'm'}{\rho_2} + \frac{c'm'}{\rho_3} + \cdots}{\frac{\frac{am}{\rho_1} + \frac{bm}{\rho_2} + \frac{cm}{\rho_3} + \cdots}{1 - \emptyset}} = 1 - \frac{\frac{a'}{\rho_1} + \frac{b'}{\rho_2} + \frac{c'}{\rho_3} + \cdots}{\frac{\frac{a}{\rho_1} + \frac{b}{\rho_2} + \frac{c}{\rho_3} + \cdots}{1 - \emptyset}} \times \frac{m'}{m} \quad (31)$$

In this experiment, the mass balance was considered as the sum of the solids and liquids. The process of dissolution increases the porosity of the system and produces increased TDS, while precipitation of solid minerals decreases the porosity by coating the pores and results in decreased TDS. Therefore, the difference of TDS before and after the reactions could be used to quantify the mass difference of the solid sample.

Based on this calculation method and the analyses results shown above, the porosity was calculated and the results were shown in Table 4.12. Due to the high concentration of NaCl in each group, and its high solubility in the water, the mineral halite could be ignored in the calculation of porosity. In Reactors 2 and 5, the dissolution was dominant due to the acidity of carbonic acid. Therefore, the porosity increased after the reaction. With the impurity SO_2 in Reactors 3 and 6, the precipitation of $CaSO_4$ would occur and block the pores. However, the dissolution would still be dominant due to the high acidity of sulphuric acid formed by SO_2 and water. The porosity was therefore increased in relatively slow rate. As discussed above, the acidity would increase with the presence of O_2 and the porosity in Reactors 4 and 7 would therefore be influenced significantly.

Table 4.12 The porosity change after the reactions

		ΔTDS (g/L)	**Porosity**
10-11-061-12W4	Initial	---	0.147
	Reactor 1	-6.76	0.085
	Reactor 2	-0.007	0.132
	Reactor 3	1.356	0.125
	Reactor 4	5.367	0.136
06-29-007-07W4	Initial	---	0.141
	Reactor 5	9.641	0.223
	Reactor 6	10.833	0.224
	Reactor 7	12	0.266

However, the 45-days experiments did not achieve the saturation equilibrium of all the minerals. As shown in Table 4.10, the saturation index indicated most minerals were under saturated. A number of studies (Humez et al., 2014; Gunter et al., 2000; Beni and Clauser, 2014; Mito et al., 2013; Jung et al., 2013; Knauss et al., 2005; Wigand et al., 2008; Wilkin and Digiulio, 2010; Xu et al., 2007; Wilke et al., 2012; Xiao et al., 2009) developed kinetic models for simulating the change of dissolution and precipitation with time. The results indicated the geochemical reaction would take a long time (even though different minerals have different kinetic factors) to achieve the equilibrium. This acceptable considering that the process of CCS is dynamic and the geochemical reaction would be continuous over long time. The present investigation only observed the reactions over the short-term and the results could be used for the prediction of the geochemical changes in the initial period of CO_2 injection. According to the saturation index shown in Table 4.10, the interaction between rock minerals, brine and CO_2 gas mixture is expected to proceed over a long period. Therefore, the absolute value of ΔTDS in Table 4.12 would increase and mass ratio of the products to the reactants would increase too. As a result, the change of porosity would be more significant.

4.4.6 The corrosion on the pipeline material

The pipeline transportation is a connection between the CO_2 sources and storage site. To ensure the safety of the CCS operation and minimize the risk of leakage, the corrosive behaviour of the fluid on the pipeline material must be understood. The effect of CO_2 leakage is not only a higher concentration of atmospheric CO_2, but also a reduced concentration of O_2. The high concentration of CO_2 would have harmful effects on the behaviour and health of human beings and animals. 1% concentration causes drowsiness and 1.5% is the maximum permissible concentration. Concentrations exceeding 2% can cause narcosis and increase cardiovascular load. At ranges between 3% and 5%, respiration can be inhibited and blood pressure and pulse increase significantly. Concentrations higher than 10% can cause mental confusion and hearing loss. Concentrations exceeding 20% are immediately leathal (Witkowski et al., 2013). Therefore, a number of studies evaluated the effect of different factors on the transportation materials corrosion and the safety risk of CCS.

Both case studies and experimental research indicate that the corrosion rate during transport of pure CO_2 could be neglected when the water content is well below the solubility limit and the corrosion rates were less than 0.02 mils per year (Dugstad et al., 2011; Schremp and Roberson, 1975). However, the corrosion occurred at very low water content (200 ppm) with contamination by acids gases. As discussed above, SO_2 would form sulphuric acid with the presence of water. To minimize the potential corrosion, a dehydration process must be conducted before the CO_2 injection. This effect of water on the corrosion behaviour of pipeline materials was also evaluated by experiments in previous studies (Choi and Nešic, 2011b; Bosch et al., 2013).

Additionally, the redox reaction between two reactants with different reduction potential would be a possible factor in the corrosion. For instance, Eq. 32-33 shows a potential case of corrosion in the transportation process. Fe, which is a main element in the pipeline material, transfers two electrons to SO_2 and O_2 for the reduction. Fe is therefore corroded.

$$SO_2 + O_2 + 2e^- \rightarrow SO_4^{2-} \qquad (32)$$

$$Fe \rightarrow Fe^{2+} + 2e^- \qquad (33)$$

SO_2 and O_2 are involved in the corrosion reaction as cathode and the corrosion rate would increase as their concentration increased. Xiang et al. (2013b) developed a mechanistic model to predict the corrosion rate in supercritical $CO_2/O_2/SO_2/H_2O$ system and then verified by the experimental results in the literature. As shown in Figure 4.9, the study indicates the corrosion rate increased as the concentration of SO_2 increased in the gas mixture. To figure out the effect of O_2 on the corrosion behaviour, Dugstad et al. (2011) proved the presence of O_2 would accelerate the corrosion process by experimental test, and the calculation results by Xiang et al. (2013b) showed a similar trend, which is shown in Figure 4.10. If the corrosion reactions are unavoidable, the physical conditions such as temperature and pressure would be the crucial parameters in control the corrosion rate. Xiang et al. (2013a) evaluated the effect of temperature on corrosion of X70 steel in $CO_2/SO_2/O_2/H_2O$ system. Figure 4.11 shows their experimental results of this study and the predicted value. The results suggest that the corrosion rate increased with temperature until it reached a peak value and then declined. Additionally, the pressure is a main factor in the effects of chemical equilibrium. In the case of corrosion by $CO_2/SO_2/O_2$, the high pressure would "push" the chemical reaction to move forward and form sulphuric acid and carbonic acid. The concentration of H^+ is therefore enhanced and the corrosion rate is correspondingly increased. Finally, pressure would cause the solubility of SO_2 to change and affect the reaction rate. For instance, Choi and Nešic (2011a) studied the relationship between the pressure and corrosion rate and the results showed that the corrosion rate in supercritical CO_2 increased when the pressure is increased from 6 MPa to 8 MPa.

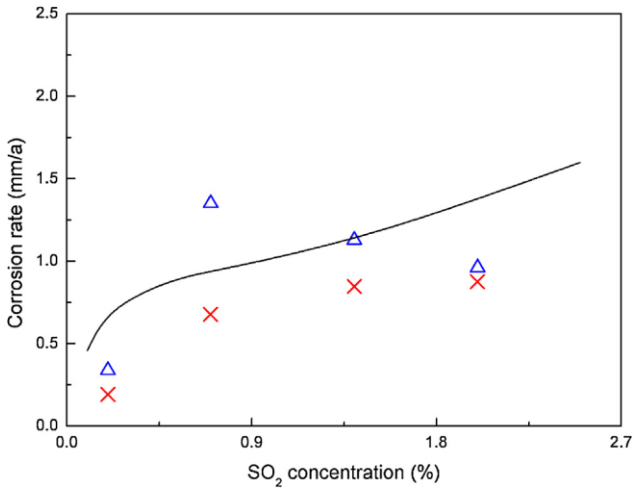

Figure 4.9 Predicted corrosion rates and experimental results with the variation of SO_2 concentration (— Predicted value (Xiang et al., 2013b); Δ Measured value of iron sample (Xiang et al., 2011); × Measured value of X70 steel sample (Xiang et al., 2011)).

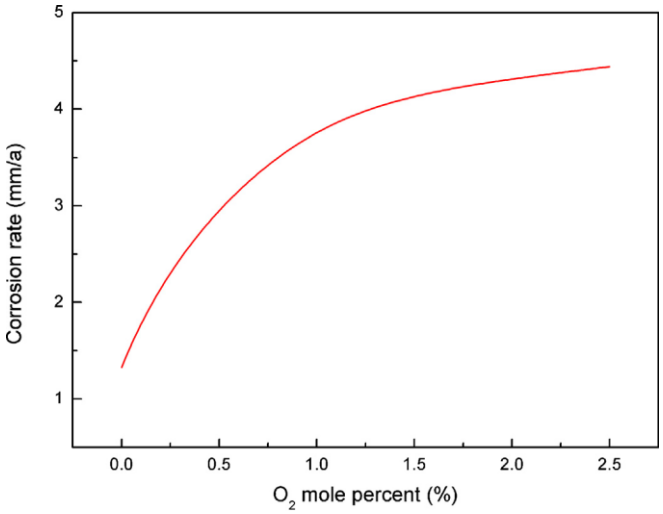

Figure 4.10 Predicted variation of corrosion rate with O_2 mole fraction (323.15 K, 10 MPa, 2.0% SO_2, 0–2.5% O_2, 100% RH, 120 rpm, 120 h) (Xiang et al., 2013b).

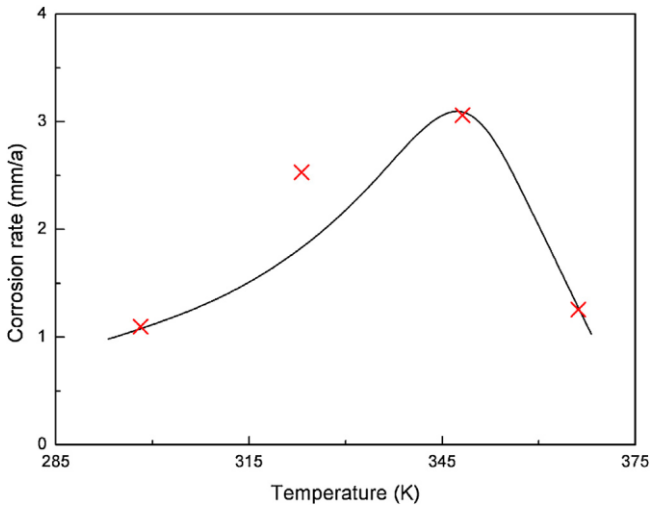

Figure 4.11 Measured corrosion rates and predicted results with the variation of temperature (— predicted value (Xiang et al., 2013b); × measured value (Xiang et al., 2013a)).

In accordance with the potential corrosion of the pipeline materials, various studies were carried out to find solutions and enhance the safety of CCS. Rules for selection of the suitable pipeline materials were proposed (Demofonti et al., 2013; Huizinga et al., 2013; Ropital, 2008). Coating the pipeline is a method to improve the corrosion resistance of the materials. For instance, polymer coating showed a good performance of corrosion resistance (Zhang et al., 2013).

4.5 Conclusion

The effects of SO_2 and O_2 on CO_2 geological storage were studied through theoretical simulation and experimental tests in this work.

(1) Effects on aqueous system: compared with results of pure CO_2, the CO_2 stream with SO_2 reduced the pH of water system significantly. In the presence of O_2, the acidity increased and the reactions were more significant. TDS of the water system increased with the impurities involved, which suggests that the dissolution was dominant.

(2) Effects on rock minerals: the rock minerals of 12W4 and 7W4 are both quartz dominant. The dissolution of quartz increased significantly with the presence of SO_2 and O_2. Kaolinite in 7W4 dissolved completely after the reaction with CO_2 mixture with SO_2. On the other hand, kaolinite in 12W4 remained unchanged. Dobassite did

not show any change with the inclusion of SO_2 and O_2. Microline, which is a species only detected in group 12W4, reacted completely except in the baseline case where CO_2 was not introduced. In addition to the dissolution, anhydrite and sulphur both formed due to the presence of SO_2. However, O_2 affected the stability of these two minerals and caused them to dissolve in water.

(3) Effects on porosity: the calculated results showed that the effects of the impurities on porosity of 12W4 and 7W4 were different. Porosity of 12W4 decreased after the reactions with both CO_2 and CO_2 mixtures. On the other hand, the porosity increased in group 7W4, which suggests that dissolution was dominant in the system.

(4) Comparing the results of 12W4 and 7W4, 7W4 would be more suitable for impure CO_2 storage.

(5) Effects on pipeline: the acid gases would cause serious corrosion on pipeline materials. Therefore, corrosion-resistant materials or coating are required in pipeline transport of CO_2.

4.6 References

1. André, L., P. Audigane, M. Azaroual, and A. Menjoz. 2007. "Numerical Modeling of Fluid-Rock Chemical Interactions at the Supercritical CO2-Liquid Interface during CO2 Injection into a Carbonate Reservoir, the Dogger Aquifer (Paris Basin, France)." Energy Conversion and Management 48 (6): 1782-1797.

2. Bachu, S. et al. 2005. Deep Injection of Acid Gas in Western Canada. Developments in Water Science. Vol. 52.

3. Bachu, S., T. Hauck, et al. (2011). "The Basal Aquifer in the Prairie Region of Canada: Characterization for CO2 Storage - Report of Findings During Stage I (Phases 1 and 2)". Edmonton, AB, Alberta Innovates - Technology Futures.

4. Bacon, D. H., B. M. Sass, M. Bhargava, J. Sminchak, and N. Gupta. 2009. "Reactive Transport Modeling of CO2 and SO2 Injection into Deep Saline Formations and their Effect on the Hydraulic Properties of Host Rocks.".

5. Bea, S. A., H. Wainwright, N. Spycher, B. Faybishenko, S. S. Hubbard, and M. E. Denham. 2013. "Identifying Key Controls on the Behavior of an Acidic-U(VI) Plume in the Savannah River Site using Reactive Transport Modeling." Journal of Contaminant Hydrology 151: 34-54.

6. Beni, A. N. and C. Clauser. 2014. "The Influence of Temperature on Chemical Fluid-Rock Reactions in Geological CO2 Sequestration." Environmental Modeling and Assessment 19 (4): 315-324.

7. Bosch, C., S. Jäger, H. Brauer, E. Fleury, M. Meyer, C. Kassel, and T. Schmidt. 2013. "Corrosion of Linepipe Material in Different CCS-CO2-Atmospheres.".

8. Choi, Y. -S and S. Nešic. 2011a. "Determining the Corrosive Potential of CO2 Transport Pipeline in High pCO2-Water Environments." International Journal of Greenhouse Gas Control 5 (4): 788-797.

9. ———. 2011b. Effect of Water Content on the Corrosion Behavior of Carbon Steel in Supercritical CO2 Phase with Impurities. NACE - International Corrosion Conference Series.

10. Crandell, L. E., B. R. Ellis, and C. A. Peters. 2010. "Dissolution Potential of SO2 Co-Injected with CO2 in Geologic Sequestration." Environmental Science and Technology 44 (1): 349-355.

11. Demofonti, G., M. D. Biagio, A. Fonzo, A. Lucci, and C. M. Spinelli. 2013. "Definition of Requirements for Safe and Reliable Co2 Transportation Network through an Integrated Laboratory, Computer Modelling and Full Scale Methodology.".

12. Dugstad, Arne, Bjørn Morland, and Sigmund Clausen. 2011. "Corrosion of Transport Pipelines for CO2–Effect of Water Ingress." Energy Procedia 4 (0): 3063-3070.

13. Ellis, B. R., L. E. Crandell, and C. A. Peters. 2010. "Limitations for Brine Acidification due to SO2 Co-Injection in Geologic Carbon Sequestration." International Journal of Greenhouse Gas Control 4 (3): 575-582.

14. Gunter, W. D., S. Bachu, D. H. -S Law, V. Marwaha, D. L. Drysdale, D. E. Macdonald, and T. J. McCann. 1996. "Technical and Economic Feasibility of CO2 Disposal in Aquifers within the Alberta Sedimentary Basin, Canada." Energy Conversion and Management 37 (6-8): 1135-1142.

15. Gunter, W. D., E. H. Perkins, and I. Hutcheon. 2000. "Aquifer Disposal of Acid Gases: Modelling of Water-Rock Reactions for Trapping of Acid Wastes." Applied Geochemistry 15 (8): 1085-1095.

16. Huizinga, S. et al. 2013. Materials Selection and Corrosion Control for a CO2 Transport and Injection System. NACE - International Corrosion Conference Series.

17. Humez, P., P. Négrel, V. Lagneau, J. Lions, W. Kloppmann, F. Gal, R. Millot, et al. 2014. "CO2-Water-Mineral Reactions during CO2 Leakage: Geochemical and Isotopic Monitoring of a CO2 Injection Field Test." Chemical Geology 368: 11-30.

18. Jacquemet, N., Y. Le Gallo, A. Estublier, V. Lachet, I. von Dalwigk, J. Yan, M. Azaroual, and P. Audigane. 2009. "CO2 Streams Containing Associated Components-A Review of the Thermodynamic and Geochemical Properties and Assessment of some Reactive Transport Codes.".

19. Ji, X. and C. Zhu. 2013. "Predicting Possible Effects of H2S Impurity on CO2 Transportation and Geological Storage." Environmental Science and Technology 47 (1): 55-62.

20. Jung, H. B., W. Um, and K. J. Cantrell. 2013. "Effect of Oxygen Co-Injected with Carbon Dioxide on Gothic Shale Caprock-CO2-Brine Interaction during Geologic Carbon Sequestration." Chemical Geology 354: 1-14.

21. Kharaka, Y. K., D. R. Cole, S. D. Hovorka, W. D. Gunter, K. G. Knauss, and B. M. Freifeld. 2006. "Gas-Water-Rock Interactions in Frio Formation Following CO2 Injection: Implications for the Storage of Greenhouse Gases in Sedimentary Basins." Geology 34 (7): 577-580.

22. Knauss, K. G., J. W. Johnson, and C. I. Steefel. 2005. "Evaluation of the Impact of CO2, Co-Contaminant Gas, Aqueous Fluid and Reservoir Rock Interactions on the Geologic Sequestration of CO2." Chemical Geology 217 (3-4 SPEC. ISS.): 339-350.

23. Koenen, M., T. J. Tambach, and F. P. Neele. 2011. "Geochemical Effects of Impurities in CO2 on a Sandstone Reservoir.".

24. Li, D., S. Bauer, K. Benisch, B. Graupner, and C. Beyer. 2014. "OpenGeoSys-ChemApp: A Coupled Simulator for Reactive Transport in Multiphase Systems and Application to CO2 Storage Formation in Northern Germany." Acta Geotechnica 9 (1): 67-79.

25. Li, Q., X. Li, N. Wei, and Z. Fang. 2011. "Possibilities and Potentials of Geological Co-Storage CO2 and SO2 in China.".

26. Li, Z. and G. P. Demopoulos. 2006. "Effect of NaCl, MgCl2, FeCl2, FeCl3, and AlCl3 on Solubility of CaSO4 Phases in Aqueous HCl Or HCl + CaCl2 Solutions at 298 to 353 K." Journal of Chemical and Engineering Data 51 (2): 569-576.

27. Mito, S., Z. Xue, and T. Sato. 2013. "Effect of Formation Water Composition on Predicting CO2 Behavior: A Case Study at the Nagaoka Post-Injection Monitoring Site." Applied Geochemistry 30: 33-40.

28. Nohra, M., T. K. Woo, S. Alavi, and J. A. Ripmeester. 2012. "Molecular Dynamics Gibbs Free Energy Calculations for CO2 Capture and Storage in Structure i Clathrate Hydrates in the Presence of SO 2, CH4, N2, and H2S Impurities." Journal of Chemical Thermodynamics 44 (1): 5-12.

29. Nordstrom, D. K., C. N. Alpers, C. J. Ptacek, and D. W. Blowes. 2000. "Negative pH and Extremely Acidic Mine Waters from Iron Mountain, California." Environmental Science and Technology 34 (2): 254-258.

30. Pruess, K. and J. García. 2002. "Multiphase Flow Dynamics during CO2 Disposal into Saline Aquifers." Environmental Geology 42 (2-3): 282-295.

31. Renard, S. et al. 2011. Impact of SO2 and NO on Carbonated Rocks Submitted to a Geological Storage of CO2: An Experimental Study. Carbon Dioxide Sequestration and Related Technologies.

32. Ropital, F. 2008. "Greenhouse Gas Limitation: Corrosion and Materials Challenges for the Capture and Storage of Carbon Dioxide.".

33. Schremp, F. W. and G. R. Roberson. 1975. "EFFECT OF SUPERCRITICAL CARBON DIOXIDE (CO//2) ON CONSTRUCTION MATERIALS." Soc Pet Eng AIME J 15 (3): 227-233.

34. Soong, Y., S. W. Hedges, B. H. Howard, R. M. Dilmore, and D. E. Allen. 2013. "Effect of Contaminants from Flue Gas on CO2 Sequestration in Saline Formation." International Journal of Energy Research.

35. Wang, J., Ryan, D., Anthony, E.J., Wigston, A., 2011a. "Effects of impurities on geological storage of carbon dioxide". IEA GHG Report 2011/04.

36. Wigand, M., J. W. Carey, H. Schütt, E. Spangenberg, and J. Erzinger. 2008. "Geochemical Effects of CO2 Sequestration in Sandstones Under Simulated in Situ Conditions of Deep Saline Aquifers." Applied Geochemistry 23 (9): 2735-2745.

37. Wilke, F. D. H., M. Vásquez, T. Wiersberg, R. Naumann, and J. Erzinger. 2012. "On the Interaction of Pure and Impure Supercritical CO 2 with Rock Forming Minerals in Saline Aquifers: An Experimental Geochemical Approach." Applied Geochemistry 27 (8): 1615-1622.

38. Wilkin, R. T. and D. C. Digiulio. 2010. "Geochemical Impacts to Groundwater from Geologic Carbon Sequestration: Controls on pH and Inorganic Carbon Concentrations from Reaction Path and Kinetic Modeling." Environmental Science and Technology 44 (12): 4821-4827.

39. Witkowski, A., A. Rusin, M. Majkut, S. Rulik, and K. Stolecka. 2013. "Comprehensive Analysis of Pipeline Transportation Systems for CO 2 Sequestration. Thermodynamics and Safety Problems." Energy Conversion and Management 76: 665-673.

40. Xiang, Y., Z. Wang, Z. Li, and W. D. Ni. 2013a. "Effect of Temperature on Corrosion Behaviour of X70 Steel in High Pressure CO2/SO2/O2/H2O Environments." Corrosion Engineering Science and Technology 48 (2): 121-129.

41. Xiang, Y., Z. Wang, M. Xu, Z. Li, and W. Ni. 2013b. "A Mechanistic Model for Pipeline Steel Corrosion in Supercritical CO 2-SO2-O2-H2O Environments." Journal of Supercritical Fluids 82: 1-12.

42. Xiang, Yong, Zhe Wang, Chao Xu, Chengchuan Zhou, Zheng Li, and Weidou Ni. 2011. "Impact of SO2 Concentration on the Corrosion Rate of X70 Steel and Iron in Water-Saturated Supercritical CO2 Mixed with SO2." The Journal of Supercritical Fluids 58 (2): 286-294.

43. Xiao, Y., T. Xu, and K. Pruess. 2009. "The Effects of Gas-Fluid-Rock Interactions on CO2 Injection and Storage: Insights from Reactive Transport Modeling.".

44. Xu, T., J. A. Apps, K. Pruess, and H. Yamamoto. 2007. "Numerical Modeling of Injection and Mineral Trapping of CO2 with H2S and SO2 in a Sandstone Formation." Chemical Geology 242 (3-4): 319-346.

45. Zhang, X., J. F. Zevenbergen, M. P. N. Spruijt, and M. Borys. 2013. "Corrosion of Pipe Steel in CO2 Containing Impurities and Possible Solutions.".

Chapter 5

Conclusion

The effects of impurities containing in CO_2 stream on the physical and chemical properties of the CO_2 stream itself and the aquifer systems were studied through theoretical simulation and experimental methods.

Physical effects of impurities include storage capacity, buoyancy and phase behaviour. In the presence of non-condensable impurities, the density decreased; the most significant reduction was found at each temperature. The CO_2 storage capacity was normalized according to these density changes. The results showed that the storage capacity decreased significantly at a certain temperature and pressure. In order to simulate the migration of CO_2 underground, the change in CO_2 buoyancy was quantified. Results indicated that non-condensable impurities such as N_2, O_2 and Ar could cause a significant change of buoyancy in the saline aquifer. Finally, the phase behaviours were simulated to determine the operation conditions. To avoid phase split, higher pressures and lower temperatures are required in CO_2 transportation when these impurities were included in CO_2 steam.

The chemical effects of impurities include the chemical properties of the aqueous system, rock integrity and pipeline safety. Compared to pure CO_2, the pH of aquifer water was reduced significantly in the presence of SO_2. Due to the high acidity, the rate of dissolution of rock minerals such as quartz increased significantly. Results of liquid analysis and solid characterization illustrate that dissolution and precipitation are the two primary effects on the reservoir rock, which may further affect the porosity of rocks in the aquifer system for CO_2 storage. The two samples studied in this article showed two different trends. The porosity increased in 7W4 but decreased in 12W4 with SO_2 present. On the other hand, acidic gases, mainly SO_2, existed in the gas phase would cause serious corrosion on pipeline materials. Therefore, corrosion-resistant materials or coating are required in pipeline transport of CO_2.

Appendix A

Table A.1 Properties of Pure Species

Component	W_m	ω	T_c (K)	P_c (bar)	Z_c
CO_2	44.010	0.224	304.2	73.83	0.274
O_2	31.999	0.022	154.6	50.43	0.288
N_2	28.014	0.038	126.2	34.00	0.289
Ar	39.948	0.000	150.9	48.98	0.291
SO_2	64.065	0.245	430.8	78.84	0.269
SO_3	80.064	0.424	490.9	82.10	0.255
NO	30.066	0.583	180.2	64.80	0.251
NO_2	46.005	0.851	431.2	101.32	0.233
H_2S	34.082	0.094	373.5	89.63	0.284
CO	28.010	0.048	132.9	34.99	0.299
H_2	2.016	-0.216	33.19	13.13	0.305
CH_4	16.043	0.012	190.6	45.99	0.286
H_2O	18.015	0.345	647.1	220.55	0.229

W_m--- *molecule weight*
ω--- *acentric factor*
T_c--- *critical temperature*
P_c--- *critical pressure*
Z_c--- *critical compressibility factor*

Appendix B

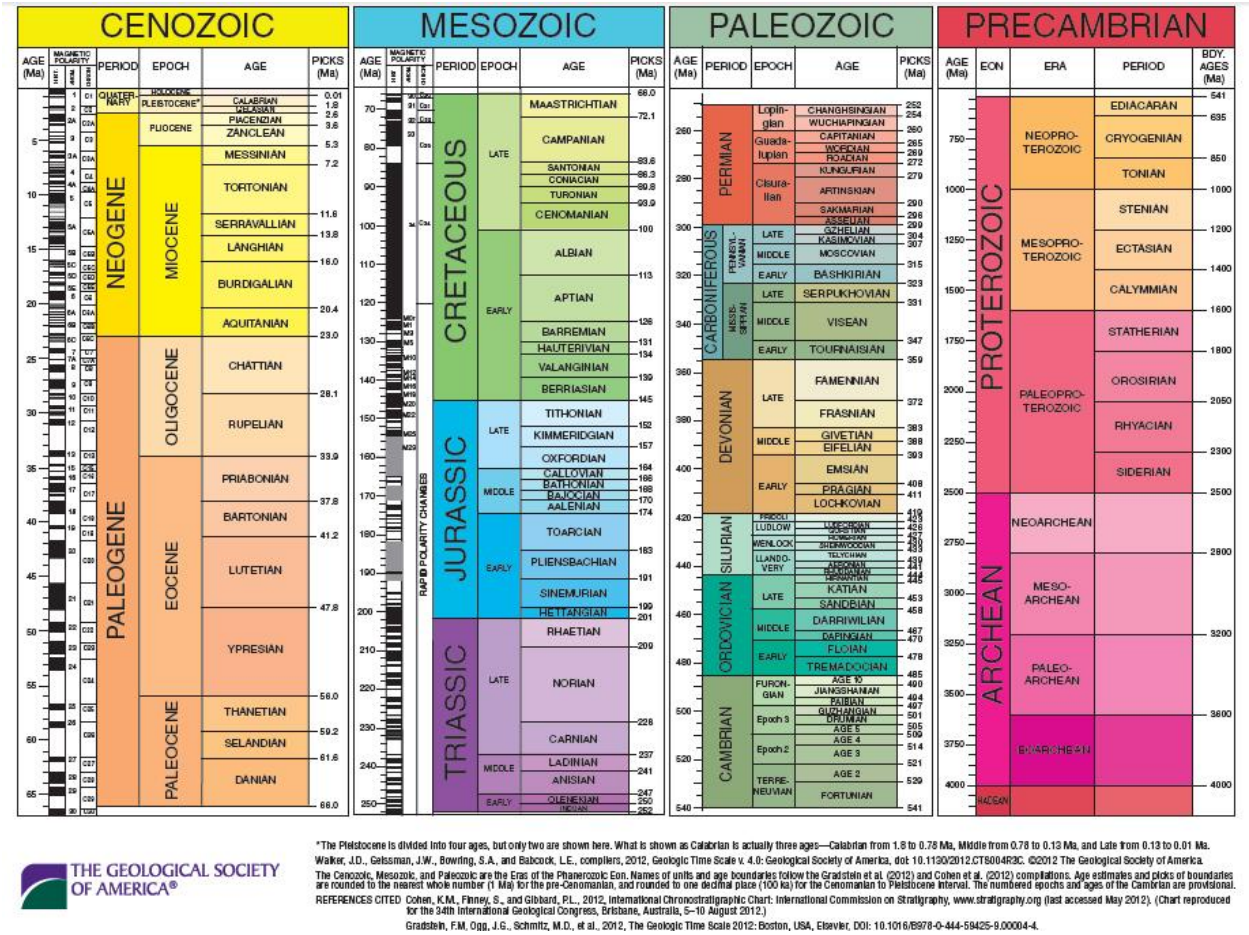

Figure B.1 Geologic Time Scale